ABSTRACT

HARP, JASON MICHAEL. Examination of Noble Fission Gas Diffusion in Uranium Dioxide Using Atomistic Simulation (Under the direction of Ayman I. Hawari).

An approach is investigated for coupling the results of nuclear reactor fuel test experiments with multi-scale atomistic simulations for the interpretation of the migration and release of fission gas from nuclear reactor fuel. Of interest in this work are gas cooled High temperature reactors that utilize Tri-Isotropic (TRISO) coated particle fuel as their fundamental fuel form. TRISO fuel consists of a small sphere (kernel) of uranium dioxide (UO_2) or uranium oxycarbide surrounded by several layers of coatings that serve as the primary barrier to fission product release in high temperature reactor designs. If a catastrophic failure occurs in a TRISO particle where the layers are breached, fission products that have migrated through the kernel (especially Kr and Xe) will begin to escape the failed TRISO particle.

In-reactor fuel qualification tests for TRISO fuel are currently on going, and their performance is monitored through the use of gamma-ray spectrometry measurements of escaping fission products such as Kr and Xe. The gamma-ray spectra are analyzed to determine the release-to-birth (R/B) ratios of Kr and Xe. Empirical models of R/B for failed TRISO particles have been developed based on previous experience. These models show that the dominant release term, diffusion, in a R/B model is partially determined by a diffusion coefficient that can be empirically extracted and compared to values derived from atomistic simulations. Therefore, a link may be established between microscopic phenomena that influence fission gas diffusion and macroscopic observations of release trends.

In this work, the simulation approach was implemented in the form of multi-scale Molecular Dynamics (MD) and Kinetic Monte Carlo (KMC) algorithms. The MD model successfully reproduced several thermo-physical properties including thermal conductivity. In addition, the model generated the basic input (i.e., migration energies and atomic vibration frequencies) that are needed to describe the physics of diffusion in KMC. Using this approach, the self-diffusion behavior of O and U, and the diffusion behavior of Kr and Xe in UO_2 were examined for bulk and grain boundary conditions. In addition, the potential effect of radiation, which could represent a burn-up state of the fuel, was considered.

The results show that the simulations are able to capture the vacancy driven bulk self-diffusion of O and U atoms in UO_2. In the case of Kr and Xe, the examined diffusion mechanism, which assumes the incorporation of Kr and Xe atoms in neutral tri-vacancy clusters of UO_2, appears to underestimate the diffusivity as measured in relatively low burn-up fuel. Given the agreement found for the self-diffusion data, the KMC simulation suggests additional potential migration pathways, beyond the conventionally suggested tri-vacancy mechanism, enhance the migration of Kr and Xe in low burn-up UO_2 fuel.

Furthermore, the resulting diffusion coefficients from the simulations were transformed into R/B values for Kr and Xe escaping failed fuel and compared to models for failed TRISO particles. Specific trends in the R/B values were identified as evidence of different release phenomena such as elemental dependent diffusion coefficients, recoil release, and enhanced diffusion due to long lived parent isotopes. The results reflected the same trends observed for the diffusivity data, which implies that this macroscopic observable (that is explicitly derived from experiments) may be utilized in the interpretation of the migration and release phenomena.

Examination of Noble Fission Gas Diffusion in
Uranium Dioxide Using Atomistic Simulation

by
Jason Michael Harp

A dissertation submitted to the Graduate Faculty of
North Carolina State University
in partial fulfillment of the
requirements for the Degree of
Doctor of Philosophy

Nuclear Engineering

Raleigh, North Carolina

2010

APPROVED BY:

_____   _____
Ayman I. Hawari   Mohamed A. Bourham
Committee Chair

_____   _____
Steven C. Shannon   Paul R. Huffman

Dedication

To Melissa for all the support and encouragement I received from you during the course of finishing this work.

Biography

Jason M. Harp was raised in the small West Texas town of Canyon. Canyon is home to West Texas A&M University and is in close proximity to the DOE Pantex site, which would prove influential in his choice to pursue a career in Nuclear Engineering.

After graduating from Canyon High School in May of 2001, Jason began attending Texas A&M University in College Station, TX. In August of 2001 he began class work for his B.S. degree in Nuclear Engineering. During his time as an undergraduate, Jason interned for two summers at the DOE Pantex site. Jason also spent two summers at Los Alamos National Laboratory. While at LANL, he worked with the Applied Physics (X) Division Nuclear Data Team on projects that included an investigation of Tritium production in the lithium isotopes and investigation comparing Monte Carlo and deterministic benchmarks for critical assemblies. On May 14, 2005, Jason graduated Magna Cum Laude from Texas A&M University.

Jason was honored as an Advanced Fuel Cycle Initiative Fellow for 2005. In August of 2005, he began his graduate studies at North Carolina State University. During the course of his graduate work Jason had the opportunity to work extensively with the staff at Idaho National Laboratory on the AGR-1 TRISO fuel experiment including spending several summers at Idaho National Laboratory. In May 2007 he received his M.S. degree from North Carolina State University under the direction of Dr. Ayman Hawari. Jason then began work on his PhD also under Dr. Ayman Hawari. After completion of his PhD, Jason plans to begin work at Idaho National Laboratory in the Fuel Performance and Design department.

Acknowledgements

Table of Contents

Chapter 5 Kinetic Monte Carlo Calculations 97

Chapter 6 Conclusions and Future Work 142

References 147

Appendices...144

Appendix A - Investigation of an Experimental Technique to Separate Krypton and Xenon 155

Appendix B – Derivation of Average Phonon Frequency for use as KMC Input..170

List of Tables

List of Figures

Chapter 1 Introduction and Background

The behavior and performance of nuclear reactor fuel especially TRISO fuel can be monitored through the use of gamma-ray spectrometry measurements of escaping noble gas fission products. By applying proper physics informed interpretation to the resulting spectra it is possible to infer the condition of the fuel and information about how the fission products are migrating out of the fuel. Experimental results coupled with simulations of the suspect phenomena result in more accurate fuel behavior models that can lead to the design of superior performing fuels. Thus, the focus of this research is to explore techniques that lead to a deeper understanding of fission gas release from failed TRISO fuel.

In this work, the mechanisms of fission gas release have been observed from the collection of the gamma-ray spectrum of radioactive Kr and Xe fission gas released from in-pile TRISO irradiation experiments. Semi-empirical models exist that relate the amount of gas produced in failed TRISO fuel (birth activity) to the amount of gas released (release activity) from the fuel. These models are referred to as release to birth or R/B models. They are based on the assumption that the gas is diffusing out of a sphere of some characteristic radius and the spherical solution to the diffusion equation [1]. One of the most informative techniques for observing trend and the physics of fission gas release occurs when the relative R/B ratios of different isotopes are compared against their half lives. With these plots it is easy to identify important trends in the fission gas release that arise from different physical phenomena. From the relative R/B plots, it is possible to observe whether Kr and Xe diffuse at different rates, if there is enhanced diffusion due to a long lived precursor to the observed

isotope, or if there are important non-diffusive effects e.g. recoil present in the release. Many R/B models account for recoil and enhanced diffusion due to a long lived precursor [2]. However, there may be other more subtle effects masked by the limits of experimental conditions. Atomistic simulations can assist in further understanding fission gas release by simulating fission gas diffusion in TRISO fuel kernel materials. These simulations are useful in explaining the microscopic phenomena that effect fission gas diffusion on a macroscopic level. Several different properties of TRISO fuel kernel material and their impact on diffusion can be studied using atomistic simulation. The diffusion of Kr and Xe through the polycrystalline UO_2 kernel is the primary release pathway for most radioactive fission gases. Diffusion through bulk crystals, changes in diffusion due to grain boundaries, and changes due to radiation damage can all be accounted for using atomistic simulations. Data flows in both directions from the both experimental interpretation, which lead to insight into what must be modeled in atomistic simulation, and the atomistic simulations, which enhance the understanding of what phenomena can be expected to occur in the experiment. By combining physics informed experimental analysis and the results of well defined atomistic simulations it is possible to create an effective model for understanding fission gas release.

1.1 *A Brief History of HTR's and TRISO Fuel*

The concept of high temperature gas reactors and coated particle fuel has been under development for several decades [3]. Several different countries have had active gas reactor programs including the United States, Germany (FRG), Japan, Russia (USSR), South Africa, and the United Kingdom. There were several test reactors built in the 1960's and 1970's

such as the DRAGON reactor in the UK, AVR in Germany, and Peach Bottom in the US. Two prototype commercial reactors were also operated THTR in Germany and Ft. St. Vrain in the US. Currently, Japan and China are operating test reactors called HTTR and HTR-10 respectively [4], [5]. The US DOE Generation IV program has designated the very high temperature gas reactor (VHTR) as a target reactor design, and current US work on these reactors is carried out through the Next Generation Nuclear Plant program (NGNP) [6]. The VHTR in either its prismatic or pebble bed form is an attractive reactor design on account of its ability to produce electricity at nearly 50% thermodynamic efficiency, and the high temperature of its coolant that may be useful in the generation of Hydrogen or other process heat applications [7]. The all modern HTR designs are fuelled with TRISO particles contained in a graphite structure.

Several different generations of coated particle fuels were evaluated over the years. Most notably in the AVR reactor which operated for over 20 years from 1967 to 1988. Initially a two layer type called BISO fuel was introduced in the AVR. The BISO fuel had only the porous carbon buffer layer surrounded by a pyrolytic carbon layer. Later this design was replaced by the current concept TRISO type fuel particles. BISO fuel worked well to contain gaseous fission products; however, the multi-layer coating strategy used in TRISO fuel allows for retention of gaseous and metallic fission products within the fuel particle. Although initial designs for HTR fuels used highly enriched Uranium, current designs and fuel tests are performed with low enriched Uranium. The kernel fuel material is also not limited to UO_2 or other Uranium ceramics. The THTR reactor used a mixed U-Th fuel

kernel. Also, plutonium and other minor actinides have been proposed for use in the kernel of a TRISO particle as a disposal mechanism [8].

Current TRISO fuel consists of an inner fuel kernel surrounded by a porous carbon layer then an initial pyrolytic carbon layer followed by layers of silicon carbide and the second pyrolytic carbon layer. This type of fuel is made into fuel elements by compacting TRISO particles in a graphite over-pack into either cylinders or sphere depending on whether the reactor is the prismatic or pebble bed type. The cylinders would then be loaded into large hexagonal blocks of graphite in the prismatic type or straight into the reactor in the pebble bed case. The layers of TRISO along with the creation of the fuel elements for prismatic type reactors and a concept drawing of a prismatic High Temperature Reactor are shown in Fig. 1.1.

1.1.1 Current Fuel Tests

There are two primary methods used to study fission gas release from different types of nuclear reactor fuel. Post Irradiation Annealing exposes fuel to a radiation field at low temperatures in order to build up fission gas without causing diffusion. The sample is then transferred into a device where it is heated to high temperatures. The fission gas is then observed as it leaves the fuel. The second major method is In-Pile Release. In this type of experiment, the fuel is irradiated in core and sweep gas flows around the fuel carrying fission products out of the core for analysis. The techniques under development in this work are geared towards In-Pile Release experiments for failed TRISO fuel. In this case, fission gas release from TRISO fuel is usually quantified by taking the ratio of the measured release activity (R) of a specific Kr or Xe isotope to the predicted activity of the isotope in the fuel

due to irradiation conditions (i.e. birth activity (B)). This ratio is termed the Release-to-Birth Ratio (R/B). Several different semi-empirical models have been developed to predict the R/B behavior of failed TRISO particles. The different physical phenomena that contribute to the R/B ratios create distinct trends. Through proper analysis, trends in the models and trends in the experimental data can lead to a better understanding of the physical phenomena that control fission gas release from TRISO fuel.
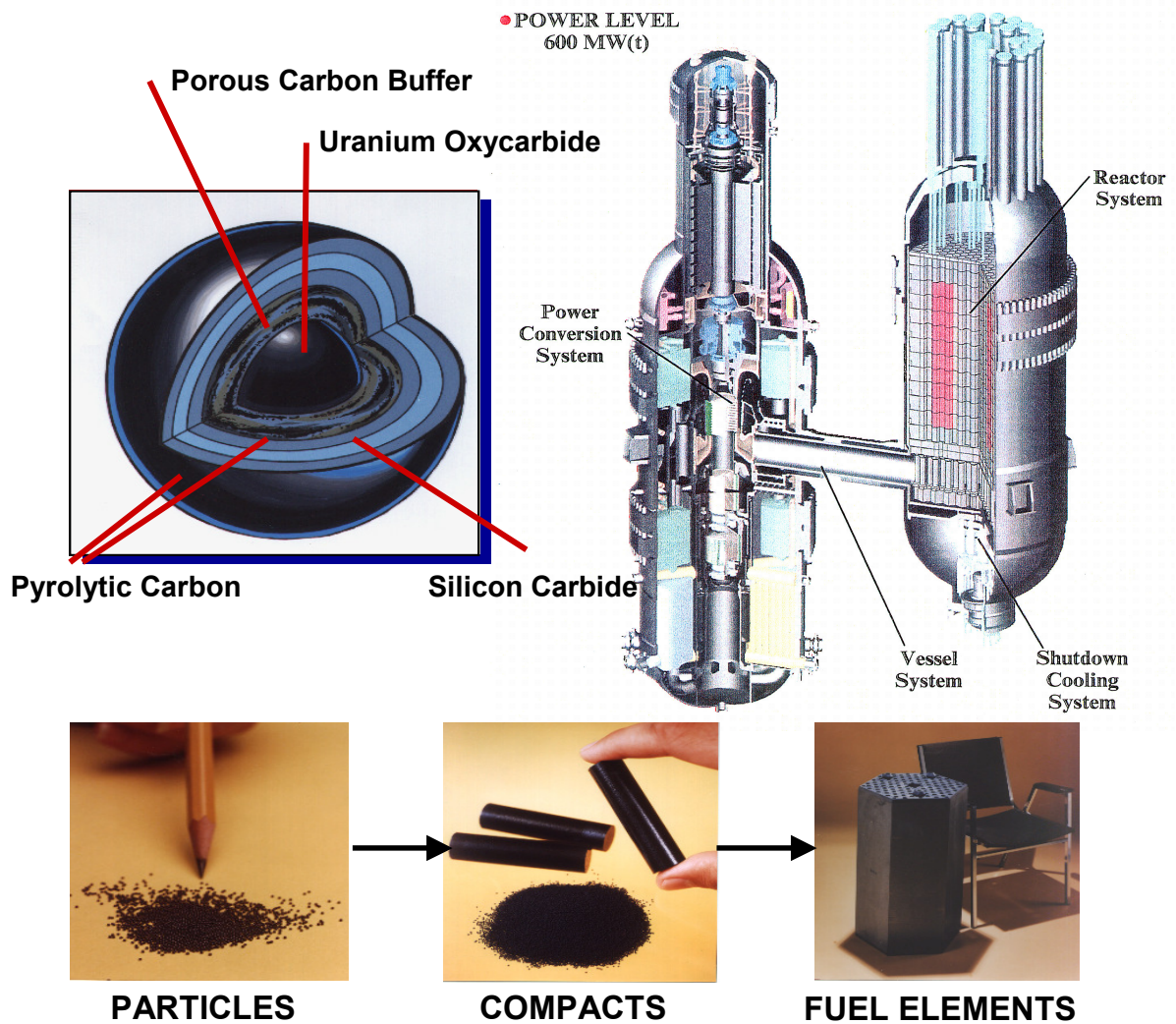
Fig. 1.1. TRISO Fuel Layers, its Configuration into Fuel Elements, and a High Temperature Reactor Concept Drawing

The environment of HTR cores coupled with the desire for high burn-up fuel utilization lead to significant engineering challenges. TRISO fuel will be subjected to high temperature (peak around 1500 K), high radiation damage conditions (fast neutron fluence reaching 4×10^{21} n/cm^2), and high burn-up (15-20 % FIMA) [9]. Under these conditions, the silicon carbide and pyrolytic carbon layers may fail due to manufacturing defects or pressure due to fission gas build up inside the TRISO particle. If these layers fail, fission gas, most notably the noble gases Kr and Xe, will escape via different release mechanisms into the core. A series of fuel tests is currently underway at Idaho National Lab (INL) named the AGR or Advanced Gas Reactor series. These tests will be irradiated in the Advanced Test Reactor at INL in gas flow temperature controlled capsules. The first in-core irradiation test (AGR-1) in this series was successfully completed on November 6, 2009. During this irradiation the TRISO fuel in the capsules set a world record for TRISO fuel performance when they achieved 19% FIMA burn-up with no failures [10]. This burn-up milestone far exceeds the previous fuel performance marks set by the German program and light water reactor fuel. There are seven other TRISO irradiations scheduled currently in the AGR program including tests with designed to fail particles that can be used to validate fission gas release models [11].

1.2 *Using Atomistic Simulation to Interpret Fission Gas Release Experiments*
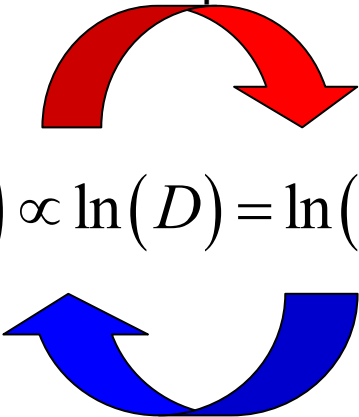
Atomistic Simulation can be used as an interpretation tool for elucidating data from experimental measurements. For this work the most basic experimental data is gamma-ray spectra collected in on-line monitoring of in-pile release TRISO fuel experiments. The

analysis of gamma-ray spectra is coupled with other experimental conditions such as temperatures, effluent flow rates, pre-irradiation fuel properties, and generation/depletion calculations to create Release to Birth (R/B) Ratios for different isotopes of Kr and Xe. The experimental R/B values are compared to R/B models whose variables can be either theoretical or semi-empirical. A key factor in R/B models is the diffusion coefficient of the Kr or Xe isotopes of interest. The diffusion coefficient is one of the many values that can be derived from Atomistic simulation. Additionally, with atomistic simulation many of the different phenomena that influence the behavior of the diffusion coefficient such as radiation damage and grain boundaries can be explored using the proper simulation techniques. More fundamental data about the atomic behavior of the system under investigation can also be investigated, for example the migration energy (E_m) of Kr and Xe through the crystal structure of the fuel under investigation. Therefore, with atomistic simulation it is possible to very diligently explore the many different factors that influence diffusion and identify how they will impact R/B values. Given these properties of experimental release and atomistic simulation, the diffusion coefficient and its relationship with the R/B values is the pivot point where data from experimental results can transfer to atomistic simulation and in turn where interpretations from atomistic simulations can be fed back to better analyze experimental results. This point is illustrated by Fig. 1.2 where the relationship between experimental R/B and simulated factors like the diffusion coefficient and the migration energy are shown.

In Fig. 1.2, k is Boltzmann's constant and T is the temperature of the system under investigation. The arrows in Fig. 1.2 demonstrate how data can flow between experimental analysis to become inputs in simulations, and the results of simulations assist in the

predicting the behavior and interpreting the analysis of experiments. Essentially by performing this two way analysis, collected gamma spectra become a map of the fission gas release from TRISO fuel that atomistic simulation helps you read.

Measurements of R/B are compared to E_m from simulation

$$\ln\left(R/B\right) \propto \ln\left(D\right) = \ln\left(D_0\right) - \frac{E_m}{kT}$$

Computational predictions of E_m feed into models of release

Fig. 1.2. The key link between nuclear fuel tests and atomistic simulations for the diffusion behavior explored in this work

Chapter 2 Analysis of Data from TRISO Fuel Irradiation Tests

2.1 *Fission Gas Release Models*

Fission gas is released from the fuel when gas migrates through the crystal structure of the fuel into the free volume between fuel grains then through the graphite matrix and into the effluent stream. The release activity due to isotopes of Krypton and Xenon that have reached equilibrium activity in the fuel can be described by R/B models. The R/B models include terms for fission product release from catastrophic failure of the TRISO particle, heavy metal contamination in the graphite matrix surrounding the fuel, and the direct recoil of fission fragments.

The major pathway for fission gas to escape the fuel and enter the effluent stream is through gaseous diffusion. Under steady state conditions, most R/B models use some form of the Booth equivalent sphere model to predict R/B caused by diffusion [12]. The Booth model can be best understood as the solution to the steady state diffusion equation for the flux of gas atoms over a sphere of fixed radius [13]. Equation (2.1) contains the general form of the Booth model

$$\left(\frac{R}{B}\right) = 3\sqrt{\frac{D}{\lambda a^2}}\left[\coth\left(\sqrt{\frac{\lambda a^2}{D}}\right) - \sqrt{\frac{D}{\lambda a^2}}\right], \qquad (2.1)$$

where D is the diffusion coefficient, λ is the decay constant, and 'a' is the radius of the equivalent sphere which is the fuel kernel radius for TRISO fuel. Often the D and 'a' terms are combined to create reduced diffusion coefficients.

The application of the Booth model is relevant to both diffusion release by the kernel and release coming from heavy metal contamination in the graphite matrix. A key feature of such models is the temperature dependent diffusion coefficients. Some models show that these coefficients may also depend on the element that is diffusing.

In this work, three different R/B models are examined. The German model (as presented by [14]) uses the same form as Equation (2.1) to model both gas release from the failed TRISO particle and heavy metal contamination. The JAERI model modifies this formulation to include precursor effects, burn-up corrections, and accounts for the effect of fission gas diffusion through the fuel compact matrix [15]. This model also can be used to predict R/B ratios for heavy metal contamination. The General Atomics (GA) model follows a similar approach to the other models [16], and adds terms that include recoil, thermal re-solution, and diffusion. However, this model does not contain terms for calculating release from contamination in the graphite matrix.

A major difference between the above models appears in the diffusion coefficients that were derived from different experimental measurements. Contemporary fuel tests are necessary to establish which (if any) of these models best describes the current generation of TRISO fuel. In fact, it may be necessary to combine features from the different models described above to accurately describe fission gas release.

2.2 *Formulation of R/B indicators*

In experimental implementation, the development of the R/B ratios involves the measurement of the activities of the radionuclides of interest using gamma-ray spectrometry.

An example of this work is the Advanced Gas Reactor (AGR) TRISO fuel experiments that are currently taking place at the Advanced Test Reactor (ATR) of Idaho National Laboratory [17]. In the first AGR experiment (AGR-1) experimental R/B ratios were calculated in a multistep process. The effluent from 6 different TRISO fuel test capsules in the ATR were monitored by 6 identical gamma-ray detection systems called Fission Product Monitoring Systems (FPMS). High Purity Germanium Detectors in each FPMS continuously collected Gamma-ray spectra in 8 hour intervals before, during, and after each reactor irradiation. In Fig. 2.1, a typical gamma-ray spectrum for AGR-1 is shown. It contains many different gamma-ray peaks corresponding to several different Kr and Xe fission products. Peak areas for gamma-rays of interest were analyzed to determine the activity of each Kr and Xe isotope of interest at the detector. The activities of each isotope were then corrected for decay during transport to derive the release activity at the fuel. These values were then divided by birth activity values obtained from a coupled neutron transport / generation and depletion program. The final results of these calculations were experimental R/B values for each Kr and Xe isotope of interest throughout the entire course of the AGR-1 experiment that can now be compared to the previously developed R/B models detailed in the previous section [18].

Predicted R/B ratios for the various radionuclides can be calculated using the R/B models described above and the known experimental conditions. Subsequent comparisons between model predictions and measurements can be made to infer the validity of a particular model for describing the physics of the gas release process from the fuel.
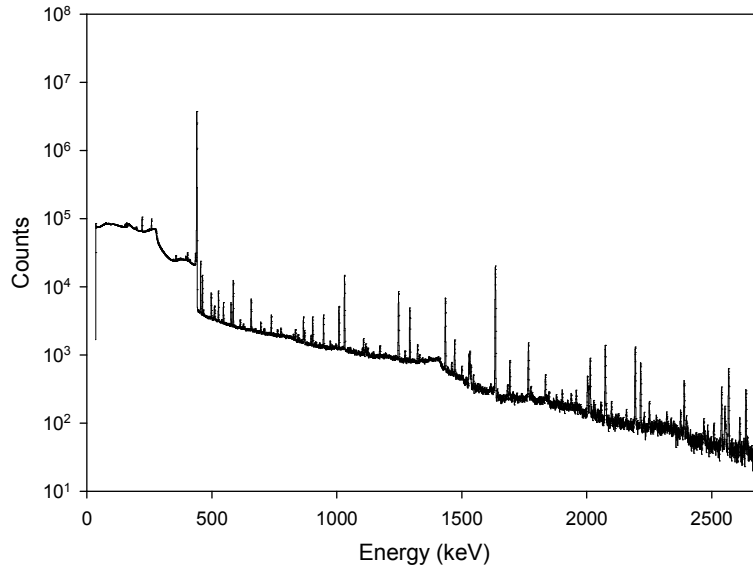
Fig. 2.1. Typical Experimental Spectrum from the AGR-1 Experiment

Typically, the comparison between measured R/B values and model predictions are made on an absolute basis. However, this type of comparison will include uncertainties that are contributed by both components of the ratio (release (R) and birth (B)). The measured value of R (for a given radionuclide) represents the release activity and will include uncertainties due to statistical and instrumentation calibration factors. B is usually obtained from a neutronic model that includes a specific description of the anticipated experimental conditions. In this case, uncertainties associated with power levels (and corresponding thermal neutron fluxes) and spectral averaged cross section (e.g., for fission or for the production and loss of a given radionuclide) can be significant.

Consequently, a relative approach was proposed that could be less susceptible to such uncertainties. Specifically, a relative R/B indicator is defined below [1], [19].

$$I = \frac{R_1}{B_1}\left(\frac{B_2}{R_2}\right).$$

(2.2)

12

In this case, 'I' (the relative indicator) is established based on the ratio of R/B values for a given radionuclide (subscript 1) relative to the R/B value for a reference nuclide (subscript 2). The radionuclides of interest are the various Kr and Xe isotopes that range in half-life from minutes up to hours.

The uncertainty in 'I' will be caused by the uncertainties in R1/R2 and B2/B1. Formulating a ratio for the release rates will allow minimizing the impact of effects such as gas travel time and detector efficiency calibration [20]. The ratio of birth rates is expected to be fairly resistant to variations in irradiation conditions. This will be especially true for short-lived radionuclides that have negligible absorption cross sections [1].

2.3 Gas Release Trends Using Relative R/B Indicators

2.3.1 Physical Interpretation of Indicator Trends

To test the approach presented above, the experimental conditions of the latest in-core TRISO fuel test (AGR-1) at the ATR were used to calculate R/B ratios for the various models. Simulations of the AGR-1 experiment were performed to predict the birth activities and expected gamma ray spectrum due to failed particles and heavy metal contamination release [21]. Estimates of the birth activities of the Kr and Xe isotopes were obtained using ORIGEN [22] depletion calculations. Once the predicted R/B values were established, a reference radionuclide was chosen to create predicted relative Release-to-Birth indicators.

Figure 2.2 shows the predicted relative indicators (I) for failed TRISO particles using Kr-85m as the reference radionuclide versus half-life. Kr-85m was chosen as the reference isotope based on its physical properties. It has a half-life (4.48 hours) that is sufficiently

short to allow reaching an equilibrium concentration in the fuel, but is long enough that decay during transport from the irradiation position to the detector is not significant. The transport time is on the order of 2 to 3 minutes [23] which poses a significant challenge for the detection of the shorter lived radionuclides of interest like Kr-90, Kr-91, and Xe-139. Kr-85m also has a distinct 75.4% yield gamma-ray at 151.2 keV that occurs in a section of the gamma ray spectrum that is relatively free of any other full energy peaks.

By recognizing the physics of a given R/B model, it is possible to observe several key trends in Fig. 2.2. For example, the German model is known to use a single expression to describe the diffusion coefficients of Kr and Xe for failed TRISO particles. In this case, half-life becomes the important factor in the R/B estimations showing a clear trend for the ratios to decrease as the half-life decreases.
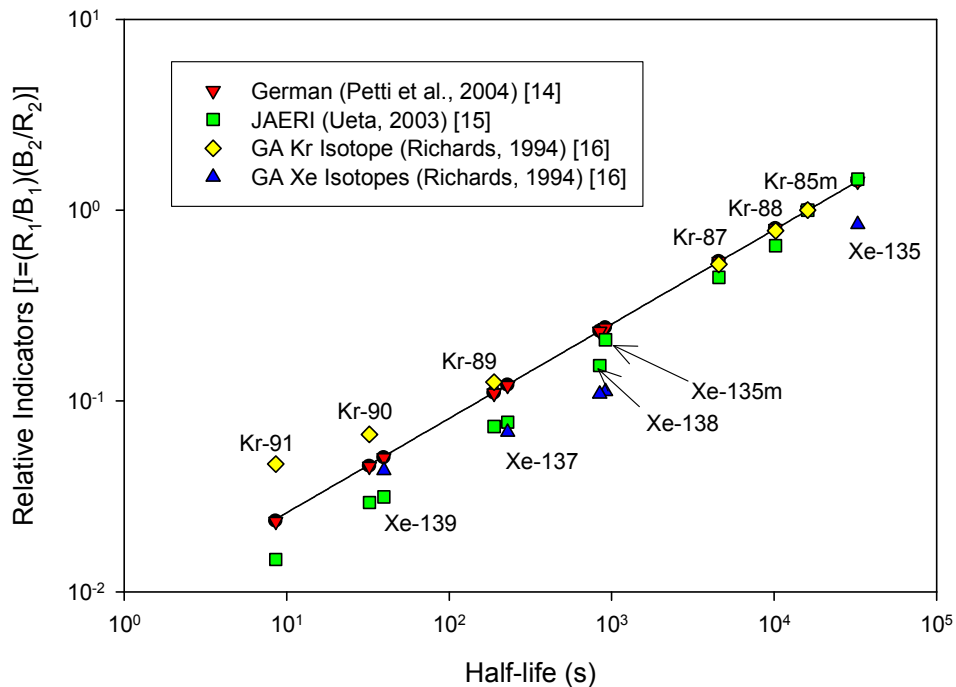
Fig. 2.2. Indicator values for different failure models as a function of half-life for failed TRISO particles. Kr-85m is used as the reference radionuclide and a temperature of 1448K is assumed [25]. The solid line is used as an illustration guide to assist in the visual interpretation of the trends.

14

This trend stems directly from the Booth model which is proportional to the square root of half-life for the nuclides of interest. However, in the GA model this trend is not observed. The GA model uses different empirical relationships for Kr and Xe to determine the diffusion coefficients. The result is that this model has two separate Xe and Kr indicator trends. The JAERI model also appears to follow the same half-life trend as the German model, which is expected since the JAERI model uses only a single diffusion coefficient relationship for kernel diffusion of Kr and Xe. However, deviations from this trend are observed when examining the data for Xe-135m ($T_{1/2}$ = 15.3 min) and Xe-138 ($T_{1/2}$ = 14.1 min). This is attributed to the fact that the JAERI model accounts for the half-life of the precursor of a given isotope. In this model, the R/B for a particular nuclide is enhanced if it has a long lived precursor. Consequently, the long lived precursor of Xe-135m (I-135 $T_{1/2}$ = 6.57 h) increases its R/B when compared to a nuclide with a similar half-life like Xe-138 with a short lived precursor (I-138 $T_{1/2}$ = 6.5 s).

Figure 2.2 also demonstrates the trends that are indicative of the second major pathway for fission gas release, i.e. direct recoil. This pathway enhances fission gas release from shorter lived isotopes that tend to decay before they can diffuse out of the fuel. Notice that the German model displays a linear relationship with half-life on the log-log plot. This is a result of ignoring recoil release. The GA and JAERI models account for recoil and do not have the strictly linear response that indicates diffusion only release mechanisms. This effect is most clearly illustrated by the indicator values of Kr-91, Kr-90, and Xe-139 for the GA model.

As seen above, it is expected that by combining relative R/B indicators with such observed trends for the various models, analysis of the experimental data (i.e., the gamma-ray spectra of released fission gases) can be extended to understanding, differentiating and validating the various models for fission gas release.

2.3.2 Application to AGR-1 Data

As an experimental implementation of the approach presented above, an analysis was performed of a representative gamma-ray spectrum collected from the AGR-1 experiment. In this experiment, graphite fuel compacts that contain TRISO particles are irradiated at the B-10 position of the ATR. At this time there have been no detected TRISO failures in the AGR-1 experiment [24], but tramp uranium contamination in the fuel compacts produce gamma-ray spectra for analysis. High purity germanium detectors continuously collect gamma-ray spectra of the fission products exiting the AGR-1 fuel compacts. Collected spectra are periodically analyzed to attain the gamma ray peak areas. The peak areas are combined with the detector efficiency and the gamma-ray yield to derive the release activities of the isotopes of interest. Before the release activities can be transformed into Release-to-Birth indicators, they must be corrected for decay during transport from the irradiation position to the detector. For each capsule the flow rate of the He effluent is continuously monitored and recorded at the ATR. The decay time is determined by the volume of tubing that the fission products must pass through to get to the detector divided by the volumetric flow rate of the effluent [23]. After the release activities are calculated, they are combined with the birth activities calculated from ORIGEN as show in Eq. 2.2 to construct the experimental relative R/B indicators.

Relative R/B indicators (I) based on the experimental data have been calculated and are shown in Fig. 2.3. The error bars of the experimental data are principally from counting statistics. In addition, computationally predicted relative indicators (I) based on the heavy metal contamination components of the German and JAERI models are also plotted in Fig. 2.3 as solid lines. The models can be displayed in this manner by assuming that the half-life of the non-reference isotope is a continuous parameter. The temperature of the fuel is assumed to be 1125 K based on AGR-1 thermocouple data for the date of the test [25].

There are several observations that can be ascertained from Fig. 2.3. The experimental data exhibits two separate trends for Kr and Xe. This behavior is qualitatively consistent with the German model, which for heavy metal contamination has two different reduced diffusion coefficient correlations for Kr and Xe. However, The German model prediction for Xe severely underestimates the magnitude the relative R/B value of Xe. This could be indicative of an inconsistency between the reduced diffusion coefficient assumed in the German model and the reduced diffusion coefficient that might be deduced from the experimental values. The experimental data suggests that the apparent difference in reduced diffusion coefficient between Kr and Xe is not as dramatic as proposed by the German model. The JAERI model has only a single trend for Kr and Xe, but it does trend closer to the experimental data than the German model predictions. This is especially true for the shorter lived isotopes like Kr-89 for which recoil release becomes an important mechanism. One feature that does not appear in Fig. 2.3 is evidence of a precursor effect. The experimental indicator value (I) for Xe-135m does not exhibit any enhanced diffusion due to

its long lived precursor when compared to the indicator value of Xe-138. However later in the AGR-1 test the Xe-135m indicator does begin to show signs of a precursor effect.

The curvature exhibited by the JAERI model line is the result of recoil. Recoil is accounted for in the JAERI model but not in the German model for contamination. The straight lines of the German model are representative of pure diffusive release. The slope of these lines on the log-log plot is near 0.5 which corresponds to the square root of half-life dependence of the Booth model. The experimental trend lines do not have the 0.5 slope. This indicates that non-diffusive mechanisms like recoil are important for describing these experimental results.

Neither model adequately describes the behavior of the Xe-135 indicator (I). This indicator is characterized by a large absorption cross section which makes its calculated B value highly sensitive to accurate knowledge of the experimental conditions and their reflection in the neutronic simulations. A modification to both the German and JAERI models is found by adjusting the loss mechanisms that are assumed in the R/B model to account for the transmutation of this radionuclide caused by its large absorption cross section. The inclusion of this correction term reduces the R/B ratio reducing the indicator values. This helps remove some of the discrepancy between experimental indicators and predicted indicators.
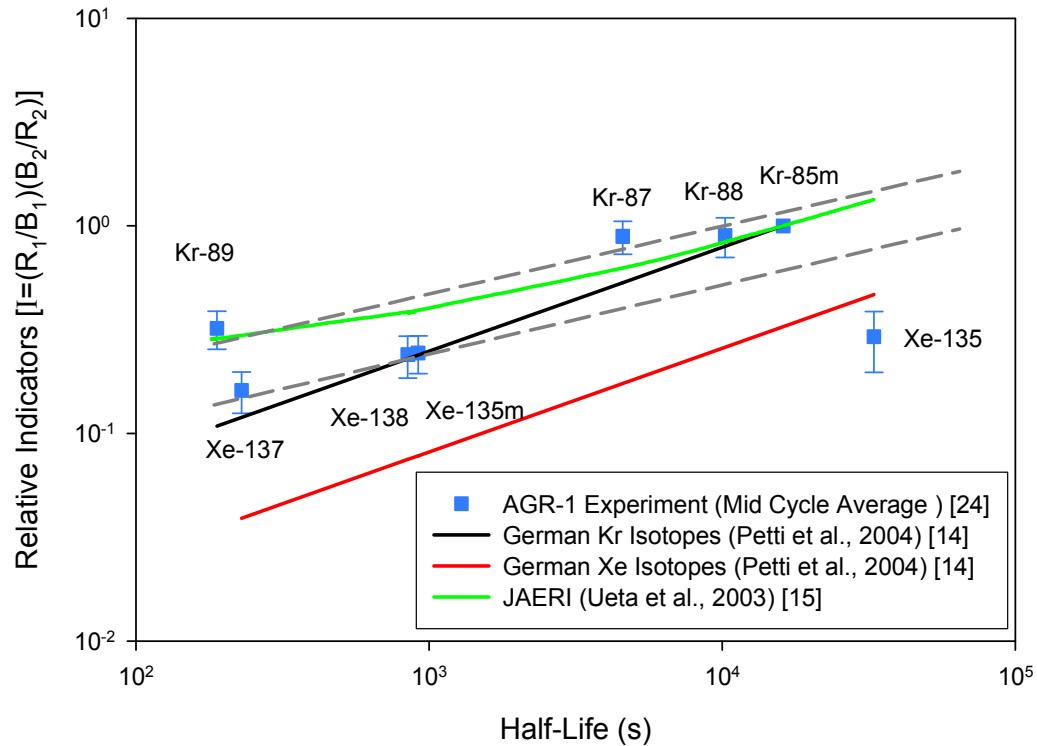
Fig. 2.3. A comparison between experimentally derived relative R/B Indicator (I) values and model predictions. The experimental points are based on capsule 2 measured mid-cycle data of the 2nd irradiation cycle of AGR-1. One standard deviation uncertainty bars are shown. The data was collected between March 26 and April 6, 2007. The predicted R/B indicators (shown as solid lines) are for release from heavy metal contamination at 1125K. Dashed lines are drawn through the experimental data points to assist in observing trends.

2.3.3 Summary of Gas release trends from R/B Indicators

1. The use of relative R/B indicators (I) can provide an accurate approach that facilitates studying gas release mechanisms from TRISO fuel.
2. The different mechanisms of fission gas release can be observed from the relative Release-to-Birth indicator (I) form. These mechanisms include
   (a) Diffusion release
   (b) Recoil release
   (c) Separate diffusion rates for different elements
   (d) Precursor effect on diffusion
3. Analysis of representative data from the AGR-1 experiment is indicative of:
   (a) Two reduced diffusion coefficients for Kr and Xe
   (b) Significant recoil release for the short lived isotopes of Kr and Xe.
   (c) To accurately simulate Xe-135 indicators, the transmutation of this isotope must be taken into account.

19

4. Potentially, this approach can be used to guide the introduction of modifications to the predictive models that enhance the agreement between measured and predicted relative R/B ratios.

2.4 *Arrhenius Analysis of TRISO Fuel Test Data*

In addition to analyzing In-Pile release experimental data against the half life of the isotopes of interest, it is also instructive to analyze the temperature dependent responses of the different isotopes. The temperature dependent responses of the R/B values provide more detailed information about the diffusion coefficients that govern fission gas release from failed TRISO particles. Indicator values that are created by taking the ratio of R/B values are useful for examining many aspects of the physics of fission gas release [2]. However while indicators can clearly illustrate when Kr and Xe are not diffusing at the same rate, they do not provide information about the value of the rates or temperature dependence of the rates of the Kr and Xe diffusion. A solution to this problem is to transform R/B data into diffusion coefficients and graph them on an Arrhenius plot (ln(D) vs. 1/T). The migration energy of the fission gas can be found from the slope of the Arrhenius plot. In addition, migration energy can be calculated for a system using a multi-scale atomistic simulation approach. The experimental migration energy provides a link between experiment and simulation that can be used as a simulation benchmark.

Fission gas release from failed TRISO particles and TRISO contamination is described by the Booth equation [12] which can be written as shown in Equation (2.3).

$$\frac{R}{B} = 3\sqrt{\frac{D'}{\lambda}}\left[\coth\left(\sqrt{\frac{\lambda}{D'}}\right) - \sqrt{\frac{D'}{\lambda}}\right] \qquad (2.3)$$

Where *D'* is the reduced diffusion coefficient that is found by dividing the Diffusion coefficient by the square characteristic spherical radius. Most TRISO R/B models either have a reduced diffusion coefficient empirical relationship with temperature, or they use the radius of the TRISO fuel kernel as the characteristic radius. The experimental conditions (T>900K) and isotopes of interest ($T_{1/2}$<10 hours) of most in-pile release experiments allow for the simplification of Equation (2.3) to the form seen in Equation (2.4).

$$\frac{R}{B} \approx 3\sqrt{\frac{D'}{\lambda}} \tag{2.4}$$

This approximation is used to transform the experimental R/B values collected from the AGR-1 experiment into diffusion coefficients for the Arrhenius analysis.

After fission Kr and Xe come to rest in the fuel material lattice (i.e. UO_2 or UC_2). The atoms can then begin to migrate through the crystal lattice. The net effect of this migration is that the diffusion coefficient can be described by the following Arrhenius relationship.

$$D' = D'_o e^{-E_m/kT} \tag{2.5}$$

Where D'_0 is the exponential pre-factor that contains the average jump distance and the frequency of jumps, E_m is the migration energy, k is Boltzmann's constant, and T is the Temperature in Kelvin.

The AGR-1 experiment has had no fuel failures through 3.0 years of operation. However there has been a wealth of information and spectra collected from release due to tramp Uranium. Using Equations (2.4) and (2.5) the R/B values derived from the collected spectra of AGR-1 were converted to diffusion coefficients and plotted against the inverse temperature values taken from the thermocouple data of the experiment. The amount of thermocouple data available decreased as the experiment progressed due to the loss of

thermocouples due to the harsh operating environment (high temperature, high irradiation damage) of the AGR-1 experiment. In order to calculate the experimental diffusion coefficients, the average R/B for a cycle for each detector and several different isotopes was calculated from the recorded AGR-1 experimental data. The recorded average R/B value includes a recoil term which was subtracted out so that only the diffusion portion remained. The average R/B values and Equation (2.4) were used to find a cycle / detector average reduced diffusion coefficient.

There are clear temperature dependent trends that exist in the data. The AGR-1 experiment operation sought to maintain a steady temperature throughout each cycle. The data has the expected negative slope for all the isotopes. The general slope for the Kr isotopes and the Xe isotopes is also different. This observation agrees with evidence from the Indicators that Kr and Xe do not diffuse at the same rate. The magnitude of the slope, which is proportional to the migration energy, is greater for the Kr isotopes than the Xe isotopes. This is the same trend that can be inferred from the Indicator data.

Table 2.1 contains selected migration energies derived from different capsules (detectors) of the AGR experiment. Additionally, the AGR-1 experimental values are compared to an experiment performed in reference [26] that is an in-pile experiment that was very similar in nature to AGR-1, but it was performed on standard LWR UO_2 fuel. It is also possible to pull migration energies from the diffusion coefficient relations ships given in the German / INL model for contamination sources [14]. These relationships are of the same form given in Equation (2.5) and were derived from historic German data on TRISO fuel testing.

Table 2.1. Migration Energies Derived from the AGR-1 Data for Kr and Xe

	Migration Energy (eV)				Experiment [25]	German / INL Model [14]
Isotope	Capsule 2	Capsule 4	Capsule 5	Capsule 6		
Kr-85m	N/A	1.61	1.05	2.82	Kr - 2.7-3.0	Kr - 1.1
Kr-88	0.52	1.46	1.08	2.40		
Xe-138	0.87	1.11	0.39	0.41	Xe - 1.6-2.8	Xe - 0.815
Xe-135	0.97	1.01	0.49	1.21		

The interpretation of the experimental data would benefit from a better understanding of the relationship between the thermocouple temperatures and the actual temperatures of the fuel compacts. Additionally it should be noted that all fission gas from AGR-1 comes from contamination sources. The behavior of actual failed TRISO should be similar, but the apparent migration energies from the Arrhenius plot could change significantly with TRISO particle failure.

Chapter 3 Atomistic Model Development for UO$_2$

The bulk or macroscopic behavior of materials is often determined by the microscopic interactions of its constituent atoms. Molecular Dynamics (MD) seeks to link the microscopic simulation of atomic systems to derive the macroscopic properties of the bulk. This is accomplished by calculating the movement of the individual atoms of a system by solving the equations of motions defined by atomic interaction potentials. Several mechanisms associated with fuel failure can be explored using different flavors of MD. These mechanisms include fission product diffusion in the crystal structure of the fuel material. For the diffusion of Kr and Xe fission products through UO$_2$, understanding the formation and migration of O and U vacancies and O-U vacancy complexes is essential to fully modeling the Kr and Xe behavior. The creation of a quality UO$_2$ Molecular Dynamics model that reproduces the behavior of UO$_2$ for several different physical properties, including the self-diffusion properties of U and O, is key to forming a complete atomistic model of Kr and Xe diffusion in UO$_2$. The following sections discuss the development and testing of a classical MD model for UO$_2$ that can be used to assist in understanding TRISO fuel failure modeling.

3.1 *Atomistic Simulations*

What is observed as fission gas release from failed TRISO fuel is the culmination of a series of interrelated physical processes that take place over a wide range of time and length scales. No one model can account for the entire range of time and length, but the results of

models for simulating one scale can be passed to models for simulating the next scale. This multi-scale idea is illustrated by Fig. 3.1, which shows different simulation techniques and their applicable scales. For example density functional theory (DFT) or *Ab Initio* simulations can be used to approximately solve the Schrodinger equation for approximately 100 atoms. The results of DFT simulations are the forces between atoms and the energy difference in different atomic configurations. The forces between atoms can be used to create a potential energy function for Molecular Dynamics (MD) simulations, which typically consist of hundreds to tens of thousands of atoms. The energy differences between two states can be used by Kinetic Monte Carlo (KMC) Simulations to determine the frequency of atom movement for simulations that contain one or two orders of magnitude more atoms than MD simulations and can reach simulation times approaching minutes. With the proper interpretation, the output of each of these simulations can be related to experimental measurements of the continuum system [27].

3.1.1 Molecular Dynamics

Molecular Dynamics (MD) is an atomistic simulation technique where a system of atoms is determined by classical potential energy functions that describe the nominally pair-wise interaction between an atom and all other atoms in a system. In MD the evolution of a system is found by solving the potential energy functions to determine the Newtonian equations of motion for each atom in a system at discreet time steps. With a well characterized set of potentials, the resulting atomic trajectories mirror the properties of the material being simulated such as thermal expansion coefficient, bulk modulus, specific heat, vacancy formation energies, thermal conductivity, and diffusion coefficients.

Multiscale Modeling Framework

Multiscale modeling framework for catalytic processes that exhibit strong coupling between scales.
Adapted from Vlachos, *Adv. Chem. Eng.* 30, 1-61 (2005)
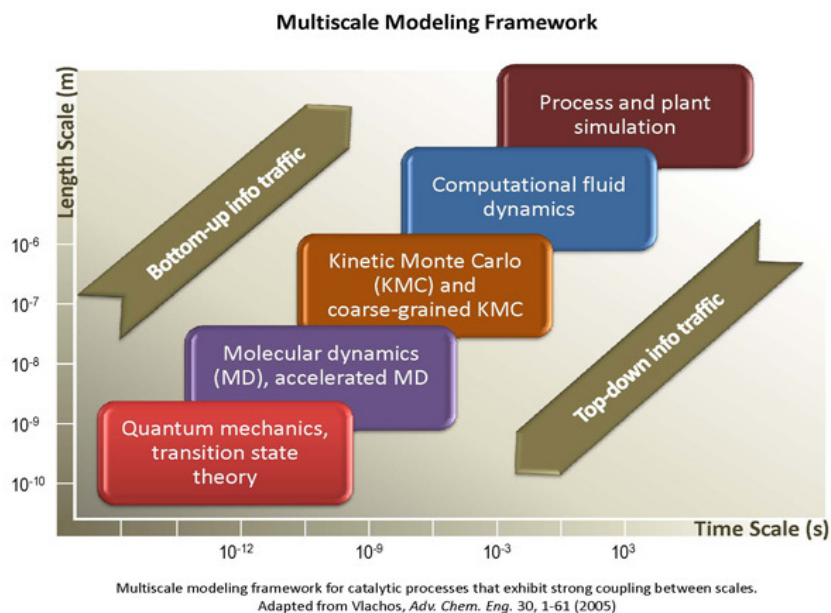
Fig. 3.1. Length and Time Scales used by different types of Atomistic and Continuum Simulations [28]

In a MD simulation the system of atoms have initial positions determined from the crystal structure of the material being simulated and are given an initial velocity from a Maxwell-Boltzmann distribution based on the initial temperature of the system. Periodic boundary conditions are typically applied to MD simulations. Under these conditions, the atomic configuration of the simulation cell is replicated by translating the atomic positions in three dimensions across the boundary to allow for interactions across the simulation cell edge. The short range forces on each particle in the MD simulation are calculated from the derivative of the potential energy equations. However at some distance the contribution of neighboring atoms becomes insignificant, and a force cutoff radius for atoms beyond which the short range forces are not calculated is normally applied to speed up the computational process. If a system is ionic, long range Coulomb forces must also be calculated. The form of the Coulomb force ($1/r$) does not converge quickly enough to use a computationally practical

cutoff radius. An alternative method of calculating ionic interactions called Ewald Sums. This method breaks the Coulomb force into real space and reciprocal space parts that converge quickly to the net force on an atom from charge interactions. After the forces are calculated, they are converted to acceleration and integrated to find Newton's equations of motion. The most common method for velocity and position prediction is a Verlet style algorithm which is 4th order accurate in position and 2nd order accurate in velocity. No matter which method is used it is important that the algorithm conserve the energy of the system and lead to a system trajectory that behaves on average how a true system of material atoms would behave. The size of the time step is also important. It must be short enough that the atoms would not travel significant distances between time steps that would hinder the propagation of short wavelength phonons through the system. However, the time step must be large enough that the simulation can be carried out in a reasonable amount of computational time. Usually the time step is on the order of 0.1 - 1 fs, but this value is very simulation dependent and certain simulations such as radiation damage cascades may call for significantly smaller time steps. The total simulation time is dependent on the time it takes for a system to reach equilibrium. For many systems this is a few picoseconds, but MD simulations can be run into the 100's of nanoseconds if the application deems this necessary.

As discussed above MD simulations would only apply to simulations where the microcanonical ensemble or constant particle (N), volume (V) and energy (E) (NVE) ensemble could apply. It would be much more convenient to specify constant temperature or pressure ensemble, and fortunately it is possible to specify thermostats and barostats for the system. By applying a thermostat to a MD simulation the equations of motions are modified

so that the net contribution of the velocities of the system will correspond to the desired system temperature. In a similar way the equations of motion can also be modified to produce the effect of constant pressure acting on the simulation. As a result constant particle, volume, and temperature (NVT) ensemble simulations are possible with MD as well as constant particle, pressure, and temperature (NPT) ensemble simulations.

Of the three primary inputs to a MD simulation (potential energy functions, initial crystal configuration, and simulation conditions like temperature, time steps, ensemble), the most effort is usually spent on creating a well characterized potential energy function. In reality interactions between atoms occur by a quantum mechanical process where electrons and nuclei are all interacting with each other. It is however possible to approximate the net effect of the quantum mechanical potential with classical potentials and Newtonian equations of motion if the de Broglie wavelength of the atoms in the simulated system is much smaller than the nearest neighbor atom distance. To accurately simulate the system, the potential energy function must emulate the true interaction of atoms as closely as possible within the limitations of its mathematical form, and ideally each factor in a potential energy function should have some phenomenological basis and not exist solely as an ad hoc fitting parameter. The potential energy function can be thought of as a collection of several components each describing a different physical phenomenon as seen in Equation (3.1).

$$U_{tot} = U_{Coulomb} + U_{Repulsive} + U_{Attractive} +$$
$$U_{Bond} + U_{Angle} + U_{Torsion} + U_{Non-Symmetry}$$

(3.1)

Where U_{tot} is the total potential energy function, and $U_{Coulomb}$ represents the electrostatic interaction between atoms in the system. Because the Coulomb force is not quickly vanishing on MD length scales, this term is usually handled separately using Ewald Sums

and is not usually written with the other parameters in the potential energy function. The term $U_{Repulsive}$ represents a contribution from the Pauli Exclusion Principle. Some examples of how this is implemented are shown later. $U_{Attractive}$ accounts for the contribution from the van der Waals force between the electron clouds of different atoms. Some systems, especially organic systems, will account for covalent bonding through a U_{Bond} term. A U_{Angle} term accounts for bond angle interactions that may occur when the potential must account for greater than pair-wise interactions. Likewise $U_{Torsion}$ also accounts for complex interactions that may be necessary to model complex organic systems. The $U_{Non\text{-}Symmetry}$ term accounts for instances where interactions do not act equally in all directions. An example would be carbon in planes of graphite.

Potentials can be derived from empirical data or from more fundamental simulations (i.e. Ab Initio calculations using density functional theory). With empirical potentials well known fundamental material properties are calculated from a set of MD simulations and then compared to the known experimental values. The form of the potential may also be based on knowledge of the general form of a particular type of interaction potential. For example, in the often used Lenard-Jones and Buckingham potentials shown in Equations (3.2) and (3.3) there is an A/r^6 term that corresponds to the $U_{Attractive}$ van der Waals attraction between electron clouds.

$$V(r) = \frac{B}{r^{12}} - \frac{A}{r^6} \tag{3.2}$$

$$V(r) = B\exp(-Cr) - \frac{A}{r^6} \tag{3.3}$$

A repulsive term ($U_{Repulsive}$), that stems from the consequences of the Pauli exclusion principle and is caused by electron cloud overlap, is represented by an B/r^{12} term in the

Lenard-Jones potential and as Bexp(-Cr) term in the Buckingham potential, where A, B and C are all tunable constants. Both the Lenard-Jones and Buckingham potentials are pair-wise potentials that only calculated the potential energy between two atoms. The r term in Equations (3.2) and (3.3) represents the scalar distance between two atoms. The constants can be adjusted as needed until the MD simulations adequately reproduce the desired material properties. In addition to constants that affect short range forces, the charges on atoms in an ionic system can also be adjusted to account for the effect of charge screening. Conversely, the position dependent response of forces between atoms from a well converged Ab Initio simulation can be numerically fit to also produce potential energy functions for MD simulations. Regardless of what method is used to derive the potential energy function, the end form should mimic the true behavior of the simulated materials atoms. Much more detailed explanations of Molecular Dynamics are available elsewhere in references dedicated to the subject such as the paper by Ercolessi [29] and monographs by Haile [30] and Frenkel and Smit [31].

3.1.2 Correlation Functions

Correlation functions examine how a property of a system varies as a function of time or space in relation to some other property. The degree of interdependency or lack thereof between the two properties becomes the correlation function. When examining the dynamic evolution of a system, time correlations of certain properties that can be measured with atomistic simulation can often be related to different transport coefficients of materials. Correlation function relationships are also used to examine the time varying changes in the atomic structure of a system that are important in neutron scattering and the analysis of

diffusion mechanisms. Depending on the property being studied, Green-Kubo formulas, which involve integrating a correlation over time, or Einstein relations, which involve differentiating a correlation over time, are used to connect the trajectories of atomistic simulations to transport coefficients like viscosity, thermal conductivity, and diffusion. In general, any two time varying properties $A(t)$ and $B(t)$ can define a time correlation given by some function $C(t)$ as shown in Equation (3.4).

$$C(t) = \lim_{\tau \to \infty} \frac{1}{\tau} \int_0^\tau A(t_0) B(t_0 + t) dt_0 = \left\langle A(t_0) B(t_0 + t) \right\rangle \tag{3.4}$$

In Equation (3.4), $C(t)$ is the autocorrelation if A and B are the same quantity. Once $C(t)$ is known for set of properties given by $A(t)$ and $B(t)$ it can be transformed into the desired material property [30].

The diffusion coefficient can be found from applying the Einstein relation to the mean square displacement of a system of atoms. This relationship is shown in Equation (3.5).

$$D = \frac{1}{2d} \frac{\partial}{\partial t} \left\langle \left[r(t) - r(0) \right]^2 \right\rangle \tag{3.5}$$

In this equation, D is the diffusion coefficient, d is the dimensionality of the system, and $<[r(t)-r(0)]^2>$ is the mean square displacement of the system. When analyzing atomistic simulations, the slope of the mean square displacement as a function of time is divided by twice the dimensionality of the system. If the time behavior of the mean square displacement is not linear with time, this is a good indication that either the simulation has an error, or the diffusion in the system is in some way anisotropic. The mean square displacement relationship is used to find the self-diffusion of Uranium and Oxygen in UO_2 and noble gas fission products in both MD and KMC simulations.

Another useful time correlation is the velocity autocorrelation function (VACF). The phonon frequency distribution of a material and the diffusion of liquids can be derived from this function shown in Equation (3.6) where $v(t)$ is set of velocities for all atoms in the system under investigation. For a system in equilibrium the velocity autocorrelation function will decay to zero as time increases so that the diffusion coefficient is the integral of the velocity autocorrelation function as time goes to infinity divided by the dimensionality of the system.

$$VACF = \left\langle v\left(t - t_0\right) v\left(t_0\right)\right\rangle \tag{3.6}$$

The thermal conductivity coefficient of a system can be derived from the energy current autocorrelation function. The thermal conductivity coefficient is a measure of how well energy is convectively transported across a medium and how well phonons transfer energy through a system. The Green-Kubo relation connects thermal conductivity with a property called energy current ($\mathbf{J}(t)$) that can be found with MD simulations given the relation shown in Equation (3.7), where E_i is the total energy of each atom i of the N_{atms} total atoms in the system at some time t and $r_i(t)$ is the positions of each atom i at some time t. Energy current can be thought of as the rate at which energy moves from one part of a system to another. The energy current autocorrelation function conversion to thermal conductivity coefficient λ shown in Equation (3.8) where V is the volume of the system, k_B is Boltzmann's constant, and T is the temperature of the system. The use of this relation in MD programs is discussed in detail in section 3.3.3.

$$\mathbf{J}(t) = \frac{d}{dt}\left[\sum_i^{Natms} E_i(t)\bar{r}_i(t)\right] \tag{3.7}$$

$$\lambda = \frac{1}{3Vk_B T^2} \int_0^\infty dt \langle J(t)J(0) \rangle \tag{3.8}$$

The way a crystal structure changes with time can also be measured with time correlation functions, specifically the Van Hove correlation function. The dynamic properties of the crystal structure can also be related to diffusion, and they can be used to determine the structure factor in thermal neutron scattering calculations. Typically the Van Hove correlation function is split into two parts shown in Equation (3.9). The distinct part (G_d) is related to how the structure of a crystal surrounding an atom changes with time. The self part (G_s) determines the probability that an atom will be at some distance r from its time and space origin at some time t, and is calculated from the relationship shown in Equation (3.10) for a homogeneous uniform substance [30].

$$G(r,t) = G_s(r,t) + G_d(r,t) \tag{3.9}$$

$$G_s(r,t) = \frac{1}{N} \left\langle \sum_{i=1}^N \delta \left[r - |\mathbf{r}_i(0) - \mathbf{r}_i(t)| \right] \right\rangle \tag{3.10}$$

In Equation (3.10) r is a scalar distance away from the time and space origin, N is the number of atoms i in the system, and $\mathbf{r}_i(t)$ is the vector position of atom i at some time t. In practice G_s is constructed as a histogram where the delta function will equal 1 for a certain interval about a scalar distance r that is one of many equally spaced scalar distance bins from $r=0$ to a cut off radius. The cutoff radius is problem dependent and should be chosen as a distance beyond which the probability of the atoms under investigation has a very low probability of migrating beyond.

Examination of how the Van Hove correlation function changes with time can also provide insight into the physical processes that occur in a crystal. For instance, in a system that is diffusing by a vacancy migration mechanism a peak will form in the G_s term at the

first nearest neighbor and will increase in size as simulation time is increased. Smaller peaks will also begin to form at the 2nd and 3rd nearest neighbor positions etc. if the simulation is long enough. As simulation time progresses, G_s relates the structure of a system to the migration of individual atoms. It is possible to relate G_s to the diffusion coefficient by assuming a roughly Gaussian shape for G_s from which a relationship between mean square displacement and G_s can be found. This relationship is shown in Equation (3.11).

$$G_s(r,t) \approx \frac{1}{\left[\frac{4}{6}\pi\left\langle\Delta r^2(t)\right\rangle\right]^{3/2}} \exp\left[-\frac{r^2}{\frac{4}{6}\left\langle\Delta r^2(t)\right\rangle}\right] \tag{3.11}$$

Where $<\Delta r^2(t)>$ is the mean square displacement, it can be related to the diffusion coefficient using the Einstein relation shown in Equation (3.5). The link between the diffusion coefficient and G_s implies a link between diffusion and the dynamic atomic structure of a material, and emphasizes how microscopic processes significantly influence properties that can be observed macroscopically in experiment like the diffusion coefficient.

3.2 *Basic Properties for Uranium Dioxide MD Simulations*

Uranium Dioxide is an ionic material that has been used extensively as a fuel for light water reactors in the nuclear power industry. In addition to use in light water reactors, UO_2 has been used as the fuel kernel material in TRISO fuel for high temperature reactor designs. The uranium oxycarbide used in current generation US TRISO fuel kernels also contains a UO_2 phase. The crystal structure of UO_2 is the fluorite structure found in CaF_2. A schematic of a unit cell of the fluorite structure is shown in Fig. 3.2. The atomic positions seen in the unit cell picture are used to define the initial positions of atoms in a MD simulation.
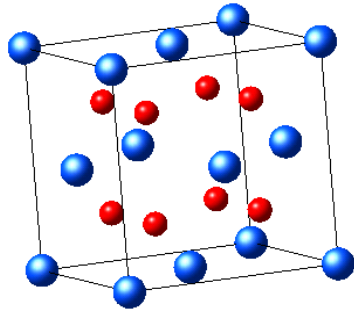
Fig. 3.2. The crystal structure of UO_2 (blue spheres represent U and red spheres represent O)

For an ionic solid such as UO_2, the potential function includes short range and long range (Coulomb) components to govern the interactions between atoms. There have been several UO_2 potential functions developed to simulate different physical properties. The short range potential functions tend to take on the Buckingham form shown in part A of the potential energy function shown in Equation (3.12). Part B of the equation is the Coulomb portion of the potential.

$$V_{ij}\left(r_{ij}\right) = \underbrace{A_{ij}\exp\left(-\frac{r_{ij}}{\rho_{ij}}\right) - \frac{C_{ij}}{r_{ij}^{6}}}_{A} \underbrace{- \frac{1}{4\pi\varepsilon_0}\frac{Z_iZ_j}{r_{ij}}}_{B} \tag{3.12}$$

The potential determines the forces between two atoms 'i' and 'j' based on the distance between the two (r_{ij}). The charge on the atoms ($Z_{i,j}$) can either be formal charges (+4 for U, -2 for O), or they can be set as partial charges. However, it is important to ensure that the net charge on a UO_2 molecule is zero. The value of the potential parameters A_{ij}, ρ_{ij}, C_{ij}, and $Z_{i,j}$ can be obtained by fitting to data obtained experimentally or possibly from more fundamental calculations. For example, data used in potential function validation include the thermal expansion coefficient, bulk modulus, and thermal conductivity.

3.2.1 Molecular Dynamics Codes

Three different Molecular Dynamics codes have been investigated for use in this research. Each code has various different benefits and weaknesses. Materials Explorer 4.0 is a commercially available MD code that incorporates a very user friendly graphical user interface in a Windows operating system [35]. While this program is a useful learning tool, its capabilities are limited. Materials Explorer lacks command line execution and input file manipulation that would allow a control script to intelligently control the execution of the code over long periods of time. Also since Materials Explorer is a commercial program the source code is not available. Modification of the source code is often necessary to derive more complex outputs from MD simulations like the heat current used in thermal conductivity calculations. Also portability of the program across several different systems (i.e. Windows, Linux, high performance computers) is not possible without the source code. Additionally Materials Explorer is not written to execute in parallel using several processors. To address these concerns the MOLDY MD code was investigated, and is now the primary MD code in use [36]. MOLDY is a general purpose MD code that is written in C. It supports many different potential energy functions, and different potential energy functions can be added without too much effort unlike Materials Explorer. The program can be run in all the different common ensembles such as NPT, NVE and NVT. It also comes with many different ancillary programs that assist with the interpretation of the MD results. An additional MD code has also been investigated. DL_POLY is another freely available MD code developed and supported by Daresbury Laboratory in the U.K. [37]. This code has the capability of running very large systems in parallel on large computer clusters and is written

in FORTRAN 90. DL_POLY_2.20 has been compiled and tested. One useful feature in DL_Poly for migration energy calculations is the ability to freeze the position of certain atoms in the system. Because of its ability to handle larger systems and installation on the NCSU High Performance Computing cluster, all larger MD systems were simulated using DL_POLY. The custom programs developed for thermal conductivity calculations are designed for MOLDY output, but they could be adapted to DL_POLY output forms if necessary.

3.2.2 Automatic Potential Optimization with MOLDY

Once MOLDY was successfully compiled, a script was written to optimize the parameters of the Buckingham potential for UO_2. A PYTHON script was written to perform this task. The script reads in the MOLDY control file, initial positions, potential parameters, and initial test parameters. It then executes MOLDY for a set of potential parameters to be tested. The results of the run are read and compared against the real physical parameters derived from experiment.

Three parameters were fit in the initial attempt to optimize the potential. The A and ρ terms for the U-O interaction, and the charge on the U ion for all interactions. These terms can be seen in Equation (3.12). This is the same strategy that was pursued by Morelon et al [38]. The justification for only modifying these three parameters follows. There is so much Coulomb repulsion between U ions that short term forces never have any effect, hence A, ρ, and C are not defined for the U-U interaction. In the U-O interaction the attraction is dominated by the coulombic term, so the C term for this interaction is zero. The Morelon study found little change in the simulation by modifying the O-O interaction terms so they

37

are not currently modified by the optimization script. In order to maintain charge neutrality, the charge on the oxygen ion must always be one half the opposite of the charge on the U ion, so the change in the O charge is always dependent on the Uranium charge.

For an initial test the potential was only optimized on the lattice constant of UO_2 at 300K and the lattice constant at 1500K. These temperatures span the conditions expected to be seen in the AGR tests. For each set of test parameters it was necessary to run two MD simulations under the NPT ensemble. At the conclusion of the runs, the lattice constants of the two simulations were extracted and analyzed. The initial parameters for this test were based on the Walker and Catlow potential parameters [39]. With just optimizing on the two physical properties the optimized potential was not too different from the original. The results of the optimization are shown in Table 3.1 and Table 3.2 below and compared to experiment [40], [41]. In the future the optimization control script can be expanded to other physical properties of UO2, and other potential parameters. However the current potential produces very good results for a wide range of physical parameters.

Table 3.1. Results of optimizing the UO_2 potential for lattice constant

Potential Parameters

U-O A	873.9018	eV
U-O ρ	0.403928	Å
qU	3.826355	e

Lattice Constant (Å)

	MOLDY	Experiment	% difference
300 K	5.4710	5.470	0.01798
1500 K	5.5378	5.541	0.06527

Table 3.2. Final Potential Parameters used for Remainder of Simulations

Interaction	A (eV)	ρ (Å)	C (eV Å⁶)
U-U	0.0	1.0	0.0
U-O	873.9018	0.40392759	0.0
O-O	50259.34	0.15285	72.653
qU (e)	3.826355		
qO (e)	1.913178		

The table header spans as: Potential Parameter over A (eV), ρ (Å), C (eV Å⁶).

3.3 *Validation of Optimized UO$_2$ Potential*

Several different well known thermo-physical properties of UO$_2$ were used to validate the optimized potential function. The thermal expansion coefficient and its pressure based corollary the bulk modulus were initially used. These simpler metrics were followed by the calculation of thermal conductivity which like diffusion is a transport coefficient. The results of these validation calculations are presented in the following sections.

3.3.1 Thermal Expansion

The thermal expansion of UO$_2$ has been examined using the optimized potential and the MOLDY code using a constant atom, pressure and temperature (NPT) ensemble. Simulations were run at 300 degree intervals for temperatures ranging from 300 to 2100 K. Each system consisted of 768 atoms run for 10 ps with 1 fs time steps. The lattice constants at each temperature were taken as the average lattice constant of the system at equilibrium. The results of the thermal expansion investigation versus literature values are shown in Fig. 3.3 [41], [42]. The literature values are based on an empirical fit to several different experiments. The current model is able to replicate thermal expansion over a wide range of

temperatures. The expected lattice coefficients from Reference [41] are given by Equation (3.13) for temperatures ranging from 273 K to 925 K and Equation (3.14) for temperatures ranging from 925 K to 3120 K, where L_{273} is the lattice coefficient at 273 K and T is the temperature in Kelvin.

$$L_T = L_{273}\left(0.9973 + 9.082 \times 10^{-6} T - 2.705 \times 10^{-10} T^2 + 4.391 \times 10^{-13} T^3\right) \qquad (3.13)$$

$$L_T = L_{273}\left(0.99672 + 1.179 \times 10^{-5} T - 2.429 \times 10^{-9} T^2 + 1.219 \times 10^{-12} T^3\right) \qquad (3.14)$$

3.3.2 Bulk Modulus

Once a model was established for thermal expansion it was important to validate the model against other physical properties. The bulk modulus represents a material's resistance to compression under a uniform pressure and was chosen since it could be considered a pressure based corollary to thermal expansion. Equation (3.15) was used to calculate the Bulk modulus by comparing the volume of the crystal at a reference pressure of 1 atm (P_1, V_1) to the volume of the crystal at much higher pressures (P_2, V_2). In general the bulk modulus should be fairly invariant under changes in pressure.

$$B = -\frac{(P_1 - P_2)}{\ln\left(V_1 / V_2\right)} \qquad (3.15)$$

For different pressures the bulk modulus was calculated to be between 180 and 200 GPa. Experiments have found the bulk modulus to range from 179 to 207 GPa at room temperature [38].
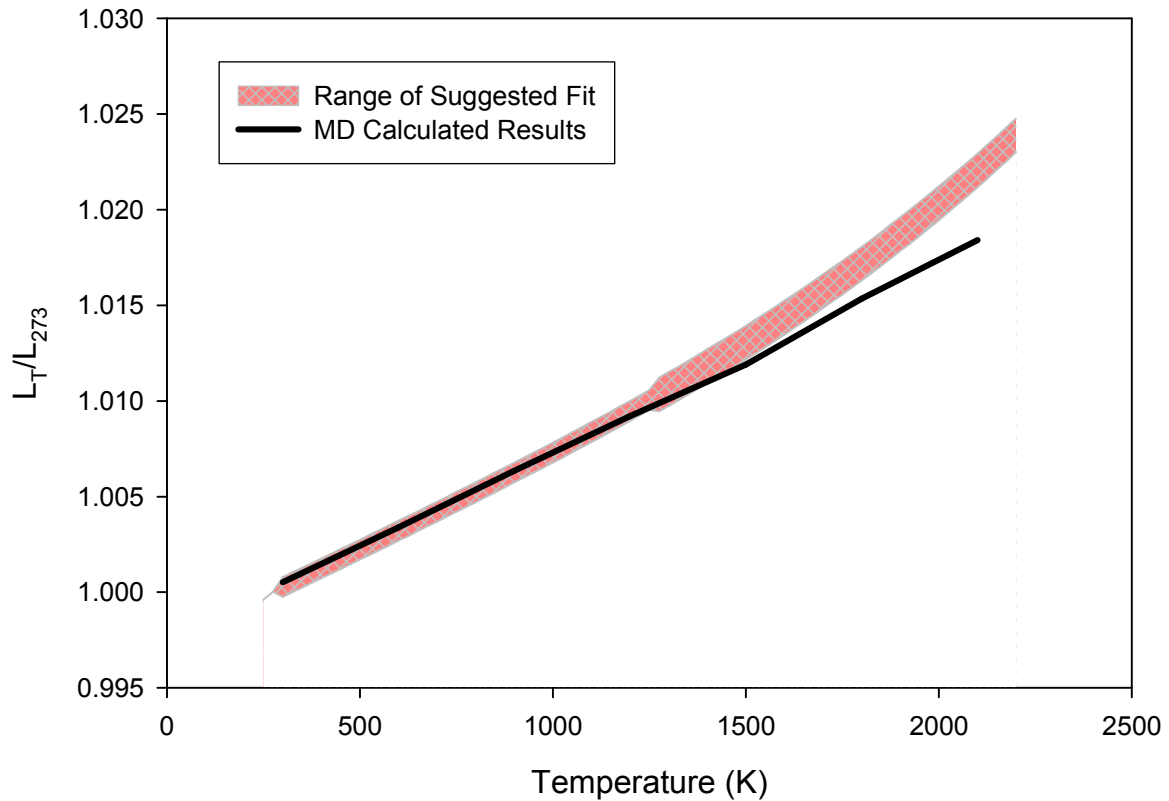
Fig. 3.3. Thermal Expansion of UO₂ as predicted from MD simulations. L_T and L_{273} refer to the lattice parameter at a temperature T and 273 K respectively.

3.3.3 Thermal Conductivity

MD simulations were also performed to calculate the thermal conductivity of UO₂ using the Green Kubo formulas and Equilibrium Molecular Dynamics. Thermal conductivity is challenging to calculate in MD, but since it is a transport coefficient it is a very good test of a model's (inter-atomic potential's) ability to replicate many different transport phenomena. The thermal conductivity coefficient λ is given by the Green Kubo relationship shown in Equation (3.16) below.

$$\lambda = \frac{1}{3Vk_B T^2} \int_0^\infty dt \langle J(t) J(0) \rangle \qquad (3.16)$$

Where V is the volume of the system k_B is the Boltzmann constant, T is the temperature of the system and $J(t)$ is the energy current, which approaches 0 as the system equilibrates. The calculation of $J(t)$ is complicated by the need to include Coulomb forces. The energy current can be thought of as the time derivative of sum of the energy of each atom 'i' (E_i) multiplied by the vector position of the ith atom (r_i).

$$\mathbf{J}(t) = \frac{d}{dt}\left[\sum_i^{Natms} E_i \vec{r}_i \right] \tag{3.17}$$

This expression with the chain rule becomes form seen in Equation (3.18) which breaks the energy current up into two convective and non-convective parts.

$$\mathbf{J}(t) = \underbrace{\sum_i^{Natms} \left(T_i + U_i - \hat{E}_i \right)\vec{v}_i}_{\text{Convective Term}} + \underbrace{\sum_i^{Natms} \vec{v}_i \vec{F}_i \vec{r}_i}_{\text{Non-Convective Term}} \tag{3.18}$$

In Equation (3.18), a Convective term consisting of the total energy of each atom (kinetic (T_i) plus potential (U_i)) that is subtracted from the average total energy per atom for the system ($\hat{E}_i$). The second set of terms from Equation (3.18) consist of the velocity of each atom at time t (v_i), the force acting on each i atom (F_i) and the vector position of each i atom (r_i). The result is only the excess energy of each atom is multiplied by the velocity of that atom which is representative of how the energy moves around the system. The kinetic energy term for each atom (T_i) is easily calculated from the velocity of each individual atom in the system. The potential energy for each atom is calculated from a combination of sources including the short range interactions from the problem specific inter-atomic potentials, the real space part of the Ewald sums, and the reciprocal space terms of the Ewald sums that are used to calculate the Coulomb interactions. The short range interactions combined with the

real space part of the Ewald sum can be quickly calculated. The reciprocal or Fourier space Ewald sums require more computation and are found from the following equation.

$$U_{reciprocal} = \underbrace{\frac{1}{\varepsilon_0 V} \sum_{k>0} \frac{1}{k^2} e^{-\frac{k^2}{4\alpha^2}} \left\{ \left| \sum_{i=1}^{N} q_i \cos(k \cdot r_i) \right|^2 + \left| \sum_{i=1}^{N} q_i \sin(k \cdot r_i) \right|^2 \right\}}_{\text{Fourier Space Term}} - \underbrace{\frac{\alpha}{4\pi^{\frac{3}{2}} \varepsilon_0} \sum_{i=1}^{N} q_i^2}_{\text{Self-Energy Term}} \quad (3.19)$$

In Equation (3.19), ε_0 is the permittivity of free space, V is the volume of the simulation cell, k is the reciprocal vector of the simulation unit cell, α is a convergence factor for the Ewald sums, N is the number of atoms in a system, r_i is the real space position of each atom i in the system, and q_i is the charge on atom i in the system. The equation also contains a self-energy term to account for energy contribution from the charge on the individual atoms.

The non-convective term in Equation (3.18) of the energy density is computationally expensive to compute as a result the need to calculate the force from every atomic interaction in the system. Additionally calculation of this term requires combining the force and the position of each atom into a tensor (S_{ab}), and then the vector velocity of each atom is multiplied by the tensor and summed over all atoms in the system. The detailed equations for this term are shown in Equations (3.20) and (3.21).

$$\mathbf{J}(t)_{Non-Convective} = \sum_{i}^{Natms} \sum_{j}^{Natms} \vec{v}_i \vec{F}_{ij} \vec{r}_i = \sum_{i=1}^{N} \mathbf{v_i} \begin{pmatrix} S_{xx} & S_{xy} & S_{xz} \\ S_{yx} & S_{yy} & S_{yz} \\ S_{zx} & S_{zy} & S_{zz} \end{pmatrix}, \quad (3.20)$$

$$S_{ab} = \frac{1}{2} \sum_{j \neq i}^{Natoms} \frac{a_{ij}b_{ij}}{\left|\mathbf{r}_{ij}\right|^2} \left[\begin{array}{l} \underbrace{F(r_{ij})}_{\text{short range}} + \underbrace{\frac{1}{4\pi\varepsilon_0} q_i q_j \left(\frac{erfc\left(\alpha\left|\mathbf{r}_{ij}\right|\right)}{\left|\mathbf{r}_{ij}\right|} + \frac{2\alpha}{\sqrt{\pi}} e^{-\alpha^2\left|\mathbf{r}_{ij}\right|^2} \right) - \cdots}_{\text{real space Coulombic}} \\[2em] \underbrace{\cdots - \frac{1}{4\pi\varepsilon_0} q_i \sum_{\mathbf{k}} \frac{k_a}{\left|\mathbf{k}\right|} \frac{k_b}{\left|\mathbf{k}\right|} \frac{4\pi e^{-\left|\mathbf{k}\right|^2/4\alpha^2}}{\left|\mathbf{k}\right|^2} \left(1 + \frac{\left|\mathbf{k}\right|^2}{4\alpha^2} \right) \times \cdots}_{\text{reciprocal space Coulombic}} \\[2em] \underbrace{\cdots \times \left(\cos\left(\mathbf{k}\cdot\mathbf{r}_i\right) \sum_{j=1}^{Natoms} q_j \sin\left(\mathbf{k}\cdot\mathbf{r}_j\right) - \sin\left(\mathbf{k}\cdot\mathbf{r}_i\right) \sum_{j=1}^{Natoms} q_j \cos\left(\mathbf{k}\cdot\mathbf{r}_j\right) \right)}_{\text{reciprocal space Coulombic}} \end{array} \right] \tag{3.21}$$

The S tensor is defined by the atomic positions, and the forces due to the Coulomb and short range potentials [43]. The term $F(r_{ij})$ represents the forces due to the short range inter-atomic potentials. In the equation for the tensor, the a and b terms are the x, y, z terms for the tensor that come from the x, y, z components of the r_{ij} vector between atoms i and j, and $\mathbf{r}_i$ is the real space vector position of atom i or atom j. The $k_{a,b}$ terms are the x, y, z components of the reciprocal lattice vector of the MD cell. In Equation (3.21), the reciprocal lattice vector is understood to be defined as

$$k_x = 2\pi \frac{a_y \times a_z}{a_x \cdot a_y \times a_z}; \quad k_y = 2\pi \frac{a_z \times a_x}{a_x \cdot a_y \times a_z}; \quad k_z = 2\pi \frac{a_x \times a_y}{a_x \cdot a_y \times a_z}, \tag{3.22}$$

where $a_{x,y,z}$ is the real space lattice vector of the MD cell. While the form used in Reference [43] is fundamentally what was used for this analysis, there were sign changes and coefficient manipulations that were applied to the published equations to create the above equations.

Calculating the heat current is a complex process, and a program was written to process the outputs of MOLDY simulations for this task. There are several programming pitfalls that can significantly increase computational time especially in the reciprocal space tensor terms.

When programming this technique, care should be taken to remove redundant calculations from loops such as the sums over all atoms j charge and position in the last line of Equation (3.21), calls to subroutines that can easily be inline coded should be eliminated (e.g. calling a dot product subroutine), and overall the total number of flops should be reduced where possible. After extensive testing which included benchmarking to program against Ar thermal conductivity simulations, UO_2 thermal conductivity results were produced. Simulations were performed with the optimized potential that is loosely based on the Walker-Catlow potential. The simulation time for each temperature was 10 ps with 1 fs time steps, and both NPT and NVT ensemble results were produced. The lattice constants for the NVT ensemble simulations were set based on the expected thermal expansion given in literature [41]. The results of the simulations are shown in Fig. 3.4 for NPT ensemble and Fig. 3.5 for NVT ensemble. The Calculations are compared to a suggested value fit of several different published sets of experimental data [41] and against the experimental results of Bates [44]. The calculated thermal conductivity values agree well with the experimental data. The NPT results range from about 5 to 44 % different from the suggested values with an average over estimation of about 22 %. The NVT results agree better with the suggested value and trend better with experiment as a whole than the NPT values. With the exception of the 300 K value, all of the NVT results overestimate the suggested values by less than 20%, and the suggested values have a recommended relative error of 10%. These results suggest that UO_2 is successfully being simulated by the current model.
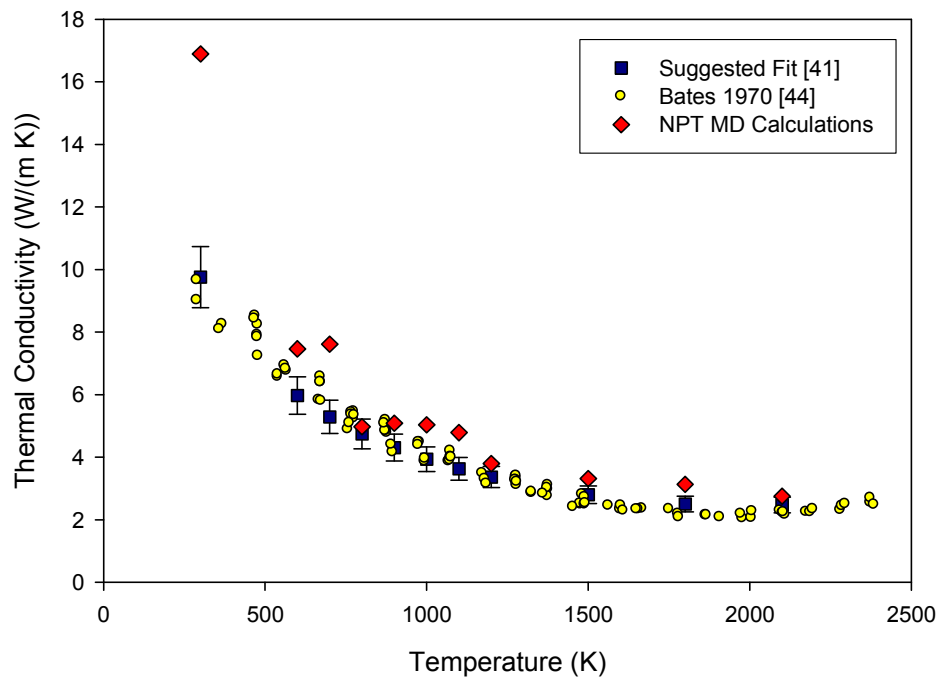
Fig. 3.4. Thermal Conductivity Calculations for NPT Ensemble with Experimental Data and a suggested fit to several sets of Experimental Data
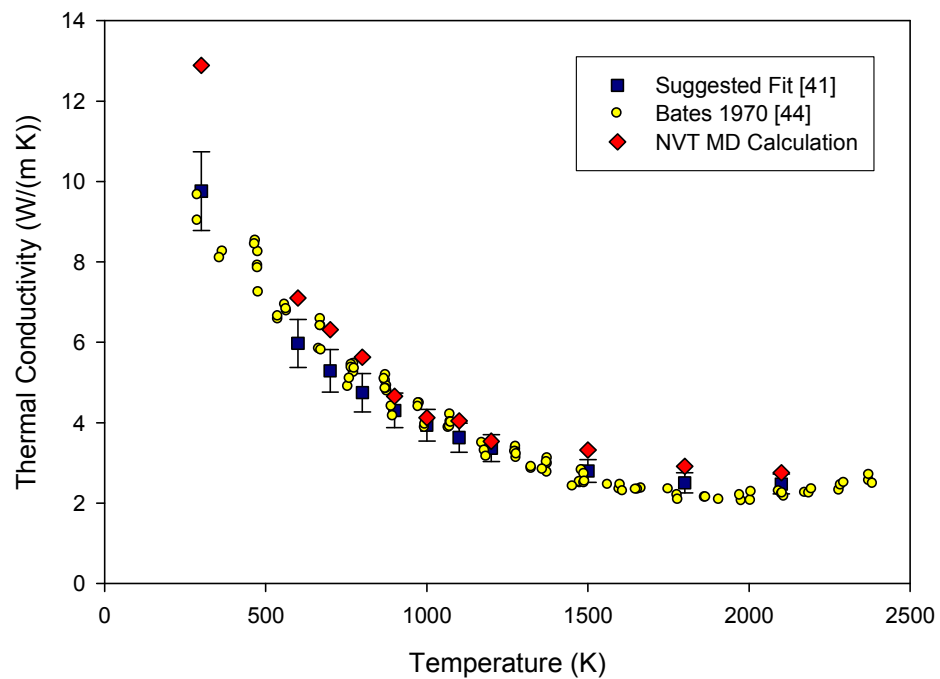
Fig. 3.5. Thermal Conductivity Calculations for NVT Ensemble with Experimental Data and a suggested fit to several sets of Experimental Data

3.4 *Summary of UO$_2$ Molecular Dynamics Model Testing*

A molecular dynamics model of UO$_2$ was created by modifying existing potentials from literature and comparing the models behavior to experimental data. The model was able to be generally applied across several different MD simulation packages. The MD model performed well against a wide variety of well known experimentally measured UO$_2$ properties. The model also performed well in a wide range of temperatures including the temperature ranges expected in TRISO fuel experiments. The thermal expansion, bulk modulus, and thermal conductivity numbers derived from this model allows for the confident extension of this model to simulating the diffusion phenomenon in UO$_2$. Both thermal conductivity and the diffusion coefficient are transport coefficients, so the quality performance of the UO$_2$ MD model with thermal conductivity is an encouraging factor in the expected performance for diffusion behavior. In the following chapter, the MD model developed in this chapter will be applied to exploring the diffusion of Kr and Xe through UO$_2$.

Chapter 4 Examining Diffusion with Atomistic Simulations

In the previous chapter, atomistic simulation was introduced, and a molecular dynamics model of UO_2 was developed. The MD model was tested against several different well known properties of UO_2 including thermal conductivity. The phenomena governing thermal conductivity and diffusion are similar, so the ability of the model to accurately reproduce thermal conductivity data suggest the model can be applied the many different diffusion processes in UO_2 including fission gas diffusion for Kr and Xe. Exploring the diffusion mechanisms of Kr and Xe in UO_2 requires knowledge of their interaction with UO_2. There are some MD potentials in literature that account for the interaction between UO_2 and the noble gases Kr and Xe [45]. These potentials were derived from theoretical first principles models of the interaction between Xe, Kr, U, and O in UO_2. However, before the specific problem of Kr and Xe diffusion in UO_2 can be addressed, it is important to first examine where Xe and Kr are located in the crystal matrix of UO_2. Given the location of Kr and Xe, the most probable Kr and Xe migration mechanism will be discussed. An important component of the proposed Kr and Xe migration mechanism involves the migration of O and U vacancies through the UO_2 crystal. A detailed analysis of O and U self-diffusion in UO_2 has been performed to better understand the essential function that these phenomena play in noble gas fission product diffusion. Additional exploration will include a review of the theory of the diffusion process, study of the relationship between diffusion and atomic structure with the van Hove correlation function, and discussions on how deviations in UO_2 microstructure (e.g. grain boundaries and radiation damage) can affect diffusion.

4.1 *The Location and Migration of Xe and Kr Fission Fragments in UO$_2$ Fuel*

Nuclear reactors utilize the fissile nature of heavy actinide metals like Uranium, Plutonium, and Thorium to create heat for power generation. In many reactors including light water reactors and gas cooled High Temperature Reactors uranium metal is made into a ceramic typically UO$_2$. The properties of UO$_2$ are very beneficial for the nuclear reactor environment. The melting temperature of UO$_2$ is very high around 3120K. The crystal structure of UO$_2$ is the fluorite crystal structure where the U atoms are set in an FCC configuration and surrounded by the Oxygen atoms on a simple cubic sublattice. The resulting structure has a large octahedral vacancy in the center of the cubic configuration that can easily incorporate many types of fission products. The retention of every fission product is not however possible especially the noble gas fission products. Krypton and Xenon fission fragments are created internally in the atomic matrix of UO$_2$ fuel during irradiation like other fission products. However, the process through which Kr and Xe end up trapped in the fuel and the eventual diffusion of the gas out of the fuel matrix involves several steps starting with the fission event itself, precursor decay, trapping and migration. Each of these steps is important in understanding Kr and Xe diffusion experiments and simulations.

4.1.1 Thermodynamic Picture of Diffusion

Before the specific case of Kr and Xe in UO$_2$ is discussed, it is useful to review some key fundamental concepts from basic material science. Classical thermodynamic rate processes such as diffusion can be described by Boltzmann statistics using the following equation.

$$R = R_0 \exp\left(-Q/kT\right) \tag{4.1}$$

Where R is the rate that a system moves from one state to another through some process, R_0 is a pre-exponential term that is dependent on the geometry of system and other crystal properties, additionally it can also be related to the entropy of the system. The exponential is a Boltzmann factor where k is the Boltzmann constant, T is the temperature of system and Q is the activation energy of the process being observed. The Boltzmann factor represents the relative probability of atoms in the system achieving some energy greater than an energy barrier Q that controls the process. With some minor manipulation, Equation (4.1) becomes

$$-kT \ln R = Q - kT \ln R_0 . \tag{4.2}$$

The manipulated equation can then be related to classical thermodynamics using the Boltzmann equation and the definition of Gibb's free energy (G).

$$S = k \ln W = k \ln R_0 \tag{4.3}$$
$$G = H - TS \tag{4.4}$$

Where S is the entropy of the system, and W is the number of ways the atoms of the system can be arranged. Combining Equations (4.2), (4.3) and (4.4) implies a link between the thermodynamics of set states and the rate process that links the states through Equation (4.5).

$$G = -kT \ln R = Q - kT \ln R_0 \tag{4.5}$$

From the above equation, there are clear links between the activation energy Q and the enthalpy of the system, and there is a link between the pre-exponential term R_0 and the entropy of the system [46].

4.1.2 Basic Atomic Diffusion Theory

The migration of atoms around a system is described by a single fundamental parameter known as the diffusion coefficient. The diffusion coefficient is defined by Fick's law in Equation (4.6), where the current of atoms across some surface J is equal to the opposite of

the diffusion coefficient D multiplied by the gradient of the concentration of the migrating species C.

$$J = -D\nabla C \tag{4.6}$$

Essentially the magnitude of the diffusion coefficient is proportional to the mobility of the migrating species in some system under investigation. The following section describes the components of the diffusion process in detail.

In addition to the thermodynamic Boltzmann statistics driven view of diffusion as a rate process, diffusion can also be understood by examining system behavior at an atomic level and then scaling that behavior up to the bulk system using thermodynamic relationships. In the atomic picture of diffusion atoms can be thought of as vibrating about the ideal the crystal lattice position. Occasionally the atoms will acquire enough energy to break through the potential energy between two possible atomic positions in the crystal lattice. The atoms can jump from their position to several different possible positions with some probability based on the energy barrier between the two positions, the temperature of the crystal and the frequency of the atomic vibrations. The possible jump positions include interstitials, nearby vacancies, or exchanging position with neighboring atoms. If a system is allowed to evolve for a sufficient amount of time, the atoms in the system will take a random walk through the crystal structure. The trajectory of the atoms can be used to calculate the diffusion coefficient of a group of atoms through the Stokes-Einstein relationship seen in Equation (4.7).

$$D = \frac{1}{2d}\frac{\partial}{\partial t}\left\langle \left[r(t) - r(0)\right]^2 \right\rangle \tag{4.7}$$

Where D is the diffusion coefficient, d is the dimensionality of the system, and $<[r(t)-r(0)]^2>$ is the mean square displacement of the system. For a 3 dimensional system d is 3 and the limit of the mean square displacement is often taken as the slope of a linear least squares fit to the mean square displacement as a function of time.

For a more fundamental example, consider the case of vacancy diffusion through a crystalline solid. The diffusion coefficient of some atom 'a' by vacancy assisted diffusion is determined by the equilibrium concentration of vacancies, the migration energy of the vacancies after they are formed, the fundamental jump attempt frequency of the crystal, and the crystal geometry. These terms are grouped in Equation (4.8) where each term represents a contribution from vacancy concentration $f(C_v)$, migration energy $f(E_m)$, geometry $f(a_0)$ and attempt frequency $f(\omega)$.

$$D_a^v = f(C_v) f(E_m) f(a_0) f(\omega) \tag{4.8}$$

The concentration of vacancies can be related to macroscopic thermodynamic properties through a change in the Gibbs free energy of the system. For a system of N atoms with N_v vacancies at equilibrium the change in Gibbs free energy is given as the following equation.

$$G(N+N_v) - G(N) = H(N+N_v) - H(N) - T(S(N+N_v) - S(N)) \tag{4.9}$$

Where $H(N)$ represents the enthalpy of the system, T represents the system temperature in Kelvin, and $S(N)$ represents the entropy of the system. At equilibrium the Gibbs free energy of a system held at constant temperature and pressure (p) is a minimum, which implies.

$$\left(\frac{\partial G}{\partial N_v}\right)_{T,p} = 0 \tag{4.10}$$

The change in enthalpy is assumed to be the amount of energy required to move an atom from the interior to the crystal surface (i.e. the formation energy ($E_{f,v}$)) and is assumed to be

constant for every additional vacancy as long as $N_v \ll N$. Equation (4.9) can then be rewritten using the previous assumptions and Equations (4.3).

$$G(N+N_v)-G(N) = N_v E_{f,v} - kT\left(\ln W(N+N_v) - \ln W(N)\right) \tag{4.11}$$

$$W = \frac{(N+N_v)!}{N_v! N!} \tag{4.12}$$

$$G(N+N_v)-G(N) = N_v E_{f,v} - kT\left(\ln(N+N_v)! - \ln N_v! - \ln N! - \ln\frac{N!}{N!}\right) \tag{4.13}$$

Using the approximation that for large x, $\ln(x!)=x\ln(x)$

$$G(N+N_v)-G(N) = N_v E_{f,v} - kT\left((N+N_v)\ln(N+N_v) - N\ln N - N_v \ln N_v\right) \tag{4.14}$$

Then taking the equilibrium condition from Equation (4.10) and taking the derivative

$$0 = E_{f,v} - kT\left(\ln(N+N_v) - \ln N_v\right) \tag{4.15}$$

Rearranging terms yields the concentration of vacancies (C_v)

$$f(C_v) = C_v = \frac{N_v}{N+N_v} = \exp\left(-\frac{E_{f,v}}{kT}\right) \tag{4.16}$$

The same kind of analysis can be applied to other types of crystal point defects such as divacancies to find their respective thermal concentrations as a function of formation energy and temperature.

The contribution to diffusion from migration energy can be represented as a Boltzmann factor, which was discussed in Section 4.1.1, where E_m is the barrier to atoms moving into the lattice site occupied by the vacancy.

$$f(E_m) = \exp\left(-\frac{E_m}{kT}\right) \tag{4.17}$$

The geometry term is the square of the jump distance a_0, and the jump frequency is determined from the fundamental vibration of the atom in the crystal as modified by the entropy of motion in the crystal (S_m).

53

$$f(a_0) = a_0^2 \tag{4.18}$$

$$f(\omega) = v_0 \exp\left(\frac{S_m}{k}\right) \tag{4.19}$$

The Diffusion coefficient for vacancies is then equal to

$$D_v = \underbrace{a_0^2 v_0 e^{\left(\frac{S_m}{k}\right)}}_{1} \underbrace{e^{-\frac{E_m}{kT}}}_{2} \tag{4.20}$$

Where v_0 is the fundamental vibration of the atom in the crystal, this value is often taken as the Debye frequency of the atom in the crystal. An alternative value could come from the phonon frequency distribution of the crystal, or often a general order of magnitude estimate of 10^{13} Hz is used. The entropy term is often ignored because it is hard to calculate from experiments and is close to unity for most materials. Note that as was discussed in the previous section Equation (4.20) follows the general form for kinetic rate processes given in Equation (4.1), where part 1 of Equation (4.20) relates to the R_0 and is related to entropy as suggested by Equation (4.5) and part 2 of Equation (4.20) relates to the activation probability of the diffusion process [13].

It is important to note that there is a difference between the diffusion coefficient of individual point defects and the diffusion of the atoms that migrate by those mechanisms. Point defects (vacancies and interstitials) will diffuse according to the model laid out in Equation (4.20). The actual atoms in the crystal will diffuse according to the diffusion coefficient for the applicable point defect multiplied by the probability ($p_{v,i}$) that the point defect exists as a nearest neighbor. For vacancies and interstitials the probability is simply the concentration of defects as determined by the formation energy of the defect and

Equation (4.16). Equation (4.21) represents the diffusion of some atom 'a' by a vacancy mechanism.

$$D_a^v = a_0^2 v_0 e^{\left(\frac{S_m}{k}\right)} p_v e^{-\frac{E_m}{kT}} = \underbrace{a_0^2 v_0 e^{\left(\frac{S_{m,v}}{k}\right)}}_{1} \underbrace{e^{-\frac{E_{f,v}}{kT}}}_{2} \underbrace{e^{-\frac{E_{m,v}}{kT}}}_{3} \tag{4.21}$$

Part 2 of the equation represents the probability that the point defect mechanism exists as a nearest neighbor to any atom in the system. By exchanging the vacancy entropy, formation energy and migration energy with the applicable interstitial values Equation (4.21) can also apply to the interstitial migration mechanism [47].

In experimental analysis, the convention is to plot diffusion coefficients on a log scale versus the inverse of temperature. This form is called an Arrhenius plot after, which is named after the Swedish chemist Svante Arrhenius who used the plots to describe reaction rates. From the Arrhenius plot, the diffusion coefficient is often modeled more simply as shown in Equation (4.22) in experimental interpretation.

$$D = D_0 \exp\left(\frac{E_D}{kT}\right) \tag{4.22}$$

Where the energy of diffusion (E_D) is taken as the slope of a fit from an Arrhenius plot, and the D_0 pre-exponential factor is taken from the intercept of the fit. It is important to differentiate E_D from E_m and E_f if possible. In the literature, migration energy, formation energy, and energy of diffusion are not carefully distinguished and are sometimes used interchangeably. The distinction between the 3 energies becomes especially important when observing systems that contain point defects that were not thermally generated. While the activation energy term (E_D) explains how diffusion changes with temperatures, the pre-exponential factor is generally useful for examining the magnitude of diffusion over all

55

temperatures. Aspects that can influence the pre-exponential factor in diffusion generally deal with the amount of free space in a crystal (i.e. vacancies) and the fundamental frequency that an atom vibrates at in the crystal. Both these properties can be affected by local changes in crystal structure such as radiation damage and grain boundaries.

The Arrhenius plot is an important construct used to elucidate relationships between kinetic processes and concepts from thermodynamics [46]. As was discussed earlier in Section 4.1.1 with Equations (4.1) and (4.5) a kinetic process like diffusion in Equation (4.22) can be connected to thermodynamic principles. The Arrhenius plot is useful in observing and explaining many phenomenon and the underlying reasons for the temperature behavior of different phenomenon in rate processes especially diffusion. The slope of the Arrhenius plot is related to the activation energy required for a process to proceed, and the intercept of a set of data is related to the magnitude of a process. The intercept is most closely related to the atomic structure of the system being studies and is influence by such factors as geometry and the entropy of the system. An Arrhenius plot with two separate slopes indicates competing processes that have different activation energies such as is the case with non-thermal vacancies discussed later in this section. Arrhenius plots will be used extensively throughout the following chapters to examine diffusion and the different processes that influence its behavior.

Crystal systems with non-thermal point defects will exhibit different regions of diffusion coefficient behavior depending on the temperature of a system and the processes taking place inside a particular crystal. The energy of diffusion (E_D) may be equal to the sum of the migration energy and the formation energy (E_m+E_f) or may just be equal to the migration

energy (E_m). For example assume a system where $E_f > E_m$ as is normally the case, and assume there is some concentration of non-thermal vacancies C_{nt}. The vacancy assisted diffusion of some atom 'a' (D_a^v) can be described by the following equations.

$$D_a^v = D_{a,0}^v C_v e^{-\frac{E_{m,v}}{kT}} = D_{a,0}^v \left(e^{-\frac{E_{f,v}}{kT}} + C_{nt} \right) e^{-\frac{E_{m,v}}{kT}} \tag{4.23}$$

$$D_a^v = \underbrace{D_{a,0}^v e^{-\frac{E_{f,v}}{kT}} e^{-\frac{E_{m,v}}{kT}}}_{1} + \underbrace{D_{a,0}^v C_{nt} e^{-\frac{E_{m,v}}{kT}}}_{2} \tag{4.24}$$

Given the previous assumptions, at high temperatures where the concentration of thermally created vacancies is much larger than C_{nt} the Arrhenius behavior of the diffusion coefficient will be dominated by the formation energy terms from part 1 of Equation (4.24). At lower temperatures the concentration of thermal vacancies will be much lower than the non-thermal concentration, and the Arrhenius behavior of the diffusion coefficient will follow part 2 of Equation (4.24) leading to a slope that corresponds to E_m. The effect of some non-thermal concentration on an Arrhenius plot can be seen in Fig. 4.1. The source of non-thermal vacancies could be from a variety of sources such as a non-stoichiometric composition of the crystal, impurities of different valence in the crystal like Ca (+2) in NaCl (Na=+1), or radiation damage. Similar arguments could be applied to interstitial diffusion in the presence of a non-thermal interstitial concentration [13].
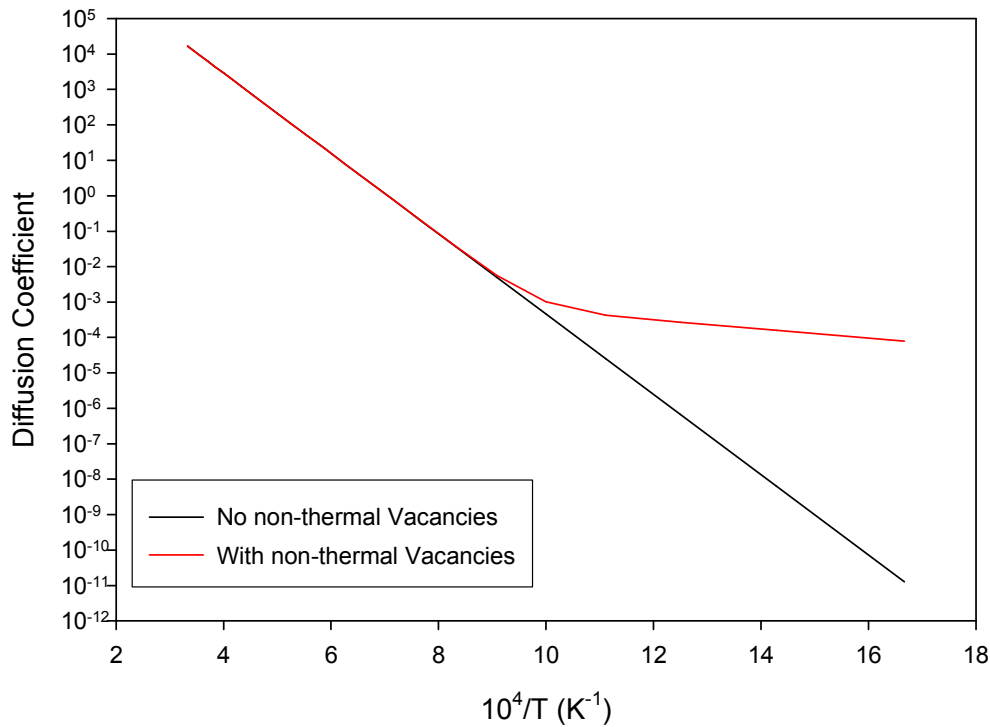
Fig. 4.1. Arrhenius Behavior of vacancy assisted Diffusion Coefficient with non-thermal vacancies and without non-thermal vacancies

Often the experiments that are performed to measure diffusion in a crystal are carried out by using a tracer that is chemically identical to the material being studied, but can be easily tracked after some time has passed. For example the self-diffusion of O in UO_2 was studied by enriching samples with O-18 in wafers of UO_2 that were then bound to un-enriched wafers and annealed. When the diffusion of all atoms by some mechanism is considered the random walks the atoms take are uncorrelated. However consider vacancy migration, after an atom hops from one site to the next all the atoms surrounding a defect will vibrate about their equilibrium site at a rate much higher than the rate of the next jump into the vacancy, and each atom near the vacancy has an equal chance of moving into the vacancy. However when diffusion is measured using a tracer, after a tracer atom moves via a vacancy it is more

58

likely to retrace its steps and return to its original position as its next step than to move 'forward'. Therefore the tracer random walk will be correlated for the vacancy mechanism resulting in a smaller diffusion coefficient for tracer atoms than for the bulk atoms. The likelihood of correlated diffusion is related to the number of nearest neighbor atoms in the crystal, where fewer nearest neighbors result in more correlated tracer migration. For simple cubic crystals the correlation factor or Haven coefficient f is 0.65311, for fcc crystals it is 0.72722, for bcc it is also 0.72722 when the migration mechanism is vacancy defects. The diffusion coefficient for tracer diffusion is directly proportional to the correlation factor multiplied by the bulk diffusion coefficient [47].

4.1.3 The Fission Process Effect on Noble Gas Location in UO$_2$

When a nucleus undergoes fission, it splits into two roughly 1/3 A and 2/3 A pieces called fission fragments and some excess neutrons. The kinetic energy of the fission fragments account for roughly 170 of the 200 MeV of energy released from a fission event. This energy results in fission fragments having a range on the order of 10 μm in the fuel which is a significant distance in terms of the atomic matrix of UO$_2$ [13]. The fission fragment nuclei are rich in neutrons leading them to decay through β- and β- plus a neutron events. It is important to note that many Kr and Xe fission products are produced primarily from the β- decay chains not directly from fission in general the longer the half-life the smaller the direct fission contribution. Table 4.1 below shows the direct and cumulative yields of different fission product isotopes of Kr and Xe [48].

A fission event creates a large amount of damage in the atomic fuel matrix in the vicinity of the event. However as the kinetic energy is dissipated through the fuel most of the

59

damage is repaired as the remaining U and O atoms rearrange themselves back into the standard fluorite structure. This property of UO_2 is one of the reasons why it makes such a good material for nuclear reactor fuel. In process of thermalizing the fission fragments have a high probability to leave their own damage and enter a relatively undisturbed section of the fuel. Additionally the primary fission fragment is often not Kr or Xe as highlighted in Table 4.1. Therefore the particle can often diffuse ~100Å as precursor elements such as I or Br which are soluble in UO_2 before they decay to a noble gas [49]. In TRISO fuel the average grain is 10 – 20 μm in diameter, when considering the range of fission fragments (10 μm) it is highly likely that not only will the fission fragments leave the general vicinity of the primary fission damage it will leave the crystal grain in which it was produced [50].

Table 4.1. Fission Yields of Kr and Xe Fission Products

Isotope	Half Life	Direct Fission Yield (%)	Cumulative Fission Yield (%)
85Kr-m	4.48 h	0.0059	1.2900
87Kr	1.27 h	0.4630	2.5600
88Kr	2.84 h	1.7300	3.5500
89Kr	3.15 m	3.4400	4.5100
90Kr	32.3 s	4.4000	4.8600
91Kr	8.6 s	3.1600	3.3500
133Xe	5.243d	0.0007	6.7000
135Xe-m	15.3 m	0.1780	1.1000
135Xe	9.10 h	0.0785	6.5400
137Xe	3.82 m	3.1900	6.1300
138Xe	14.1 m	4.8100	6.3000
139Xe	39.7 s	4.3200	5.0400

4.1.4 Trap Sites for Kr and Xe in UO_2 Fuel

When a Xe or Kr fission fragment comes to rest there are several different possible locations in the fluorite structure of UO_2 that could accommodate the atoms. The primary

defect structure in UO_2 is Frenkel pairs, but Schottky defects formed from one U and two O vacancies will form in UO_2 at high temperatures and with radiation damage [45]. The likelihood of a noble gas fission product becoming trapped in a particular type of vacancies left by Frenkel pairs or Schottky defects can be evaluated using Molecular Dynamics. The level of non-stoichiometry in the fuel will also influence the preferred trapping site. The UO_2 in nuclear reactor fuel is formulated as close to stoichiometric as possible. Under operating conditions, UO_2 is slightly hyper-stoichiometric (UO_{2+x}), however pockets of hypo-stoichiometric UO_2 will exist in the fuel due to temperature gradients in the fuel [49].

4.1.5 Incorporation Energy

The favored site for Xe or Kr can be determined from incorporation energy simulations performed in Molecular Dynamics calculations or inferred from experimental observations. Trap sites are identified by the energy required to substitute the noble gas atoms into different crystal lattice vacancy and interstitial formations. The MD model developed for this work was used to calculate the energy difference between two different crystal configurations. Several different types of vacancies were considered for the UO_2 crystal including Oxygen or anion vacancies, Uranium or cation vacancies, vacancy structures consisting of U and O vacancies, neutral Schottky or tri-vacancies consisting of U and 2 O vacancies, and tetra-vacancies consisting of 2 U and 2 O vacancies. The formation energy of each of these vacancies is defined as the total energy of the system containing some defect less the total energy of the perfect crystal as seen in Equation (4.25).

$$Formation\ Energy = E_{\text{system with defect}} - E_{\text{perfect crystal}} \qquad (4.25)$$

The energy required to incorporate an atom into a preexisting vacancy can also be calculated from MD simulations by subtracting the total energy of a system containing the fission product in a defect structure by the total energy of a system that contains the empty defect structure. This value is defined as the "Incorporation Energy" as seen in Equation (4.26).

$$Incorporation\ Energy = E_{with\ Filled\ Defect} - E_{with\ Empty\ Defect} \qquad (4.26)$$

To calculate the Incorporation Energy from MD simulations, the difference between the total energy of the two states was taken as the difference between the time averaged total system energy of the MD systems after the simulations had achieved equilibrium. When Kr and Xe are included in the MD simulations their interactions with U and O must also be defined by a potential energy function. The Kr and Xe potentials developed by Grimes [45] were used in the MD simulations for this work and can be found in Table 4.2. The form of the potentials is the same as the form of the U and O atom potentials seen in Equation (3.12).

Table 4.2. Potential Parameters for Kr and Xe Interactions with U and O atoms of UO_2 [45]

Interaction	Potential Parameter		
	A (eV)	ρ (Å)	C (eV Å^6)
Kr-U	5912.78	0.3191	50.34
Kr-O	800.38	0.3888	55.13
Xe-U	6139.16	0.3395	71.84
Xe-O	598.00	0.4257	108.38

A negative incorporation energy indicates that an atom is soluble in a defect structure, while a positive incorporation energy indicates that energy is required to integrate the atom into the defect structure. A positive incorporation energy also indicates that the atom will only stay in the fuel matrix as long as the barrier to diffuse out remains to prevents the migration of the

atom. When several defect configurations are considered the structure with the lowest incorporation energy is considered the preferred trap site for that atom in the surrounding material. Several different studies [45][51][52][53][54][55] and this work have examined the incorporation energy of Xe and Kr in UO_2 using either MD or Ab Initio simulation techniques. Some of these values are present in the Table 4.3. Nicoll et al did not consider Kr in their calculations.

Table 4.3. Calculated Incorporation Energies for Kr and Xe

Defect	This Work		Grimes [40]		Nicoll et al [46]	
	Xe Inc E (eV)	Kr Inc E (eV)	Xe Inc E (eV)	Kr Inc E (eV)	Xe Inc E (eV)	Kr Inc E (eV)
V_O	14.53	11.32	13.34	9.93	15.15	--
V_U	4.82	3.60	4.99	3.79	5.83	--
V_{UO}	4.18	3.08	2.84	2.39	4.39	--
V_{UO2}	3.65	2.70	1.16	1.09	3.3	--
V_{U2O2}	3.93	3.08	2.00	1.33	3.43	--
Interstitial	17.21	13.63	17.23	13.31	18.67	--

The neutral tri-vacancy (Schottky) defect composed of one U and two Oxygen atoms is the most stable defect structure for Xe found in preexisting trap sites in the fuel.

The calculation of the incorporation energy of Kr and Xe into the defects only accounts for the behavior of the fission products in preexisting defects caused by either temperature or radiation damage. As more and more fission products are built up in the fuel matrix all of the pre-existing will be filled and the fission products must begin forming their own defects. The energy required to form the defect and incorporate the fission product is called the "Solution Energy" and is equal to the incorporation energy plus the equilibrium solution site formation energy. The later part is taken from a combination of different energies including the Oxygen Frenkel Pair formation energy, the Schottky defect formation energy and the binding energies of the different defects [45]. When the creation of different defect structures is

considered, the non-stoichiometry of the fuel must also be taken into account. More specifically the abundance of oxygen vacancies or interstitials will affect the amount of energy required to trap the fission product. For example in UO_{2-x} there is an excess of oxygen vacancies, therefore a fission product can be accommodated into an O vacancy without the need to displace any atoms. However in UO_{2+x} there is excess oxygen in the fuel matrix at the octahedral interstitial sites, so to trap a fission product in an O vacancy a Frenkel pair must also be formed. The calculation method for each site formation energy type can be found in Reference [51].

Table 4.4. Site Formation Energy Formula

Vacancy Defect Formation	UO_{2-x}	UO_2	UO_{2+x}
O	0	$0.5\,E_f$	E_f
U	E_s	$E_s - E_f$	$E_s - 2E_f$
UO	$E_s - B_{dv}$	$E_s - 0.5\,E_f - B_{dv}$	$E_s - E_f - B_{dv}$
UO_2	$E_s - B_{nt}$		
U_2O_2	$2E_s - B_{tv}$	$2E_s - E_f - B_{tv}$	$2E_s - 2E_f - B_{tv}$

E_f – O Frenkel Pair formation energy, E_s – Schottky defect formation energy,
B_{dv} – divacancy binding energy, B_{nt} – neutral tri-vacancy binding energy,
B_{tv} – tetra-vacancy binding energy

Table 4.5. Site Formation Energy for this Work

	Trap Solution Energy					
	Xe			Kr		
Defect	UO_{2-x}	UO_2	UO_{2+x}	UO_{2-x}	UO_2	UO_{2+x}
O	14.53	17.97	18.20	11.32	14.76	18.20
U	18.15	11.27	<u>4.39</u>	16.93	10.05	<u>3.17</u>
UO	14.27	10.83	14.27	13.17	9.73	13.17
UO_2	<u>8.57</u>	<u>8.57</u>	8.57	<u>7.62</u>	<u>7.62</u>	7.62
U_2O_2	21.71	14.83	7.95	20.86	13.98	7.10
Interstitial	17.21	17.21	17.21	13.63	13.63	13.63

With these modifications to the incorporation energy seen in Table 4.5, this work shows the neutral tri-vacancy will still be the preferred trap site for hypostoichiometric and stoichiometric UO_2 when fuel conditions require the formation of extrinsic defects to trap

noble gas fission products. However for hyperstoichimetric UO_2 the U vacancy will be the preferred trap site. The work of Grimes suggests that the neutral tri-vacancy is still the preferred trap site for Xe and Kr in hypostoichiometric UO_2. For stoichiometric UO_2 the UO divacancy along with the neutral tri-vacancy may be a preferred trap site for both Kr and Xe. For hyperstoichiometric UO_2 the preferred trap site for Kr and Xe is the uranium vacancy [45]. However, the work of Jackson and Catlow suggests that the neutral tri-vacancy is the preferred trap site for all stoichiometries of UO_2 [51]. Given the simulations suggesting the tri-vacancy as the preferred trap site, the suggested migration pathway to be discussed subsequently in Section 4.1.6 seems probable. However this migration path requires diffusion through the Uranium sub-lattice and the Oxygen sub-lattice of the UO_2 crystal. In the sections following the migration mechanism, the ability of MD to capture diffusion of both the O and U species by examining the self-diffusion of O and U in UO_2 with MD will be explored.

4.1.6 Migration Mechanism

The migration mechanism of noble gas fission products in UO_2 has been studied from both experimental and theoretical perspectives [55][56][57][58][59]. Multiple thermal migration mechanisms have been proposed for Kr and Xe trapped in the tri-vacancy sites of UO_2, and there is no strong experimental evidence that directly identifies an exact migration mechanism [13], [52]. Additionally, it should also be noted that in addition to thermal diffusion there is some athermal diffusion of Kr and Xe due to fission spikes disturbing the crystal lattice of UO_2 [59]. In part the migration mechanism will be influence by the trap size of the fission products in the fuel. In spite of disagreement in the preferred trap site in the

stoichiometric flavors of UO_2 between different studies. The studies do agree that the Uranium vacancies in some form are part of the trap site, therefore their movement will be important in defining the migration mechanism of the fission products in the fuel. One proposed migration mechanism involves the trapped fission product jumping from a filled trap site to a nearby trap site [60][61]. A second mechanism involves the noble gas fission product trapped in the preferred tri-vacancy trap site. The Kr or Xe then moves about the system with the assistance of additional U vacancies forming tetra-vacancy clusters, rearranging the trap site, and then disassociating back to a tri-vacancy and U vacancy [45][55]. It is the latter mechanism that became the accepted Xe migration mechanism in recent decades.

The accepted mechanism for noble gas diffusion was investigated in this work. It involves the Schottky defect or neutral tri-vacancy and an additional U vacancy. This process is illustrated in Fig. 4.2, and the steps are labeled (a) to (d). In this mechanism the fission product (Xe or Kr) is initially trapped in the tri-vacancy (a). A second U vacancy moves into the immediate vicinity of the defect. The second U vacancy forms a charged tetra-vacancy cluster with the tri-vacancy and the Xe atom moves to the center of this configuration (b). The Xe atom will settle near one of the U vacancies releasing the other U vacancy to diffuse again at random (c). In Fig. 4.2 the fission product has settled near the new U vacancy, and the original U vacancy has moved off (d). The oxygen vacancies in the tri-vacancy may rearrange the tri-vacancy through interactions with other O vacancies, but they will not directly contribute to the bulk motion of the Xe atom [45].
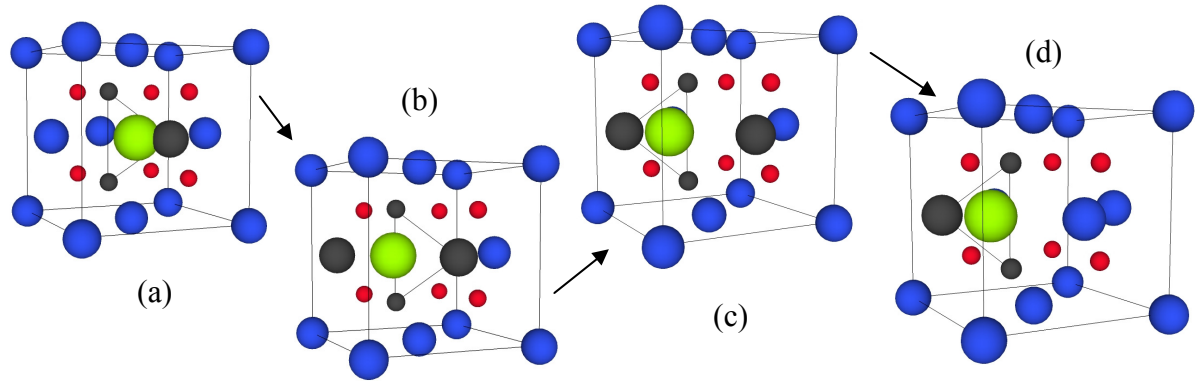
Fig. 4.2. The process of Xe diffusion in UO_2 by the mechanism described above. In the figure blue spheres are Uranium, red spheres are Oxygen, the green sphere is Xe, and grey spheres represent vacancies

The suggested mechanism is also supported by experimental studies where the migration energy of Xe is shown to be similar to that of U vacancy self-diffusion. The assertion that the noble gas migration must proceed via a vacancy cluster was also tested in experiment. Samples of UO_2 were doped with Niobium, which is a (+5) valence state atom, in order to create additional Uranium vacancies. The doped UO_2 did not show an enhancement in the diffusion of Xe providing evidence that Xe does not migrate via single U vacancies [49].

4.2 *Extension of Molecular Dynamics to Diffusion*

4.2.1 Self-Diffusion in the Bulk Crystal by MD

The migration of oxygen in UO_2 has been studied because of the important effects that non-stoichiometric compositions of UO_2 have on the fuel. Oxygen tracer experiments show two important oxygen self-diffusion modes. In near stoichiometric to hyperstoichiometric conditions Oxygen was found to diffuse by hopping from interstitial site to interstitial site with a migration energy near 2.46 [61] or 2.57 eV [63]. Conversely, oxygen self-diffusion experiments with hypostoichiometric UO_2 show evidence of a vacancy assisted diffusion

mechanism that has a migration energy near 0.51 eV [64]. The vacancy mechanism is also supported by Mott-Littleton calculations that also find 0.51 eV for the migration energy [65].

For the purposes of Kr and Xe diffusion, the behavior of Oxygen self-diffusion in UO_2 provides a useful additional diffusion based benchmark for both MD and KMC simulations. Simulations for Oxygen self-diffusion were performed using DL_Poly 2.20 with the optimized UO_2 potential discussed in Section 3.2.2. The MD system contained 10x10x10 unit cells of UO_2 resulting in the simulation of 8000 O atoms and 4000 U atoms. The large system size was necessary to allow for the insertion of several pre-existing defects without overly perturbing the stoichiometry of the system. Simulations were run for temperatures ranging from 300 to 2700 K with simulation times of 250 or 500 ps and time steps typically of 1 fs. The trajectory of the simulations was usually output every 1 ps. From the trajectory it is possible to calculate the diffusion coefficient of the U and O atoms in the system along with other related functions such as the self and distinct van Hove self correlation functions that help clarify the underlying processes responsible for migration in the system.

Diffusion coefficients are calculated from the mean square displacement of the atoms as discussed in Section 4.1.2 Equation (4.6). In Fig. 4.3, the self diffusion of O in stoichiometric undamaged UO_2 is plotted versus the inverse of temperature in the typical Arrhenius fashion. In the MD simulations O self-diffusion was observed from temperatures of 1850K to 2400K. The MD simulations are compared to the Oxygen self-diffusion experimental fits derived from experiments by Belle [62] and experiments by Marin and Contamin [63]. The simulated diffusion was observed at higher temperature ranges than in the experiments. At lower temperatures, the MD simulations did not exhibit a mean square

displacement that changed with simulation time, so it was not possible to calculate the diffusion coefficient. However the results of simulation were near the same temperature range explored by Belle, but not quite the Marin and Contamin temperature range. The migration energy found from the MD simulations was 2.33 eV which is quite comparable to the 2.46 and 2.57 eV migration energies found by the experiments. The temperature independent response of the simulated diffusion coefficients (i.e. the D_0 term in Equation (4.22)) is also very close to the Marin and Contamin results.
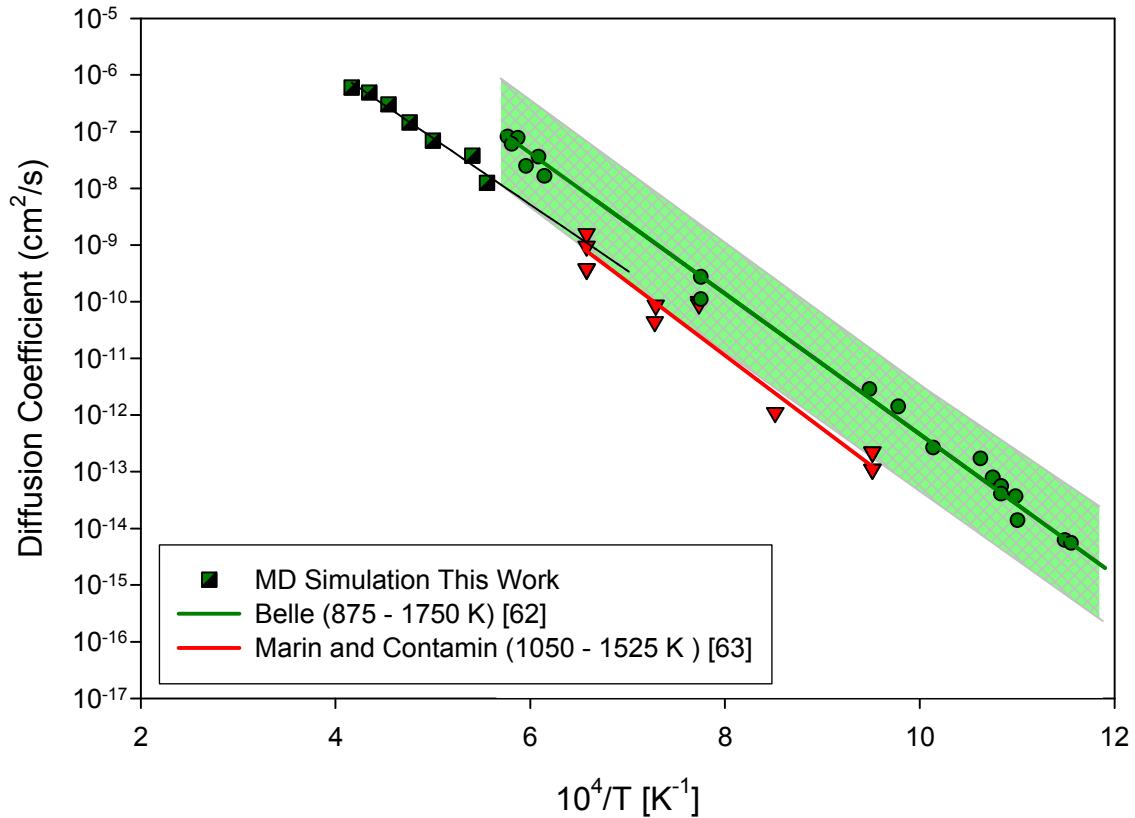
Fig. 4.3. Self Diffusion of O from MD with perfect crystal UO_2 compared to two experiments

The fit provided by Belle is derived from 3 sets of experiments performed on near stoichiometric UO_2 of different physical forms and was given a 95% tolerance interval that is

also shown in Fig. 4.3. The samples used in the Marin and Contamin study were mostly sintered powders and a few single crystal samples. They reported no major differences in the self-diffusion behavior between the two physical forms due to a grain boundary effect. The similar migration energies measured between the experiments and the simulation show that the comparison of the three sets of data is appropriate and the diffusion behavior in the experiments was not being significantly altered by a non-bulk diffusion process.

In Fig. 4.4, the diffusion coefficient as a function of inverse temperature is plotted for UO_2 with preexisting O defects. The diffusion coefficients were derived from the mean square displacement of O atoms using Equation (4.6) in Section 4.1.2. The concentration of O vacancies in the simulation was 0.00125 which is equivalent to a formulation of $UO_{2-0.0025}$ for the simulated crystal. The MD simulations are split into 2 different temperature regimes that show different behavior. For temperatures ranging from 900 to 1800 K the diffusion coefficients follow the standard Arrhenius relationship for diffusion coefficient and the inverse of temperature. This temperature range is representative of the expected TRISO fuel operating temperature range. The fuel temperature data was found to have a migration energy of 0.578 eV which is similar to the experimentally measured migration energy of 0.51 eV [64]. The experiments performed by Kim and Olander [64] were carried out by annealing two samples of hypostoichiometric UO_2 one of which was enriched in radioactive O-18. Hypostoichiometric UO_2 contains intrinsic O vacancies very similar to the MD simulations of UO_2 with pre-existing defects. The MD results also compare favorably with results from Ref. [66] that found a migration energy of 0.58 eV for Oxygen self-diffusion in UO_2 with pre-existing defects of a similar concentration ($UO_{1.91}$).
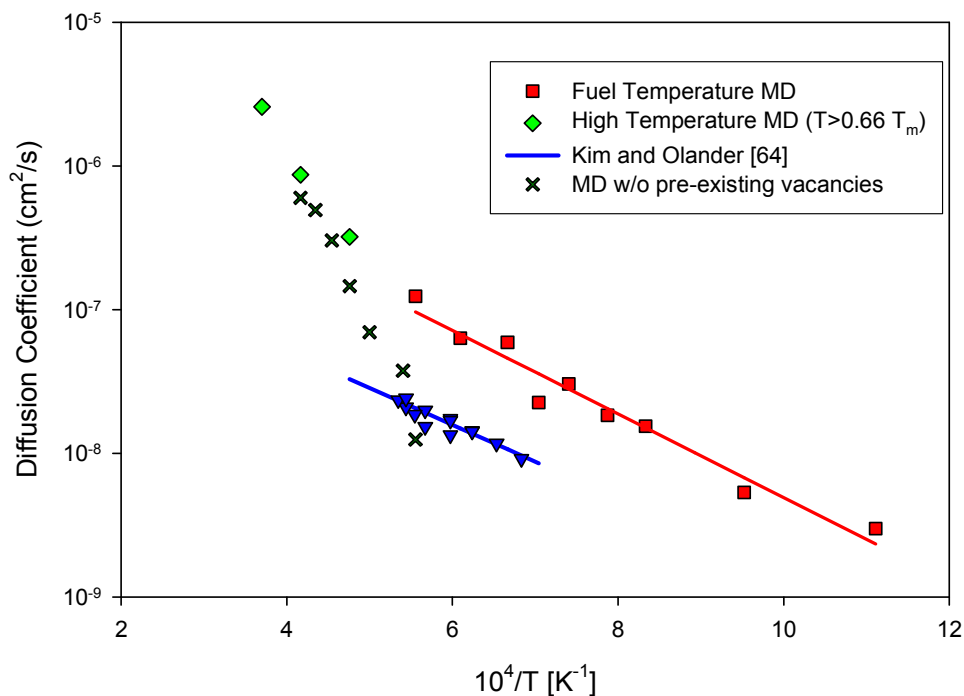
Fig. 4.4. Oxygen Self-Diffusion coefficients for MD systems containing preexisting defects compared to fit of experimental data from $UO_{2-0.0025}$

At higher temperatures ranging from 2100 to 2700K, the diffusion coefficients begin to become larger than is expected from a simple Arrhenius relationship in Fig. 4.4. Notice how well this data corresponds to the data from the MD simulations with no pre-existing vacancies (shown in dark green). This is evidence of a transition from a temperature regime where migration energy and non-thermal vacancies dominate diffusion to a temperature region where the vacancy formation energy and thermal vacancies dominate the diffusion coefficient as seen in Fig. 4.1.

The diffusion coefficient measures the amount of migration occurring in a system, but it does not elucidate the mechanism of migration that is occurring. By examining the self part of the van Hove correlation function, it is possible to explore some of the mechanisms of migration present in the diffusion behavior of UO_2. This correlation function is the

probability that an atom will be some distance r away from its original starting position at some time t. Insight into the diffusion process can be derived through observing which neighboring positions are filled by atoms leaving their initial positions. The time evolution of the self part of the van Hove correlation function is shown for perfect crystal UO_2 at 2100 K in Fig. 4.5 and shown for UO_2 with pre-existing vacancies in Fig. 4.6. From the figures, it appears that the majority of atoms will vibrate around their original position as indicated by the large initial peak in Fig. 4.5 and Fig. 4.6. However as time progresses many atoms will hop to the nearest neighbor position indicated by the small peak at 2.734 Å. This peak provides evidence that the O atoms in UO_2 with pre-existing defects are migrating by vacancy assisted diffusion on the simple cubic O sub-lattice of UO_2. Closer examination of the of Fig. 4.5 and Fig. 4.6 indicate peaks forming at the 3rd nearest neighbor sites of r equal to 3.87 Å and subsequent neighbor sites. Increases in temperature accelerate the migration of the atoms to new nearest neighbor positions as seen in Fig. 4.7 for perfect crystalline UO_2 and in Fig. 4.8 for UO_2 with pre-existing vacancies. These plots show the relative effect of temperature on diffusion for the two systems at a single point in simulation time. As the temperature is increased the atoms become increasingly mobile making it less and less likely that they will be near their origin location. Additionally the 2700K data in Fig. 4.8 demonstrates how as the temperature increases the van Hove correlation function can help indicate when the crystal structure begins to break down. For a fluid this function would be flat line, clearly the O atoms at 2700K are beginning to become more fluid like which is expected from a simulation that occurs at approximately 85% of the melting temperature of UO_2.
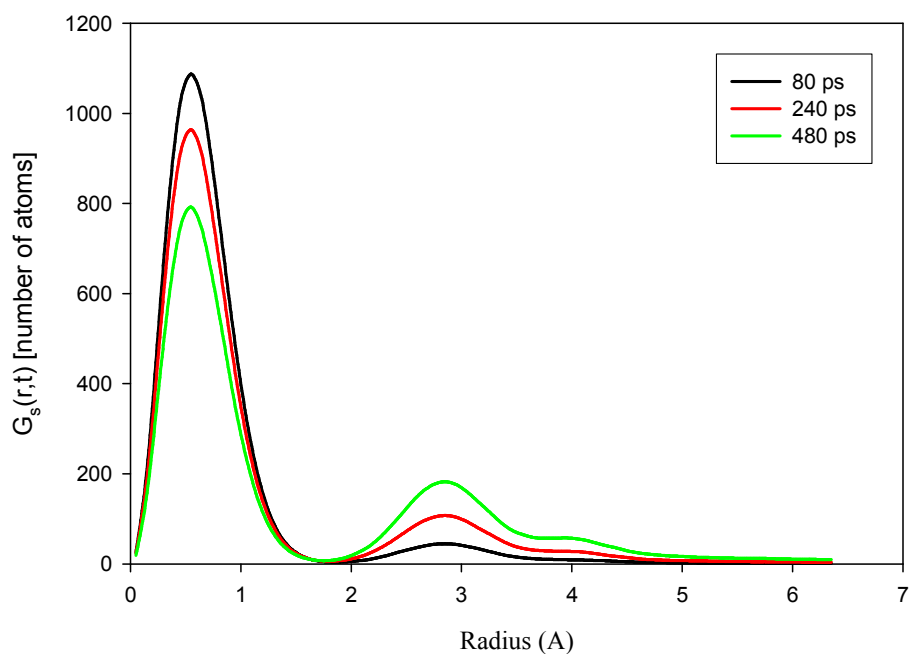
Fig. 4.5. The self part of Van Hove correlation function for O in perfect crystal UO_2 at 2100 K at different simulation times
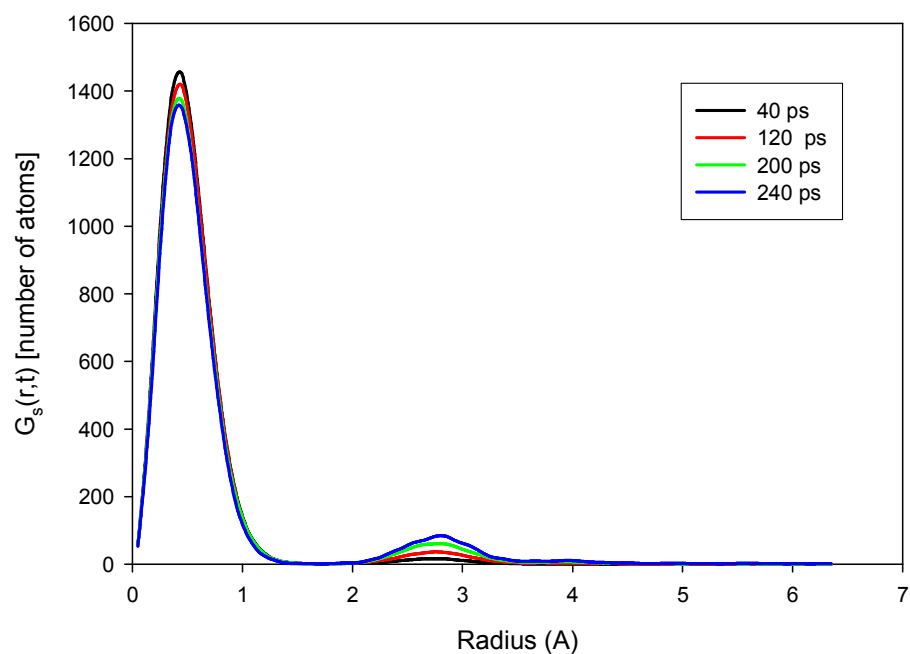
Fig. 4.6. Self part of Van Hove correlation for O atoms in UO_2 with pre-existing defects at 1500K at different simulation times

73
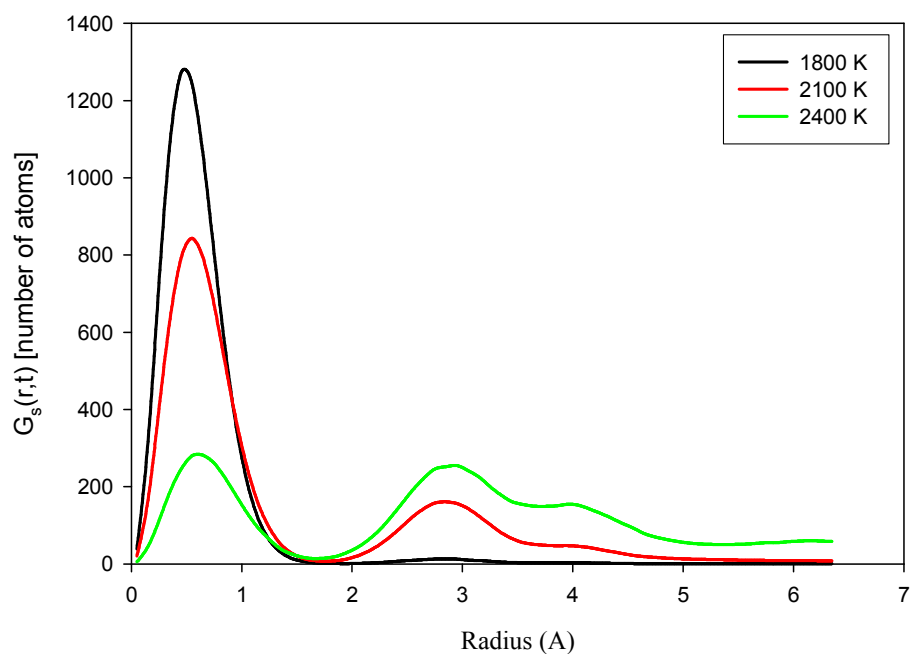
Fig. 4.7. The self part of Van Hove correlation function for O in perfect crystal UO_2 after 400 ps of simulation time for different temperatures
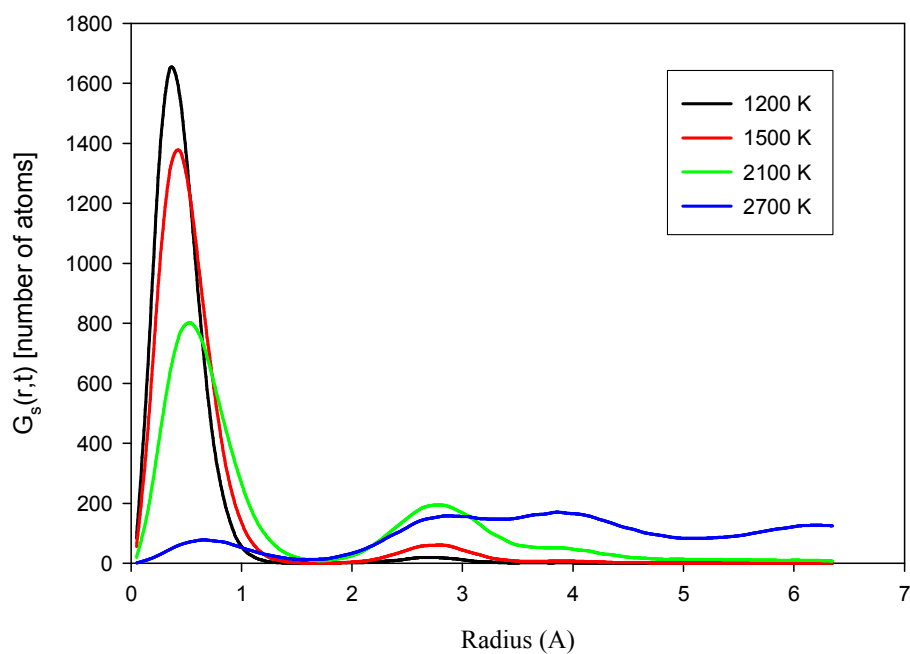
Fig. 4.8. The self part of the Van Hove correlation for Oxygen atoms in UO_2 with pre-existing defects at different temperatures after 200 ps of simulation time

Ideally Uranium self-diffusion would also be simulated by Molecular dynamics. However experimental data indicates that the barrier to U self-diffusion is quite high. In Matzke's review article [67] the suggested value is 5.6 eV. More recent experimental results using secondary ion mass spectrometry from Sabioni et al [68] give a migration energy of 4.4 eV. In this work and others [38], MD simulations were not able to simulate the self-diffusion of U atoms in UO_2 on the time scales available. Even when pre-existing defects were incorporated to the system no U self-diffusion was observed. The inability to simulate this in MD is an important motivation for the creation of KMC simulations that can observe this phenomenon and will be discussed in the subsequent chapter. Since U vacancy diffusion is thought to be key to noble gas diffusion discussed in Section 4.1.6, it was important to estimate the barrier height between a U atom and an adjacent vacancy with MD. The value of the barrier height can be compared to experiment and used as an input for KMC simulations. In DL_POLY an 8x8x8 unit cell system of UO_2 was created with a single U vacancy. A second system was created with an adjacent U atom moved to the saddle point between its original position and the lattice position of the vacancy and frozen in place. The equilibrium energy of the single vacancy system was compared to the equilibrium energy of the frozen atom system to estimate the barrier height. The results were a barrier height of 4.8 eV for U vacancy assisted diffusion, which compares favorably with the values from references [67] and [68].

4.2.2 Impact of Changes in Crystal Microstructure Conditions on Diffusion

The net process that is observed as diffusion is not solely influenced by behavior of atoms in the bulk of undisturbed crystals. Diffusion contains frequency information that can be impacted by structure including the interfaces between different crystals and radiation damage from fission and fast neutrons. Both the conditions in the grain boundaries and the effect of radiation damage will tend to enhance the diffusion coefficient of atoms under these conditions.

Interfaces form solids where two crystal grains meet whose structures have different orientations. There are many such interfaces in polycrystalline materials like ceramic UO_2. In the grain boundary region of a crystal the atomic structure is less densely packed. The mis-orientation of the crystal grains also influences the cohesive energy in the grain boundaries. The general state, of atoms being less bound in the grain boundary than in the bulk, creates a high diffusivity pathway through the material [47]. The high diffusivity effect of grain boundaries was first observed in the 1930s, and by the 1950s the enhancement in diffusion by grain boundaries was confirmed by experimental observation. Grain boundary diffusion plays a key role in polycrystalline materials below 0.6 T_m, and is different enough from bulk diffusion that the two kinds of diffusion are considered to take place in separate diffusion regimes. The diffusion spectrum is marked by different levels of atomic constraints where diffusion is further enhanced as more and more constraints are lifted. Bulk diffusion (D_{bulk}) is the most constrained followed by dislocation core diffusion (D_d), grain boundary diffusion (D_{gb}) and then surface diffusion (D_s) as illustrated by Equation (4.27) [69].

$$D_{bulk} << D_d < D_{gb} < D_s \tag{4.27}$$

Similarly the energy required for diffusion to proceed shrinks as atomic constraints on motion are lifted between bulk, grain boundary, and surface diffusion as illustrated in Equation (4.28).

$$E_{D,bulk} > E_{D,d} > E_{D,gb} > E_{D,s} \tag{4.28}$$

Grain boundary diffusion has been shown empirically to still follow and Arrhenius relationship shown in Equation (4.22). In metals the bulk diffusion coefficient is usually 4 to 6 orders of magnitude lower than the grain boundary diffusion coefficient, but in empirical studies of metals the pre-exponential factor does not significantly change, leaving most of the change in diffusion coefficient to the energy of diffusion term (E_D) [69].

When observing diffusion for a polycrystalline material, the observed diffusion coefficient will be some effective combination of grain boundary and bulk diffusion. The effective diffusion coefficient (D_{eff}) for both self-diffusion and diffusion by a foreign atom has been defined by the Hart model [69]. In the case of self-diffusion the Hart model for effective diffusion is given by Equation (4.29).

$$D_{eff}^{self} = gD_{gb} + (1-g)D_{bulk} \tag{4.29}$$

The term g is the fraction of atomic sites in the grain boundary of the polycrystalline material. It can be estimated by the following equation.

$$g = \frac{q\delta}{d} \tag{4.30}$$

The term q is determined by grain shape. It is 1 for planar grain boundaries and 3 for cubic grains. The grain boundary width is given by δ, and d is the diameter of grains in the system. In general the grain boundary region (δ) is considered to extend 5 to 10 Å into the crystal. The diameter of UO_2 crystals in TRISO fuel is typically 10 − 20 μm [50]. For

foreign or impurity atoms diffusing in the crystal the effective diffusion coefficient ($D_{eff}{}^{imp}$) is slightly different.

$$D_{eff}^{imp} = \tau D_{gb} + (1 - \tau) D_{bulk}$$ (4.31)

Where τ is the fraction of time impurity atoms spend in the grain boundary, and this value can be estimated from the following equations.

$$\tau = \frac{gc_{gb}}{gc_{gb}(1-g)c} \approx \frac{sg}{1+sg} = \frac{qs\delta/d}{1 + qs\delta/d}$$ (4.32)

$$s = \frac{c_{gb}}{c}$$ (4.33)

The term c_{gb} is the impurity concentration in the grain boundary, c is the impurity concentration in the bulk, and s is the segregation coefficient. If the concentration of impurity atoms is in equilibrium between the bulk and the grain boundary region, the effective diffusion coefficient will reduce to the form seen in Equation (4.34) [69].

$$D_{eff}^{imp} = \frac{g}{1+g} D_{gb} + \left(1 - \frac{g}{1+g}\right) D_{bulk}$$ (4.34)

From Equation (4.28), the migration energy of the diffusion of atoms in the grain boundary region will be lower. A good general estimate of the change in migration energy is on the order of a factor of two ($2E_{m,GB} \sim E_{m,bulk}$). The difference in migration energy leads to grain boundary diffusion dominating vacancy assisted diffusion at lower temperatures and bulk diffusion dominating at higher temperatures. Additionally the size of the crystal grains in a material will influence the temperature at which grain boundary diffusion dominates versus where bulk diffusion dominates. The Arrhenius behavior of these properties is illustrated in Fig. 4.9. From the figure the low temperature (right side of graph) behavior of

the observed diffusion coefficient is dominated by the lower migration energy (i.e. lower slope) grain boundary behavior [47].

The grain size behavior seen in Fig. 4.9 can be explained by a surface area to volume argument. As the grain size decreases the number of atoms on the grain boundary will increase compared to the number of atoms in the bulk of the material leading to the domination of the grain boundary diffusion at higher temperatures. Similarly the *g* term in Equation (4.29) and Equation (4.34) will increase as grain size decreases causing the effective diffusion coefficient to become closer to the grain boundary diffusion coefficient. More detailed analysis and background on grain boundary diffusion can be found in the books by Mehrer [69] and Kaur et al [70].

Radiation damage brought about by the fission process and interactions with fast neutrons will also have an effect on the behavior of diffusion in polycrystalline materials. Frenkel pair defects, Schottky defects and vacancies will occur due to radiation damage especially in nuclear fuel materials. These defects enhance diffusion in two important ways. Any vacancy created by radiation damage will add to the vacancy concentration term found in Equation (4.21) part 2 modifying the diffusion coefficient as shown below where C_{irr} is the concentration of vacancies due to irradiation as shown in Equation (4.35). The modification to vacancy assisted diffusion by radiation damage is analogous to the effect of non-thermal vacancies discussed near the end of Section 4.1.2.

$$D_a^v = a_0^2 \nu_0 e^{\left(\frac{S_m}{k}\right)} p_v e^{-\frac{E_m}{kT}} = \underbrace{a_0^2 \nu_0 e^{\left(\frac{S_{m,v}}{k}\right)}}_{1} \underbrace{\left(e^{-\frac{E_{f,v}}{kT}} + C_{irr} \right)}_{2} \underbrace{e^{-\frac{E_{m,v}}{kT}}}_{3} \tag{4.35}$$

$$C_{irr} \propto \Phi t_{irr} \tag{4.36}$$

As shown in Equation (4.36), the concentration or radiation damage vacancies is a function of the neutron flux and irradiation time along with several other factors such as neutron cross section and fission rate, but not temperature. Vacancies created by radiation damage create a non-thermal component to the diffusion coefficient of vacancy assisted mechanisms, and will dominate the diffusion at low temperatures where the concentration of thermal vacancies is low much like in the case of grain boundaries. The effect increasing radiation damage on the diffusion coefficient is also analogous to decreasing grain size as illustrated in Fig. 4.9.
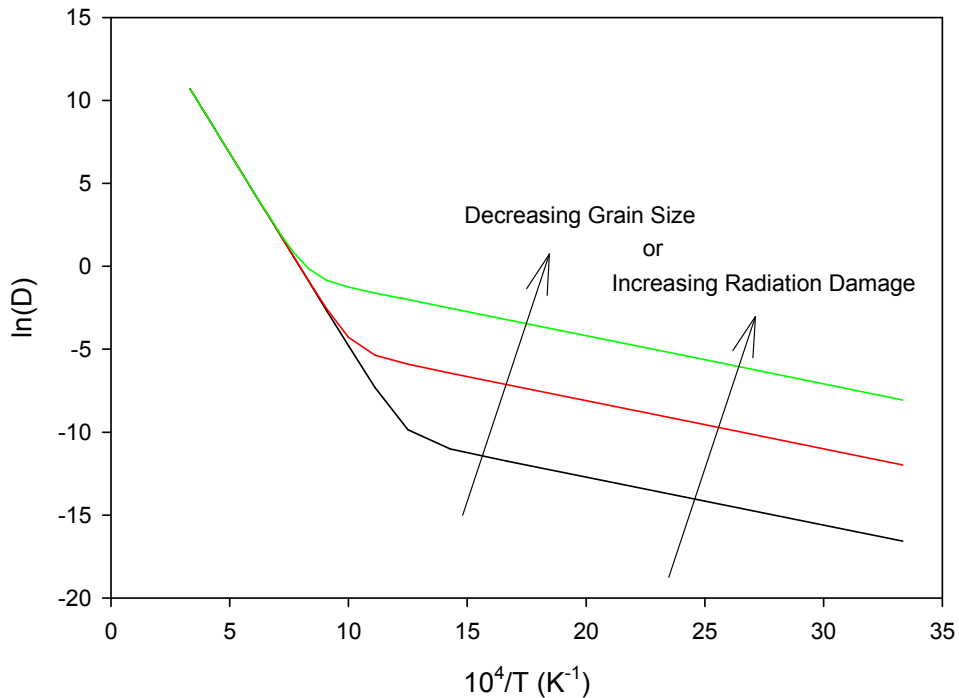
Fig. 4.9. Influence of Grain Size and Radiation Damage on Diffusion

A second manner in which radiation damage enhances diffusion is the creation of new diffusion pathways that do not exist in perfect crystal systems. The creation of new pathways is especially important in the diffusion of noble gas atoms in nuclear fuel. The majority

radiation defect in UO_2 is Frenkel pairs, but Schottky defects consisting of one Uranium and 2 Oxygen vacancies will form in the fuel. The fission process also encourages Schottky or neutral tri-vacancy production by destroying U atoms thereby creating U vacancies that can form vacancy complexes with free O vacancies. The formation of vacancy complexes creates trap sites and diffusion pathways for species that are insoluble in the UO_2 crystal and cannot diffuse via the interstitial pathway.

Radiation damage is needed to form these pathways. Even though there is a finite probability that vacancy complexes could form thermally however the probability is very low. For example consider the case of thermal Oxygen vacancy formation versus Oxygen di-vacancy formation at 1500 K and assuming 5 eV for $E_{f,O}$ and 10 eV for $E_{f,\,2O}$. The thermal vacancy concentration is $\sim10^{-17}$ while the thermal di-vacancy concentration is $\sim10^{-34}$, which is about 1 di-vacancy in 20 metric tons of UO_2. Clearly, vacancy clusters seldom form thermally even under reactor temperatures.

4.2.3 Modification to Self-Diffusion by Grain Boundaries in the Simulation

The modification of diffusion by grain boundaries is a well known phenomenon and was discussed in Section 4.2.2. Grain boundaries (GB) provide a high diffusion region in crystals where the barrier to movement is lower than in the crystal interior. This results from atoms being more loosely packed due to crystal misalignments at the crystal-crystal interface.

To simulate a grain boundary interface in Molecular Dynamics, two large crystal super-cells are constructed, where one super-cell is rotated by some angle relative to the other super-cell. For this simulation, the rotation angle was chosen to correspond to a symmetrical

tilt grain boundary. Specifically a <310> Σ5 grain boundary was created that corresponds to a misalignment angle of 36.87°. An example of this configuration being used in a DL_POLY simulation is shown in Fig. 4.10. The lower grain remained stationary, and the upper grain was rotated about the *y* axis by the mis-orientation angle to produce the grain boundary.

The effect of grain boundaries on self-diffusion properties derived from MD simulations was studied using the Σ5 grain boundary atomic configuration under different conditions. To account for the lattice expansion at different temperatures the crystal was allowed to reach an equilibrium state in the NVT ensemble where the lattice coefficient was set at the expected experimental lattice coefficient given by either Equation (3.13) or (3.14) depending on temperature. Simulations were run for reactor relevant temperatures ranging from 300 K to 2100 K for approximately 500 ps.
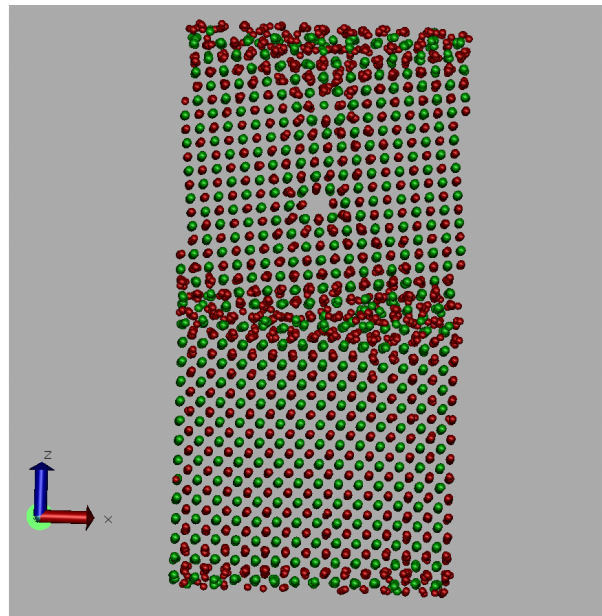
Fig. 4.10. Sigma 5 grain boundary in a UO$_2$ MD simulation

The grain boundary core region is usually considered to extent approximately 5-10 Å from the plain of the grain boundary interface. The trajectories U and O atoms in the region

extending 6 Å above and below the interface plain were used to calculate diffusion coefficients. These results were compared to MD results of self-diffusion of O atoms in the bulk crystal. An Arrhenius plot of this data is shown in Fig. 4.11.

There are several key details to take away from Fig. 4.11. First, U self-diffusion is observable at the grain boundary interface. In bulk crystal simulations with and without pre-existing defects, the barrier to diffusion is too high to observe U self-diffusion. Additionally the migration energy of the U atoms on the GB is very low ($\approx$0.2 eV) almost athermal in behavior when compared to the MD predicted barrier energy of 4.8 eV or experimental 4.4 eV barrier height. However this behavior is consistent with theory presented is Section 4.2.2 concerning the effect of GB on diffusion.
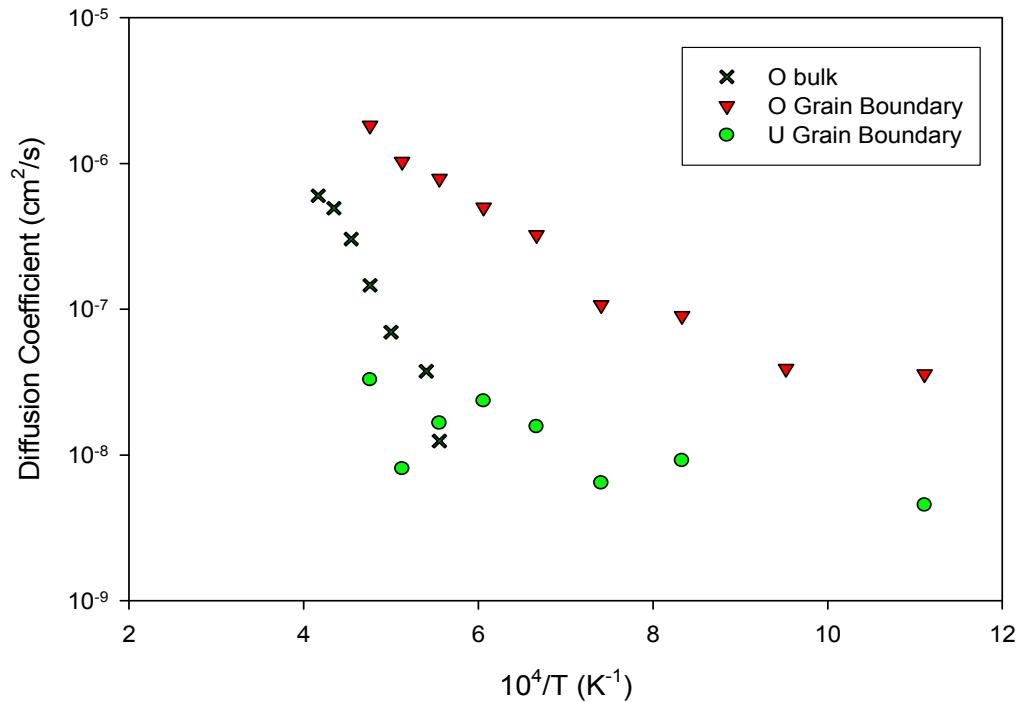
Fig. 4.11. Arrhenius Plot of O and U self-diffusion in the Grain Boundary core region compared to the bulk crystal self-diffusion of O in UO_2

From these results it is not possible to definitively state a migration energy for the self-diffusion of U atoms at the grain boundary, but the mere evidence of diffusion is significant. From the incorporation energy data, it is clear that U migration must participate in the diffusion of trapped Kr and Xe in UO_2. Observing U diffusion at the grain boundary but not in the bulk implies that grain boundaries may play an important role in the diffusion and release of noble gas fission products. The O self-diffusion behavior for O atoms in the grain boundary is also significantly different from the bulk O diffusion. The less constrained atomic structure of the grain boundary results in diffusion coefficients that are much higher than bulk O diffusion coefficient. There are no pre-existing O vacancies present in the grain boundary region, but the O atoms act almost as if there were non-thermal vacancies present. The effective migration energy of the grain boundary O atoms is 0.56 eV, which is around 4 times lower than the 2.33 eV migration energy of the bulk O self-diffusion and is close to the migration energy for pre-existing vacancies of 0.578 eV. The change in migration energy follows the general rule set forth is Section 4.2.2. Additionally, the diffusion pre-exponential factor for the bulk diffusion and the grain boundary diffusion are similar which matches empirical observations discussed in Section 4.2.2 as well.

The self-diffusion behavior of atoms in the grain boundary region can also be examined using the self part of the van Hove correlation function. The correlation function for O atoms in the grain boundary at 1500 K is shown in Fig. 4.12, and Fig. 4.13 contains the function for U atoms in the grain boundary region at 2100 K. The data in Fig. 4.12 can be compared to the data in Fig. 4.5 and Fig. 4.6 to see how grain boundaries distort the structure of the crystal. Notice how much more structure exists in the grain boundary figure. Clearly the

atoms in the grain boundary region are migrating much faster than the bulk O atoms and are much more likely to occupy a position in the crystal that is not its original position. In the grain boundary region data for Fig. 4.13, Uranium atoms also exhibit a probability for occupying their nearest neighbor positions that is not seen in bulk diffusion studies with Molecular Dynamics. It is also instructive to examine the directional behavior of the van Hove correlation function for the atoms in the grain boundary region. In Fig. 4.14 to Fig. 4.17 the correlation function is split into two parts. The first part seen in Fig. 4.14 for O atoms and Fig. 4.15 for U atoms examines the motion along the plane of the grain boundary and only considers displacements in two directions. This case allows you to see how migration is enhanced along the grain boundary plain. The second special case of the van Hove correlation function only considers displacement of the atoms in the direction perpendicular to the grain boundary plain. This case is shown in Fig. 4.16 for O atoms and Fig. 4.17 for U atoms and shows behavior that is more similar to the behavior seen in the bulk crystal simulations. Notice how while Fig. 4.16 has a first nearest neighbor peak it has none of the other distinct peaks present in Fig. 4.14. Some care must be taken when examining these plots. The first nearest neighbor peak shifts in the plots depicting U atom behavior, but this is due to U atoms moving in two dimensions when it makes a hop not necessarily a significant change in the crystal structure of the UO_2.
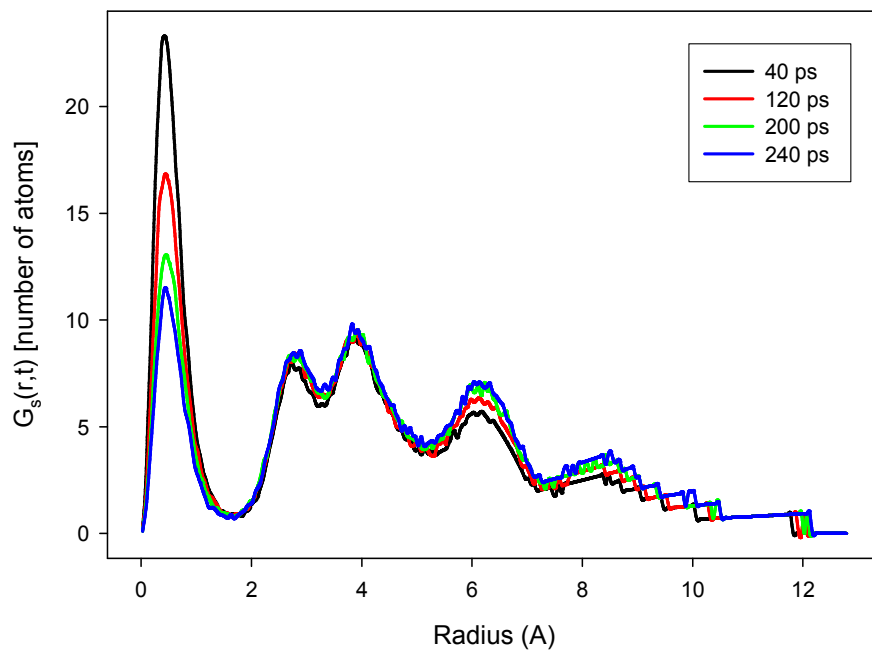
Fig. 4.12. The self part of the Van Hove correlation function for O atoms in the grain boundary region at 1500K
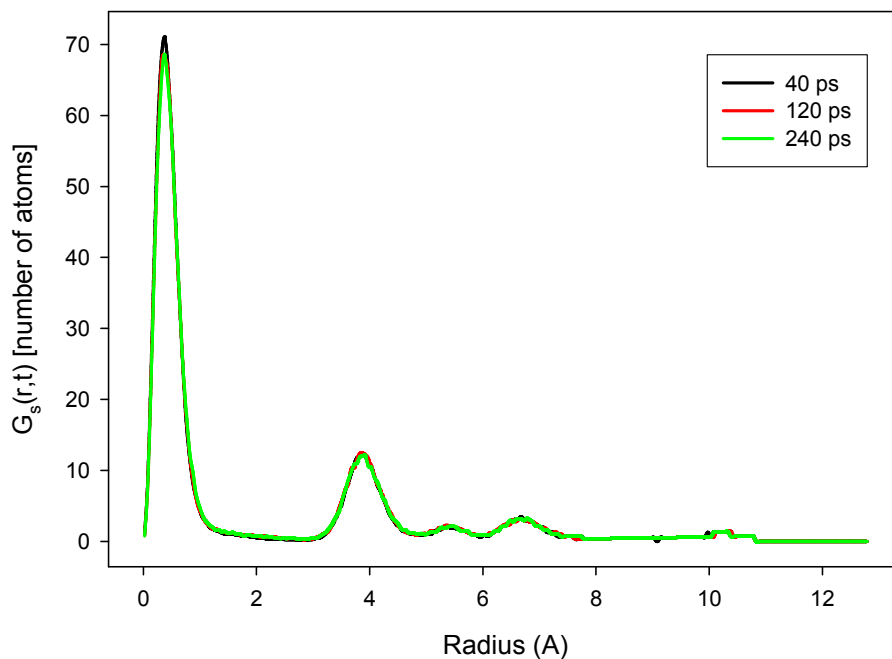
Fig. 4.13. The self part of the Van Hove correlation function for U atoms in the grain boundary region at 2100K
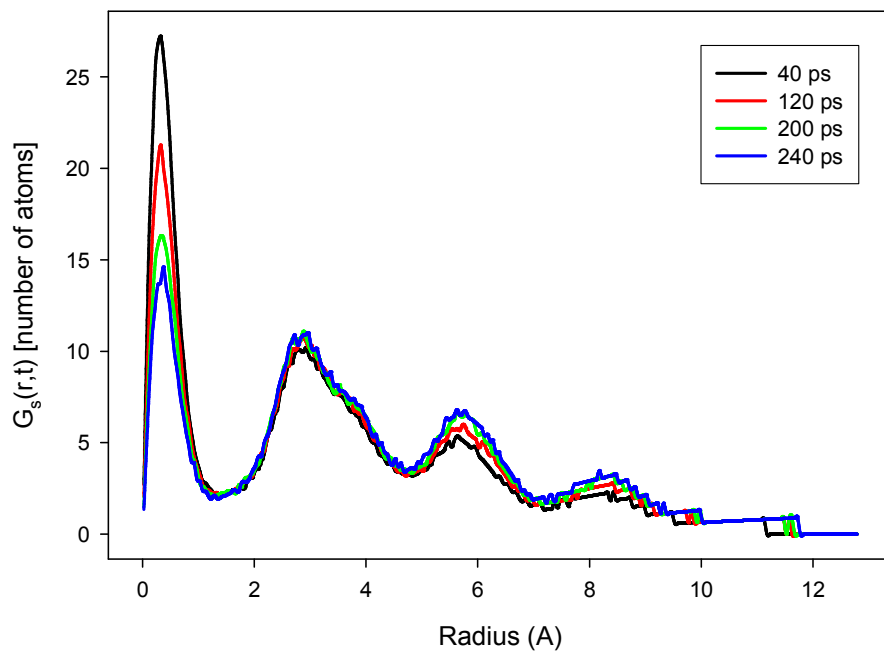
Fig. 4.14. The self part of the Van Hove correlation function restricted to the grain boundary plane for O atoms in the grain boundary region at 1500 K
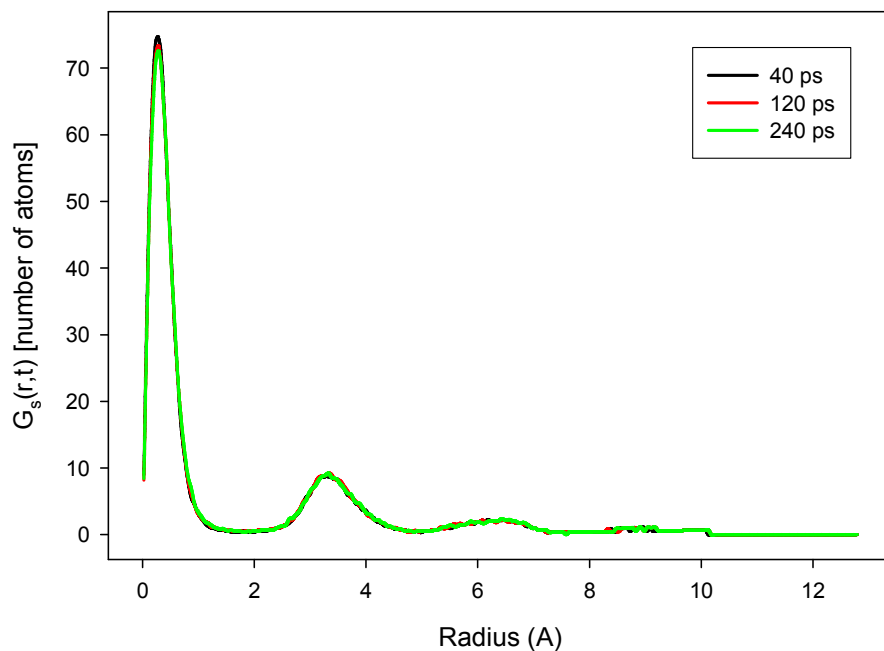
Fig. 4.15. The self part of the Van Hove correlation function restricted to the grain boundary plane for U atoms in the grain boundary region at 2100 K
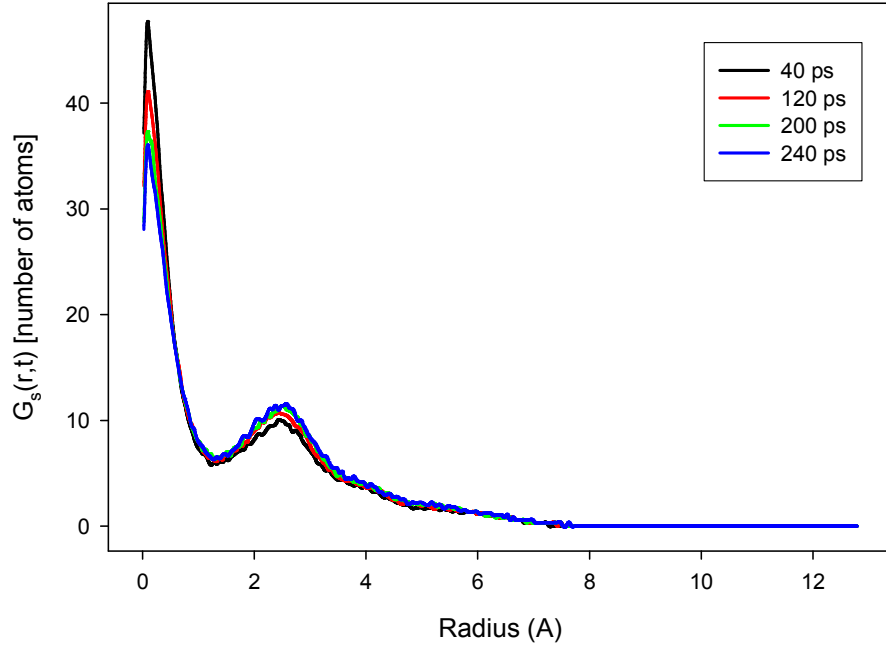
Fig. 4.16. The self part of the Van Hove correlation function restricted in the direction perpendicular to the grain boundary plane for O atoms in the grain boundary region at 1500 K
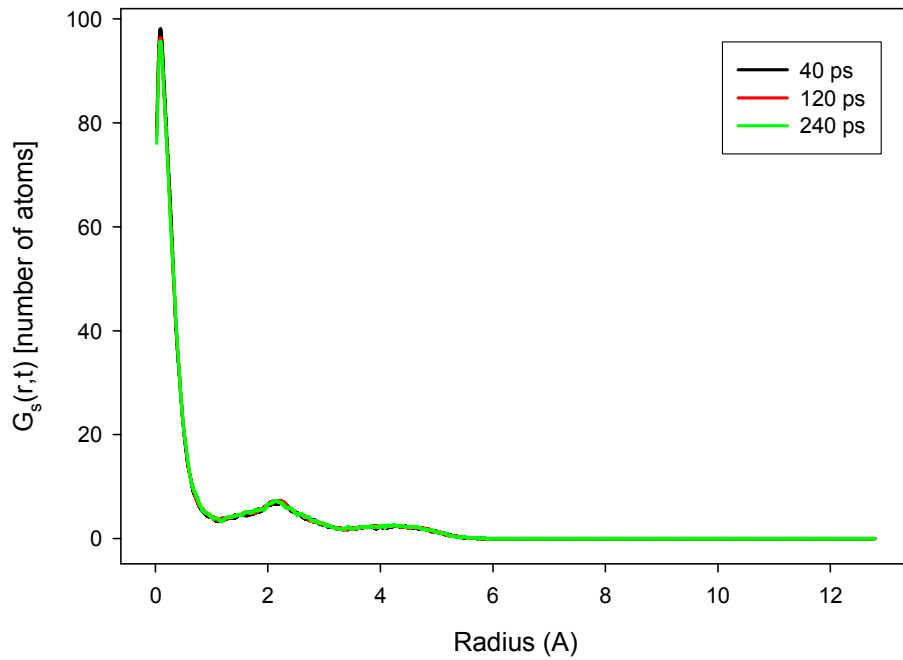
Fig. 4.17. The self part of the Van Hove correlation function restricted in the direction perpendicular to the grain boundary plane for U atoms in the grain boundary region at 2100 K

4.2.4 Radiation Damage Simulations

Radiation damage occurs through several mechanisms when UO_2 is used as a fuel in nuclear reactors. Cascades from fission fragments, primary knock-on atoms (PKA) from interactions with fast neutrons, and all their associated secondary and tertiary recoiling atoms create many types of defect structures in the fuel and result in many displaced atoms. Fortunately UO_2 is very robust under irradiation and will often quickly return to its original crystalline structure after the initial radiation damage cascade subsides. Additionally many defects that remain after the initial radiation damage will anneal out of the crystal after some time has passed at operating conditions.

In this work radiation damage simulations with Molecular Dynamics were explored to investigate the self-diffusion behavior of radiation damaged UO_2 and the types of defects that were created due to radiation damage. The type of radiation damage studied was limited to fast neutron interactions with U atoms that create U PKAs. When a neutron elastically scatters of a U atom it will impart only a small amount of its total energy to the U atom due to the large difference in the masses of the two particles. A 2 MeV neutron can impart at most about 33.3 keV to a U-238 atom at rest. However this is recoil energy is more than enough to move the U atom out of its lattice site and begin slowing down through charged particle collisions with other atoms in the surrounding crystal structure.

Several different sets of radiation damage cascades were investigated. The simulations were linked together to simulate the effect of cascade overlap on the crystal. Each radiation damage simulation was carried out in DL_POLY_2.20 on a 10x10x10 unit cell UO_2 system. The initial atomic configuration was allowed to equilibrate for 2.0 ps, and then a random U

atom was selected as the primary knock-on atom for a cascade. An initial random direction for the PKA was chosen and an initial energy for the PKA was chosen either from a uniform distribution of energies between 0.0 keV and some predetermined maximum energy or as some constant energy. The MD time step for each cascade was determined by the initial energy of the PKA so that the PKA would travel no more than 0.5 Å in a single step. The cascade step runs for 3 ps, and then the system is allowed to equilibrate again for 0.5 ps before the next cascade.

The trajectories of the radiation damage simulations were analyzed for many different types of defects. These defects included the number of displaced O and U atoms from their original lattice site, the number or O and U Frenkel pairs produced, the number of O vacancies, U vacancies, U-O di-vacancies, and U-O-O tri-vacancies produced. All of these different types of defects were observed in the simulations. This is important to note considering the presence of minority defects like the U-O-O tri-vacancy trap is key in the proposed migration mechanism for Kr and Xe through UO_2.

Table 4.6. Point Defects present at end of cascade for 5 overlapping cascades of various energies

Impact	Energy of PKA (keV)	Displaced Atoms		Frankel Pairs		Vacancy Types			
		O	U	O	U	O	U	UO	UO_2
1	6.60	27	2	1	2	1	1	0	0
2	1.23	205	7	1	2	5	2	2	0
3	0.75	441	9	35	3	41	3	1	0
4	1.06	822	11	38	4	54	4	2	0
5	0.10	1047	11	8	3	8	5	0	1

Table 4.6 contains a listing of the number of point defects and displaced atoms present at the end of each overlapping cascade. In these 5 cascades there is evidence of all the different point defects of interest. As more and more cascades are overlapped on a system the number

of displaced O atoms will begin to approach the total number of atoms in the system, but the number of U atoms displaced will remain low usually only about 1 or 2 atoms will be displaced in each cascade. Similarly there will be many O vacancies formed in the system and only a few U vacancies. However even with only a few cascades it is possible to begin seeing the emergence of higher order point defects like the UO di-vacancy and UO_2 tri-vacancies or Schottky defects. Other MD simulations of radiation damage in UO_2 have also observed the formation of di-vacancies, tri-vacancies and higher order point defect clusters [71]. The behavior of Frenkel pairs in Radiation Damage simulations has also been studied. As the number of cascade overlaps increases, the number of Frenkel pairs in a system will begin to reach an equilibrium [72]. This behavior was observed in overlapped cascades in this work and is shown in Fig. 4.18. The number of Frenkel pairs changes slightly after each cascade the beginning of which can be identified by the drop in the number of Frenkel Pairs. There are 13 cascades represented in Fig. 4.18. Both the O Frenkel pair population and the U Frenkel pair population quickly reach an equilibrium number after about 6 or 7 cascades.
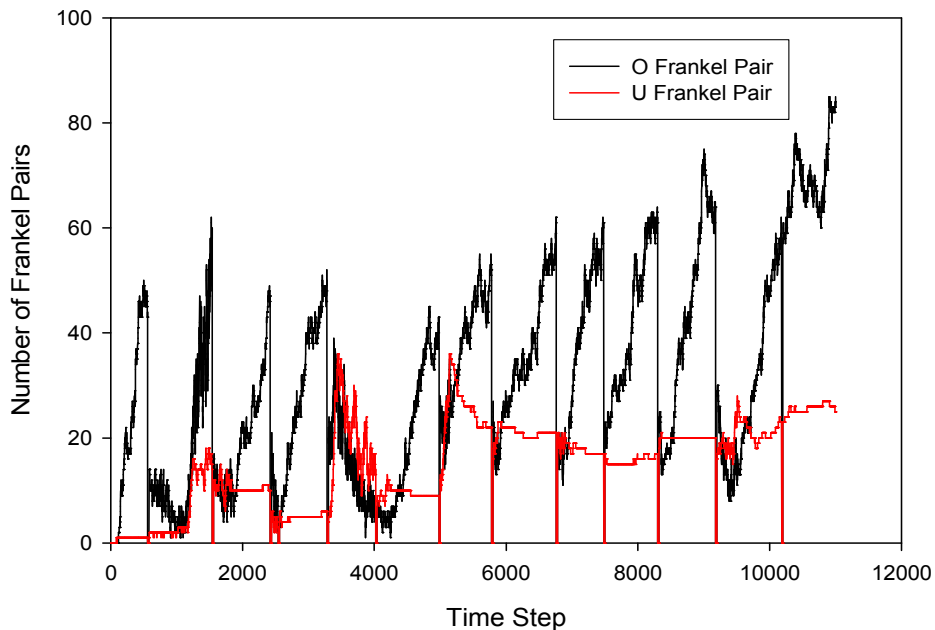
Fig. 4.18. Time behavior of Frenkel Pair population in radiation damage MD simulations

4.2.5 Modification to Self-Diffusion by Radiation Damage

Radiation damage will also affect the self-diffusion behavior or O and U atoms in the fuel as was discussed in Section 4.2.2 and illustrated by Fig. 4.9. In order to study the effect of radiation damage on self-diffusion, a UO_2 Radiation damage MD simulation was run for 11 overlapped cascades with a maximum PKA energy of 5 keV. The initial crystal contained 40 O Frenkel Pairs and 4 U Frenkel Pairs. The crystal configuration was then taken up to temperature in a MD simulation and run for an additional 250 ps. The mean square displacement of the O atoms for each temperature was converted to a diffusion coefficient using Equation (4.6) in Section 4.1.2 and compared to the O self-diffusion coefficients for MD simulations with and without pre-existing vacancies. The Arrhenius behavior of these simulations is shown in Fig. 4.19, and the self part of the time-space correlation function for the 1500K simulation is shown in Fig. 4.20.

92
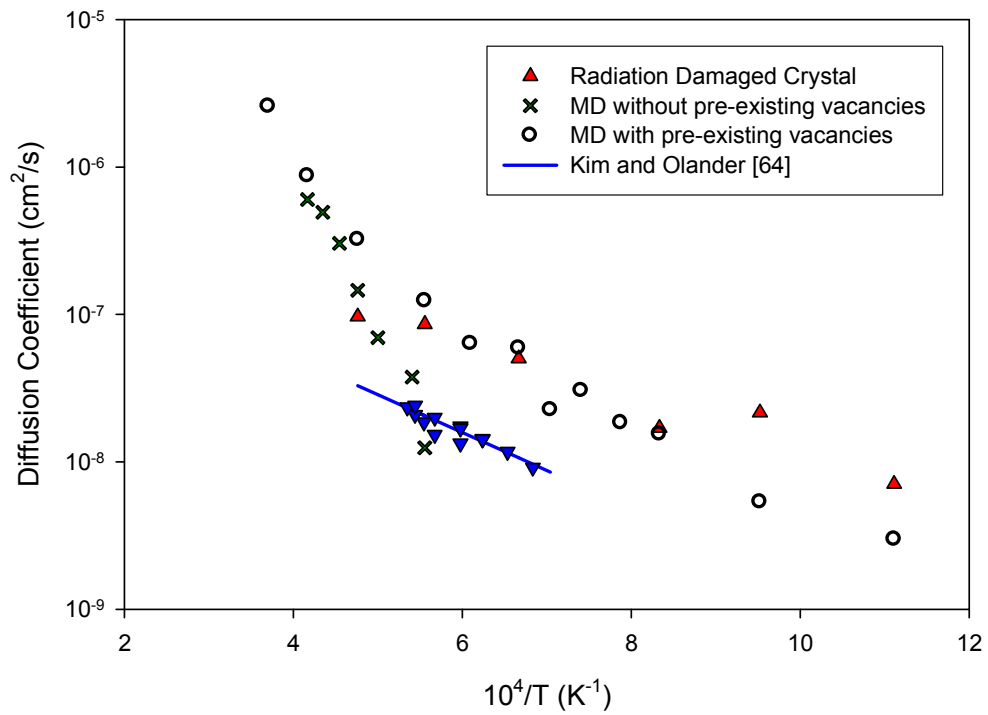
Fig. 4.19. Oxygen Self-Diffusion Arrhenius Behavior of Radiation Damaged UO_2 crystals compared to the behavior of crystals with and without pre-existing vacancies
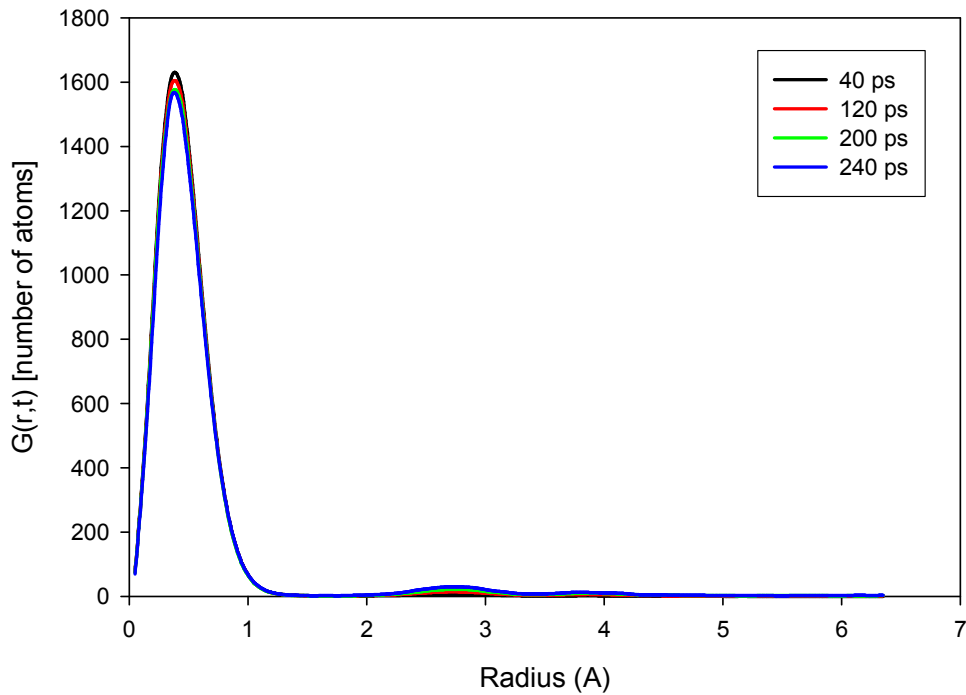
Fig. 4.20. Self part of the Van Hove correlation function for O at 1500K in Radiation Damaged UO_2

93

The O self-diffusion of the Radiation Damaged UO_2 is very similar to the self-diffusion of O in UO_2 with pre-existing vacancies. As expected from theory, the diffusion of the O is dominated by the presence of non-thermal vacancies that provide a diffusion pathway in the crystal. However there is an important difference in the O self-diffusion seen in the radiation damage case and the pre-existing vacancy case that can be seen by closely examining the differences between the self part of the Van Hove correlation plotted in Fig. 4.5 for pre-existing vacancies and Fig. 4.20 for radiation damage. Both of these plots examine the 1500 K simulation, but the first nearest neighbor peak in the pre-existing vacancy data at approximately 82 atoms for 240 ps into the simulation is much higher than in the radiation damage case at approximately 30 atoms for 240 ps into the simulation. This is most likely a result of Frenkel pair recombination. In the radiation damage simulations, O atoms are trapped in interstitials. If an O vacancy approaches a trapped O atom, the interstitial and vacancy will recombine destroying the low barrier diffusion pathway for the surrounding O atoms. Examination of the Frenkel pair population of the radiation damaged UO_2 MD simulations shows that as the simulations progressed there were fewer and fewer O Frenkel pairs present in the UO_2 crystal. This is a good example of where Arrhenius behavior is not enough to fully understand all phenomena taking place in a system.

Self-diffusion of U was also examined, as in the O Frenkel Pair case, the Frenkel pair population decreased as the simulation progressed. This lead to some completely non-thermal migration of U atoms in the system as the interstitials and vacancies of the U Frenkel pairs began to annihilate with one another. The evidence of this diffusion being non-thermal in nature is emphasized by the lack of any diffusion at these temperatures and higher

94

temperatures for UO$_2$ with pre-existing U vacancies. The destruction of Frenkel pairs by the U sub-lattice rearranging itself is also energetically favorable since Frenkel pairs increase the energy of a crystal system. No diffusion was observed below 1200 K. In the crystals simulated at 1200, 1500, 1800, and 2100K an average diffusion coefficient of 5.6 *10^{-9} was observed, and there was no thermal trend observed in the data.

4.2.6 Noble Gas Diffusion by MD

In Section 4.1.6, the theoretical and experimental migration mechanism for Kr and Xe diffusion in UO$_2$ was discussed. MD calculations of the incorporation energy for Kr and Xe in UO$_2$, shown in Section 4.1.5, support the neutral tri-vacancy or Schottky defect as the preferred trap site for Kr and Xe. All these factors support a U vacancy migration driven diffusion process for the noble gas fission products. Unfortunately as was demonstrated in Section 4.2.1 with pre-existing U defects, the current MD simulations cannot simulate the migration of U vacancies through the bulk crystal lattice. Therefore without U vacancy diffusion, the migration of Kr and Xe cannot be captured in the current MD model. However, the energetics of the probable diffusion mechanism can be explored in MD to use as inputs to a KMC program as was done at the end of Section 4.2.1 to find the saddle point energy for U vacancy migration. Some U self-diffusion was observed in grain boundary MD simulations of UO$_2$. It is likely that U migration in the grain boundary could play a significant role in Kr and Xe release from UO$_2$ in reactor fuel. However, the U diffusion observed in Fig. 4.11 is not definitive enough to draw many quantitative conclusions on the true behavior of U at the grain boundary. The limitations of the MD simulation suggest a multi-scale simulation technique is needed. In the next chapter, a Kinetic Monte Carlo

simulation of Kr and Xe diffusion through the bulk and grain boundary crystal lattice of UO_2 will be examined. The information learned from MD simulations of diffusion in the UO_2 system will be applied as inputs into the higher order Kinetic Monte Carlo atomistic technique. Most notably the O self diffusion data for pre-existing defects from MD is used to derive the inputs for O vacancy migration in the KMC algorithm, and the energy barrier derived for U from MD will be directly used as an input to the KMC simulation. The transfer of data that links KMC to MD is an important feature of a multi-scale approach for simulating the diffusion of Kr and Xe through UO_2.

Chapter 5 Kinetic Monte Carlo Calculations

A common theme in the investigation of self-diffusion using Molecular Dynamics was that while the behavior of O diffusion in the bulk crystal could readily be observed the behavior of U diffusion in the bulk crystal could not be observed by the time scales accessible in MD. In order to observe the U vacancy migration that is essential in the diffusion of Kr and Xe through bulk UO_2, a different atomistic technique was required. There are several atomistic techniques that address the time scales above Molecular Dynamics as seen in Fig. 3.1. For this work, the Kinetic Monte Carlo (KMC) technique was investigated and developed into a model of UO_2 that could simulate the diffusion of Kr and Xe through a UO_2 crystal.

5.1.1 Kinetic Monte Carlo Fundamentals

Many physical phenomena occur at the atomic level, but take place on time scales that are too long for simulation with Molecular Dynamics simulations which are typically limited to the hundreds of nanoseconds scale. For example the self-diffusion of Uranium in UO_2 is observable experimentally, but the barrier to diffusion is so high it is difficult to observe in MD simulations of realistic temperatures. The time scale for U self-diffusion is on the order of seconds, while the time scale for O self-diffusion is on the order of picoseconds. An alternative atomistic simulation technique called Kinetic Monte Carlo (KMC), however, can be utilized for observing the consequences of rare event atomistic phenomena.

Kinetic Monte Carlo models a system evolving dynamically from one state to another based on the probability of an event occurring [32]. A key underlying assumption in KMC is for the quantity that under observation. The vibrational movement of the atoms in the system, where they more or less remain in the same general vicinity, is less important than the infrequent larger atomic moves where atoms hop to another atomic position that is outside of its vibrational box (e.g. vacancy assisted diffusion). Another key to KMC is that the infrequent atomic moves occur sufficiently separated in time so that the atoms "forget" how they arrived in their current state. Additionally, the rate the atomic system changes must not depend on how it arrived. This way each move is random and independent creating a Markov chain of events that lead to a model of the dynamical development of the studied system.

The rate that atoms move by some path from state to state is called the rate constant in KMC simulations. The probability of any path in the system being chosen for the next step is defined by the size of the particular rate constant for that path versus the total rate constant for all possible paths. In simulations, the rate constants of N paths are numbered ($k_1, k_2, ... k_N$) and placed in a cumulative array where the value of each array is the sum of all previous rate constants, and the last cell in the array is the total rate constant (k_{tot}) as shown in Equation (5.1) and Equation (5.2).

$$k_{tot} = \sum_{i=1}^{N} k_i \qquad (5.1)$$

$$\text{Cumulative Rate Constant Catalog} = \begin{pmatrix} k_1 \\ k_1 + k_2 \\ \vdots \\ k_1 + k_2 + ... + k_{N-2} + k_{N-1} \\ k_{tot} \end{pmatrix} \tag{5.2}$$

A random number between 0 and 1 is then chosen and multiplied by the total rate constant. This value (k_{pick}) represents which path is chosen, however it cannot be used to directly identify which path is chosen. The value of k_{pick} will be between the values of two different consecutive entries in the cumulative rate constant array and will correspond to the event represented by the larger array entry. When this is implemented in a computational algorithm the array must be searched through to find the chosen event, the fastest and most popular array search method is the binary search algorithm.

Additionally, each move is also assigned a time that has passed before the move occurs. The probability that a system has jumped to the next state is defined as shown in Equation (5.3).

$$P_{jump}(t) = k_{tot} \exp(-k_{tot}t) \tag{5.3}$$

In the above equation, k_{tot} is the sum of all the individual pathway rate constants in the system. Given this probability it is possible to derive the random time step t_{step} of a KMC simulation from standard Monte Carlo techniques. First the probability distribution function is integrated to find the cumulative distribution function and set to a random number ξ uniformly distributed between 0 and 1. The equation is then rearranged to find the t_{step} for each KMC move.

$$\xi = \int_0^{t_{step}} k_{tot} \exp(-k_{tot}t')dt' = 1 - \exp(-k_{tot}t_{step}) \tag{5.4}$$

99

$$t_{step} = \left(\frac{-1}{k_{tot}}\right) \ln(\xi) \tag{5.5}$$

In Equation (5.5) the common practice of substituting ξ for $(1-\xi)$ is used. The value of ξ, should be supplied by a pseudo-random number generator with a large stride and period that avoids returning a 0.0 value.

Given a system of atoms for a simulation the rate constants for all moves in the system can be determined from transition state theory (TST). Consider a two state system with some energy barrier of height E_{sad} between two static initial and final positions of energies E_i and E_f, highly accurate rates can be calculated by determining the flux across a dividing surface set on the barrier between the states. However the details of these calculations are seldom necessary and a simpler approximation based on Harmonic transition state theory is usually used [32]. With this approximation the rate constant k^{HTST} is defined as

$$k^{HTST} = \frac{\prod_{i}^{3N} v_i^{min}}{\prod_{i}^{3N-1} v_i^{sad}} \exp\left(\frac{-E_{static}}{k_B T}\right). \tag{5.6}$$

Where the pre-factor consist of the normal mode frequencies of the atom at the minimum of the first static position v_i^{min}, and the normal mode frequencies of the atom at the saddle point v_i^{sad}. This form was originally derived from the work of Vineyard [33]. In Equation (5.6), E_{static} is equal to the difference in saddle point energy (E_{sad}) and energy state under investigation (E_i), k_B is Boltzmann's constant, and T is the temperature of the system. As a further simplification the pre-factor is usually reduced to a single frequency pre-factor (v_0), which is equal to the ratio of the products of the normal mode frequencies shown in Equation (5.6). Therefore all the physics in a KMC simulation is wrapped up in two factors the E_{static}

term that can be found from MD calculations or ab initio simulations, and the frequency pre-exponential factor (v_0). Typically, most effort in developing the values for KMC simulation is spent on the E_{static} term since small variations are amplified by its location in an exponential term. Less effort is usually spent on the pre-exponential frequency that can be estimated from a variety of sources including the Debye frequency and the phonon frequency dispersion. Data accumulated for many different materials has also found that for most materials v_0 will fall in the range $10^{12} - 10^{14}$ s^{-1}, and many studies simply choose to use 10^{13} s^{-1} as an adequate approximation [34].

For many systems the pathways that will develop are known before the simulation begins. Prior knowledge allows for the creation of rate constant catalogs that save the computational time of computing the rate constants at every KMC step. The catalog size is further reduced by assuming that only nearest neighbor atoms to a pathway represent possible jumps.

Issues with sampling all possible moves can arise in systems with multiple types of moves that have widely different barrier heights. The lowest barrier height will dominate the chosen pathway and can limit the simulation times accessible to the simulation. If the barrier heights are sufficiently different, a low barrier can prevent the high barrier move from ever occurring. For example a 1 eV barrier height at 1500K has an exponential term on the order of 10^{-4} while a 4 eV barrier height has an exponential term on the order of 10^{-14} at the same temperature. The chance of ever sampling the move corresponding to the 4 eV barrier is miniscule. One approximate solution for this problem of the low barrier is to artificially raise the low barrier. Since fast process moves will be in equilibrium the dynamical trajectory of

the whole system will still be dominated by the slower high barrier processes. Caution should be used whenever dealing with a low barrier problem to assure that the system dynamics are not distorted too badly by modifying the barriers [32].

5.1.2 Description of KMC Algorithm for UO$_2$

A custom KMC algorithm was created to specifically analyze the movement of U and O vacancies through a UO$_2$ crystal with special accommodations being made to simulate a tri-vacancy that is filled with either Kr or Xe and its particular migration pathway that is discussed in Section 4.1.6.

The input to any KMC code will include three key factors the geometry, the pre-exponential factor for the jump frequencies, and the Energy barrier of each different type of jump. Specifically in the algorithm for this work, the user specifies the size of super-cell desired, the number of U and O vacancies, the temperature of the system, the number of jumps to be simulated, the pre-exponential factor, several different migration energies for U and O vacancies that account for different vacancy configuration scenarios, and the location of the filled tri-vacancy if it is desired. There are also a few other inputs that deal with what kind of outputs to produce.

There are several types of vacancies and atoms in the KMC code. Their classification and position determines how they will interact with each other, and their probability for jumping from position to position. The crystal lattice is filled with O and U atoms that are tracked through the system. Free O and U vacancies move through the system based on a jump frequency (v) determined by Equation (5.7) which is a simplification of the rate constant shown in Equation (5.6)

$$\nu(T) = \nu_0 \exp\left(\frac{E_B}{kT}\right)$$
<div align="right">(5.7)</div>

Where ν_0 is the pre-exponential factor, and E_B is the energy barrier to a particular jump. Oxygen and Uranium vacancies that comprise the filled tri-vacancy are treated with special logic described in Section 5.1.5 to account for their unique interactions with other vacancies and the UO_2 crystal.

The general execution of the KMC algorithm is illustrated in the flow chart shown in Fig. 5.1. Inputs are read from a user provided text file. The system is initialized by building the U and O sub-lattices and placing all the U, O, and compound (i.e. filled tri-vacancy) vacancies throughout the system, and the initial jump frequencies are calculated. Then the jumps begin. For each jump, the current cumulative rate constant catalog of the current state of the system is calculated. A random number between 0 and 1 is chosen and multiplied by the total rate constant k_{tot}. This value represents the next event in the KMC progression. A binary search algorithm identifies the next event. The system moves according to the chosen event and the atom and vacancy positions are updated. The time step for the previous jump is found from Equation (5.5) and added to the total simulation time. If outputs are requested after the current time step, they would then be processed. If the maximum number of jumps had not yet been reached the simulation would loop back to begin building the current cumulative rate constant catalog for the next step.
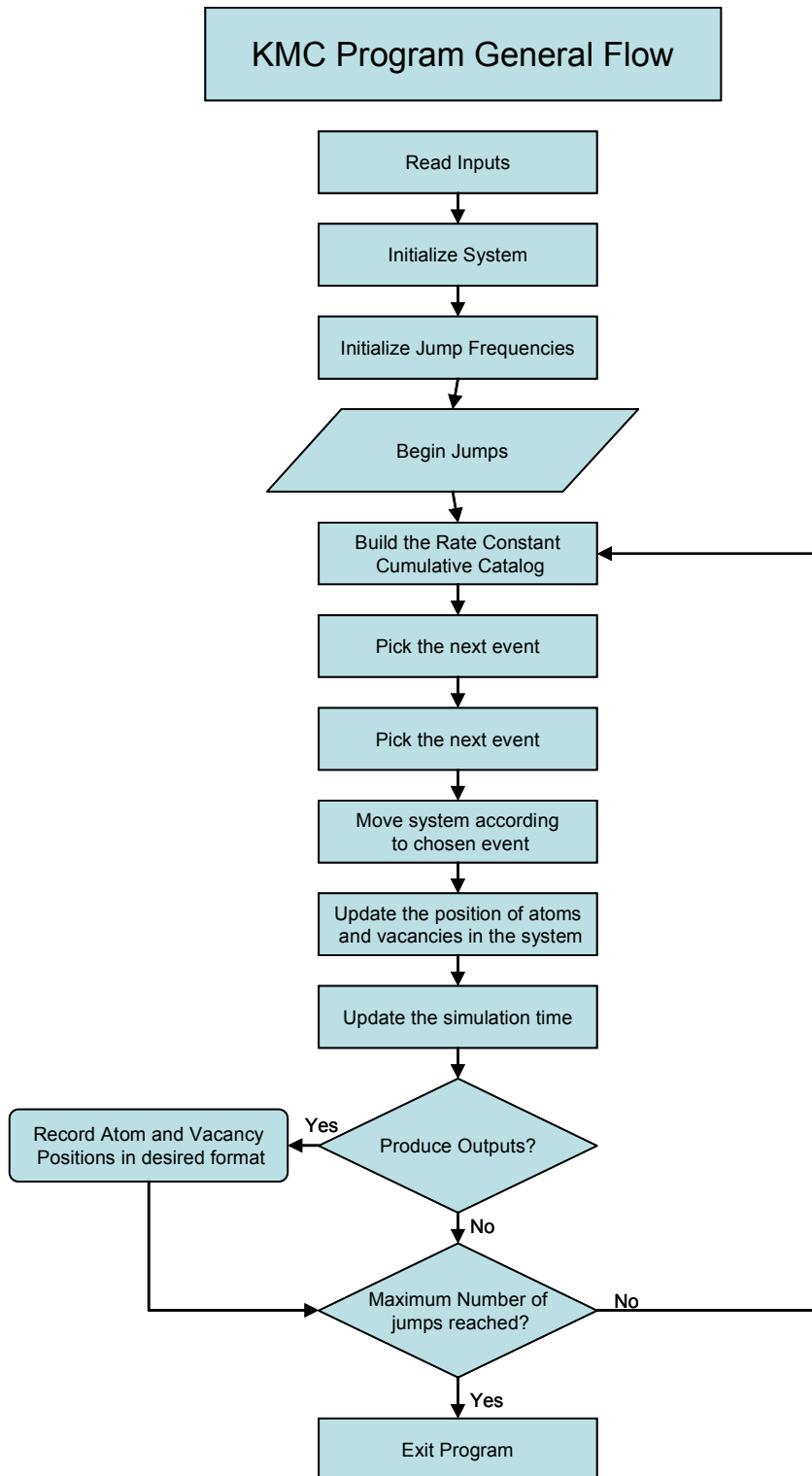
Fig. 5.1. General Execution Flow Chart of Processes in KMC algorithm

Similar to Molecular Dynamics, the outputs of a Kinetic Monte Carlo Simulation are essentially the atomic positions at different simulation times. This KMC simulation will produce 2 primary types of outputs. The first is simply the trajectory of the filled tri-vacancy. The other more complex output is the trajectory of all atoms and vacancies in the system that is formatted in a DL_POLY_2.20 HISTORY file format. This format allows for easy use of tools that were previously developed for MD simulations including the calculation of correlation functions and visualization of the atoms and vacancies moving through the simulation.

5.1.3 KMC Testing: Self-Diffusion of Oxygen and Uranium

After the KMC code was created, it was tested and compared to the self-diffusion of O and U atoms. Self-diffusion is a good test of the KMC algorithm to diagnose any problems that might be present in the software. The results of MD calculations were used to largely determine the barrier height and jump frequency pre-exponential values used as inputs into the algorithm. In the case of O vacancy migration, the migration energy was taken from the O self-diffusion calculations of UO_2 with preexisting vacancies ($UO_{2-0.0025}$) that were discussed in Section 4.2.1. The results of the MD simulations implied an energy barrier height value of 0.577 eV would be used for O in the KMC simulations. For Uranium atoms, the Molecular Dynamics saddle point calculations also described in Section 4.2.1, in which an atom is frozen in place hoping from one vacancy to another at the potential energy saddle point between the vacancies, were used for the U vacancy barrier height energy of 4.8 eV. As was previously discussed, both these values agree well with experimental results of 0.51 eV for O [64] and 4.4 eV for U, [67]. To set the proper value for the jump frequency pre-

exponential factor (v_0), KMC simulations of a 10x10x10 unit cell UO_2 system were performed with 10 O vacancies ($UO_{2-0.0025}$) at different temperatures with the jump frequency pre-exponential factor set to the Debye frequency of O in UO_2 at 0 K. The v_0 value was then adjusted to 3.890 fs^{-1} in order to closely match the corresponding MD results. Similarly, the U vacancy self-diffusion behavior was also explored using the KMC code. Ab Initio calculations of UO_2 were performed to calculate the phonon frequency distribution of U and O in UO_2. In the KMC simulations, the jump frequency pre-exponential factor for U (v_0) was set to the average phonon frequency for U in UO_2 from these calculations of 0.0037867 fs^{-1} [73]. The derivation of this value from the phonon frequency distribution of UO_2 is detailed in Appendix B. This value corresponds to experimental phonon frequency distributions that found the range of phonon frequencies for U in UO_2 to be 3.0 – 5.0 THz [74]. The primary input data for the KMC simulation is summarized in Table 5.1 along with comparisons to other reported values.

Table 5.1. Input Parameters for KMC Simulation

Data	KMC Inputs (this work)	Experiment	Atomistic Simulation
$E_{m,O}$ (eV)	**0.577**	0.51 [60]	0.58 [62], 1.24, 0.63 [51]
$v_{0,O}$ (fs^{-1})	**3.890**		
$E_{m,U}$ (eV)	**4.8**	4.4 [64], 5.6 [63]	4.43, 3.09 [51]
$v_{0,U}$ (fs^{-1})	**0.003787**		

Bold border indicates use in KMC simulations for this work

With the inputs finalized, the O atom self-diffusion behavior of $UO_{2-0.0025}$ simulated by KMC is compared to the MD simulated behavior and the experimental behavior [64] in Fig. 5.2. This comparison between experimental results and simulations should be treated

qualitatively as it is difficult to ensure that the structure of UO_2 in the experiment is duplicated faithfully by simulation.

However, the similarity in slope indicates good agreement as far as the energetics of the migration process is concerned. Additionally the similarity of the MD results and the KMC results for O self-diffusion show that data is accurately being passed from the MD simulation scale up to the KMC simulations scale.
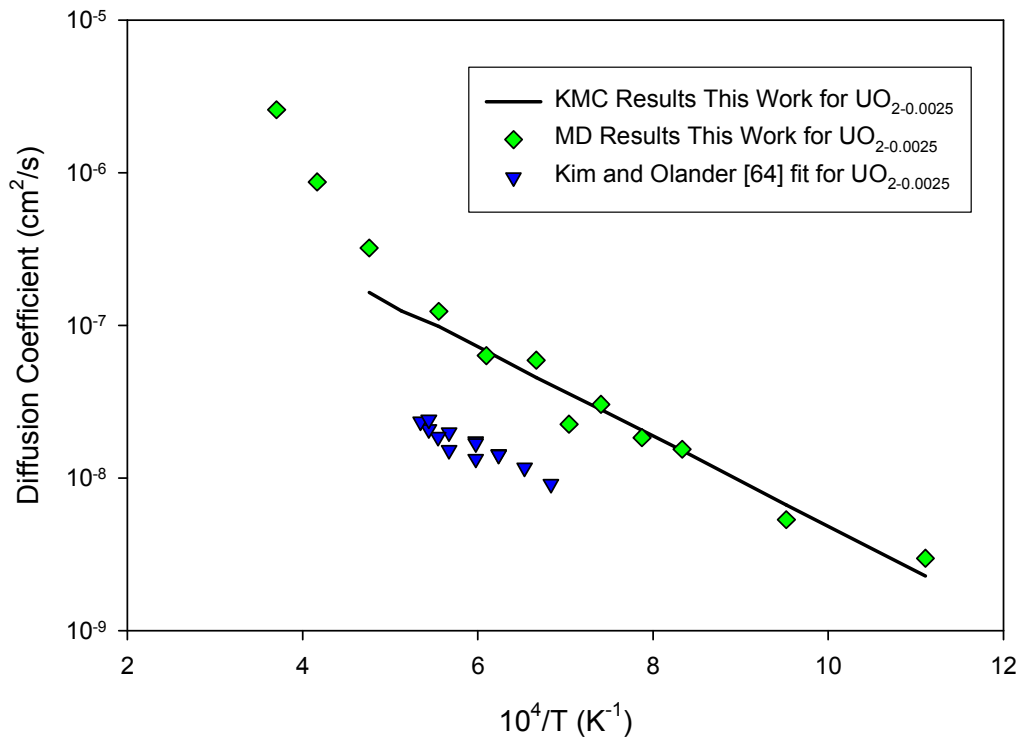
Fig. 5.2. KMC simulation of O vacancy assisted self-diffusion in UO_2 compared to experimental measurements and MD simulations

The KMC simulation of the behavior of U vacancy diffusion through the bulk UO_2 crystal is shown in Fig. 5.3 and compared to two different experimental measurements [67], [68]. Both U diffusion experiments were performed on single crystal UO_2 specimens. The different sets experimental of data utilize different techniques to analyze the diffusion of

tracers through the single crystal specimens. The study in Reference [67] observed tracer motion using alpha spectroscopy, and the study in Reference [68] used Secondary Ion Mass Spectrometry. Both studies took special precautions such as extended anneal times to insure the observation of volume bulk diffusion of U through UO_2 which make them especially appealing for comparison to the KMC diffusion. The absolute magnitude of the diffusion coefficient for the KMC simulation is very near the results from the study by Sabioni et al [68]. However, the wide scatter in the magnitude of reported U self-diffusion coefficients in literature should be noted. The similarities in migration energy between the KMC results and the experiments are significant as the migration energies are consistently similar in literature [68]. The KMC results have a migration energy of 4.8 eV, the Sabioni et al [68] experiment revealed a migration energy of 4.4 eV, and the Matzke [67] data has a migration energy of 5.6 eV. When using the frequency pre-factor from Table 5.1, the U vacancy self-diffusion data fell very close to the Sabioni data. The agreement between the KMC data and the Sabioni data is considered coincidental and is not due to any fitting of the experimental data.

The results in Fig. 5.3 demonstrate a reasonable ability for the KMC approach to describe the process of vacancy drive O and U self-diffusion in UO_2. Since this process was well studied previously, the noted level of agreement validates the implement simulation approach. Additionally the O and U self-diffusion simulations demonstrate the linking of different atomistic simulation techniques that operate in different time and length scales. With these results it well understood, it is then possible to extend the KMC simulations to account for the behavior of Kr and Xe in the UO_2.
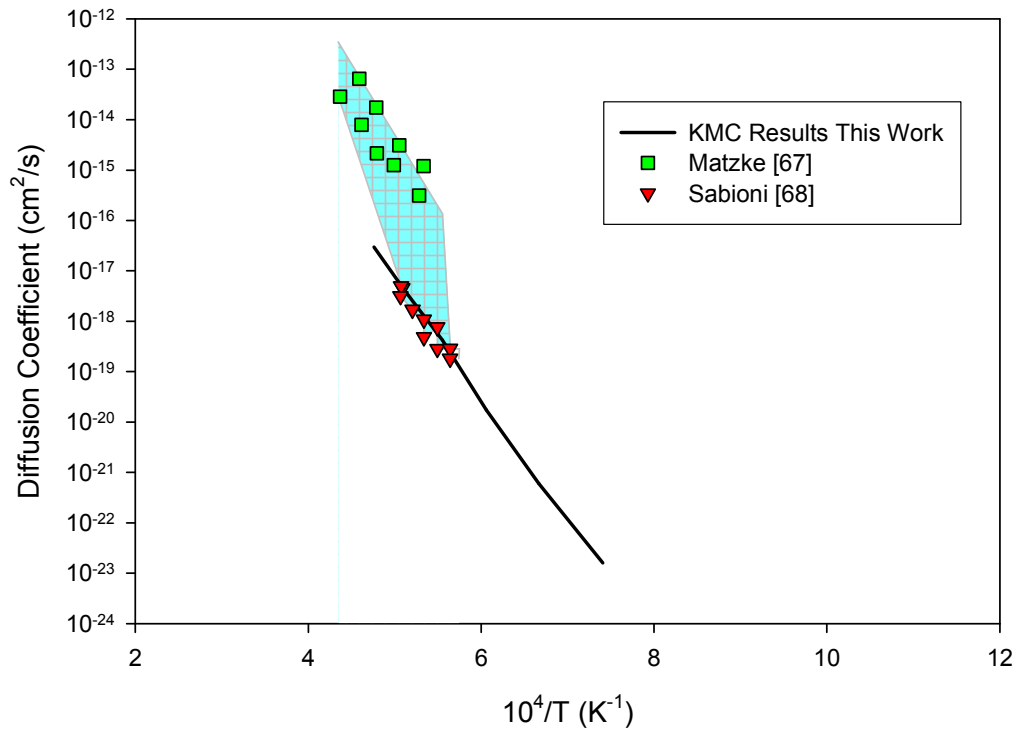
Fig. 5.3. KMC simulation of U vacancy self-diffusion in UO_2 compared to experimental measurements

5.1.4 Exploring the Filled Tri-vacancy Migration Pathway

In section 4.1.6, the proposed migration mechanism for Kr and Xe is discussed. This "filled tri-vacancy" mechanism is considered the most probable migration mechanism based on simulations in this work and in the literature [45] that show that Kr and Xe will be favorably trapped in the neutral tri-vacancy site, and experimental data that suggested Xe migration is not enhanced solely by the addition of U vacancies to the fuel [49]. Before proceeding with the migration mechanism it was important to confirm the existence and stability of Schottky defects in the UO_2 crystal. The existence of Schottky defects in UO_2 crystals from radiation damage was discussed earlier in Section 4.2.4 and has been reported in literature [45], [71], [72], [75]. Some molecular dynamics studies directly examined radiation damage cascades and their ability to create Frenkel Pairs and higher order clusters

like U-O di-vacancies and neutral tri-vacancies [71], [72]. Other research has observed the long time behavior of different concentrations of O and U Frenkel pairs that resulted in the formation of Schottky defects under the appropriate conditions [75].

In order to confirm that a filled Schottky defect was stable and would not begin to disassociate during diffusion, MD simulations with empty and filled Schottky defects were completed. In the simulations there was not U self-diffusion as expected, but there were marked differences in the O self-diffusion behavior of crystals with empty and filled Schottky defects. These differences can be found by examining Fig. 5.4. In general it appears that O in a crystal with filled Schottky defects will not begin to diffuse until thermal vacancies begin to form, but empty Schottky defects will readily disassociate without any additional energy barrier to O vacancy migration. For empty Schottky defects the vacancy assisted self-diffusion of O was almost identical to the behavior of O in UO_2 with the same concentration of preexisting O vacancies. However, the self-diffusion of O in UO_2 with either Kr or Xe filled Schottky defects is significantly lower in magnitude especially at lower temperatures. For the case of Xe filled Schottky defects the O self-diffusion behavior matches the behavior of UO_2 with no preexisting vacancies. Indicating that the O vacancies present in the Schottky defects are strongly bound to the defect and cannot diffuse as easily as the O vacancies in the empty Schottky defects. The O vacancies in Kr filled Schottky defects also found to be more strongly bound to the defect cluster than in the empty Schottky defect. However the strength of the bond is not as strong as in the Xe case. The stabilizing effect of the Kr and Xe on the Schottky defects is derived from the MD potentials accounting for the large size of the Kr and Xe atom in the defect. The large spherically shaped electron

110

cloud structure of Kr and Xe will repel O atoms that are attempting to hop into the O vacancies of the Schottky defects consequently stabilizing the defect.
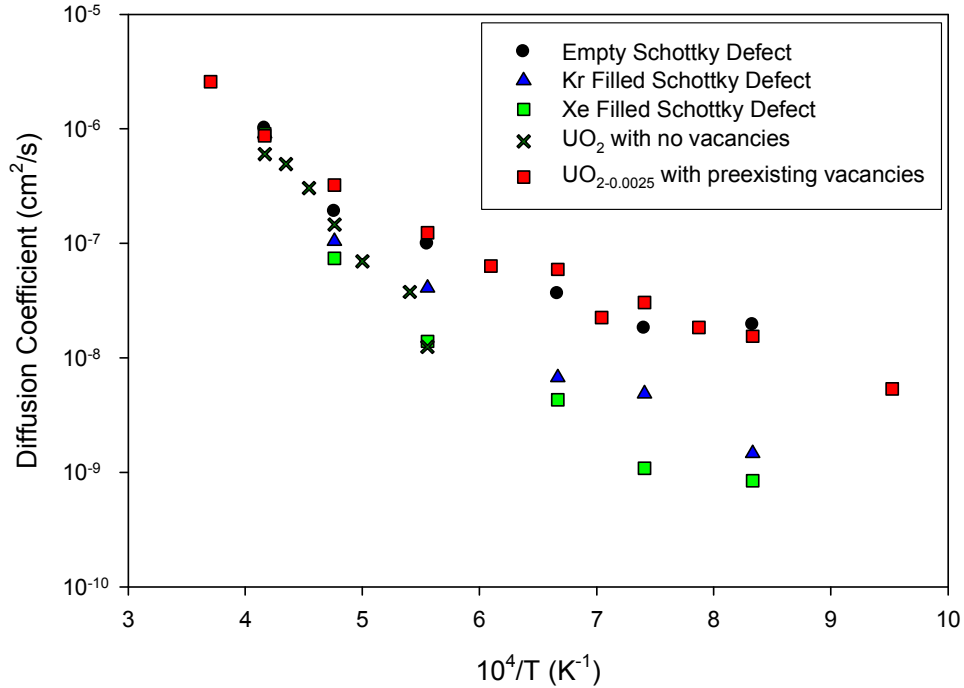
Fig. 5.4. Comparison of MD simulations for vacancy assisted self-diffusion of O in UO_2 crystals that have empty or filled Schottky Defects or crystals that contain no or preexisting vacancies

In the KMC simulation, the O and U vacancies usually move about the crystal lattice with little to no change in the probability of a jump occurring. One exception to this is the motion of U vacancies leaving a filled tri-vacancy after the formation of a charged tetra-vacancy. This event is illustrated in going from state (c) to state (d) of Fig. 4.2. In additions to the normal barrier to migration, U vacancies leaving the filled tetra-vacancy configuration must overcome an additional barrier due to the Kr or Xe filling atom. When a vacancy leaves the filled tetra-vacancy, an atom must move in to take its place. The large Kr or Xe atoms will resist the approach of the U atom. Molecular Dynamics simulations of this process were

performed to estimate the additional barrier height that Kr or Xe added to the U vacancy migration. In the MD model of UO_2, U atoms were placed at the saddle point between their original lattice positions and one of the U vacancies of the filled tetra-vacancy defect. The equilibrium energy of this configuration was compared to the equilibrium energy of the filled tetra-vacancy defect and U atom in its original lattice site. The additional barrier to diffusion above the 4.8 eV barrier to normal U vacancy diffusion was simulated to be approximately 1.0 eV for Kr and 1.5 eV for the larger Xe atom. This additional energy consideration was added to the KMC code as an adjustable parameter for the change in energy for U vacancies leaving the charged tetra-vacancy configuration.

The Schottky defect simulations and the barrier height simulations establish the behavior of the O and U vacancies that comprise the filled tri-vacancy in the KMC simulation. The results shown in Fig. 5.4 establish that the O vacancies in a filled tri-vacancy will not disassociate once they are bound to a filled tri-vacancy. The additional energy barrier for the U vacancies to leave the filled tetra-vacancy defect, establish a distinction between Kr and Xe in the KMC simulations. With these two checks of the filled tri-vacancy mechanism complete, the diffusion of Kr and Xe through UO_2 can now be investigated with the KMC simulation.

## 5.1.5 KMC Simulation of Kr / Xe Diffusion

With the KMC algorithm properly tested against O and U self-diffusion, it was then possible to begin simulating the diffusion of Kr and Xe through the UO_2 crystal using the migration mechanism from Fig. 4.2. Special logic was developed for both O vacancy interaction with the filled tri-vacancy and U vacancy interaction with the filled tri-vacancy.

Additionally, the change in U vacancy barrier height for movement out of the filled tetra-vacancy was also accounted for in the KMC algorithm.

The interaction of free O and U vacancies with the filled tri-vacancy is handled by a special set of logic in the KMC program. Certain particular atomic configurations trigger specific vacancies moves in the system. Normally the O and U vacancies that make up the filled tri-vacancy are considered stable based on the results of Fig. 5.4, but these vacancies will become activated through interaction with the free vacancies in the system. When a third O vacancy approaches the filled tri-vacancy, one of the three O vacancies will be released from the vacancy cluster. All three vacancies are considered to have the same probability to escape. In the next move, one of the O vacancies will leave the cluster, and the remaining vacancies are now treated as the O vacancies that are bound to the filled tri-vacancy. When a free U vacancy approaches a filled tri-vacancy, it will also interact using special rules. If the free U vacancy is the correct distance from the O vacancies of the tri-vacancy and a nearest neighbor to the U vacancy of the filled tri-vacancy, the Kr or Xe will be considered to have associated more closely with one of the U vacancies freeing the other one to migrate away on the next move. When this move out of the charged tetra-vacancy configuration occurs, the additional energy barrier discussed in Section 5.1.4 is accounted for in the jump frequency of the potentially departing U vacancies. The additional energy barrier was modeled as a variable input parameter to the KMC program. To find to diffusion coefficient of the simulated Kr or Xe, the trajectory of particle was periodically output. Multiple independent KMC simulations were performed and the trajectories of each simulation were used to calculate the mean square displacement of the set. After the KMC

simulation was complete, the mean square displacement of the set of Kr or Xe trajectories was transformed into the diffusion coefficient using Equation (4.6).

The simulated diffusion coefficient of a Kr or Xe atom migrating through a UO_2 crystal using the migration mechanism discussed in Fig. 4.2 is shown in Fig. 5.5. The effect of the additional energy barrier to the final U vacancy move in the migration mechanism is shown for several different energies ranging from 0.5 eV to 2.0 eV including the 1.0 eV that was estimated for Kr and the 1.5 eV that was estimated for Xe from the MD calculations in Section 5.1.4.
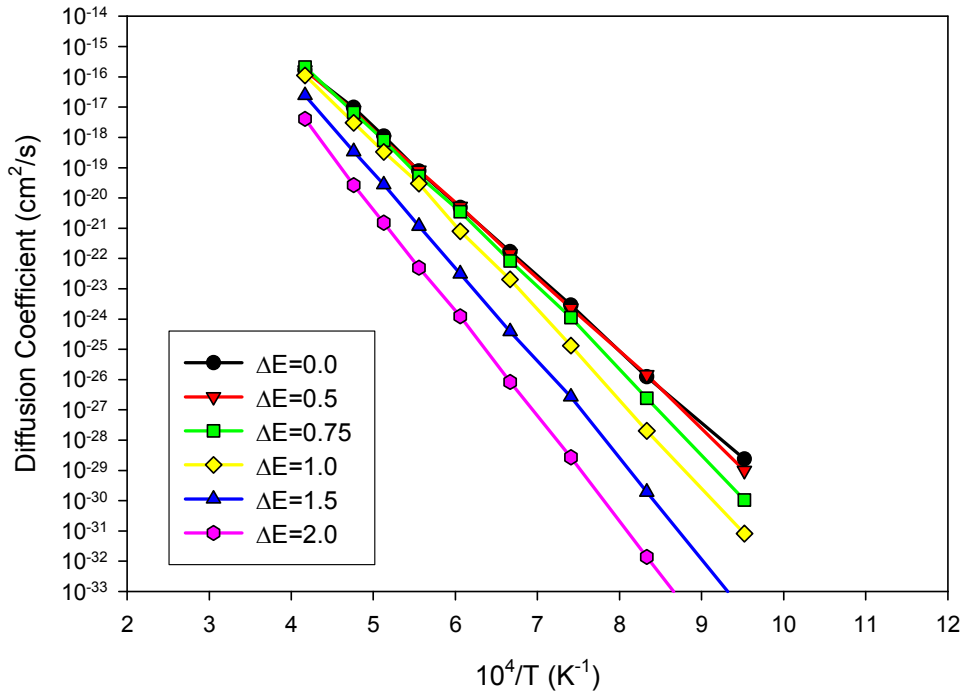
Fig. 5.5. KMC Calculation of the bulk crystal diffusion of Kr and Xe through UO_2 for different additional diffusion barriers

In Fig. 5.5 the Diffusion coefficient for the filled tri-vacancy with no additional energy barrier to U atom diffusion follows the same temperature dependent Arrhenius relationship as U vacancy self-diffusion shown in Fig. 5.3. However, the absolute magnitude of the tri-

vacancy diffusion is approximately 4 times lower than U vacancy diffusion. From these results, it is clear that U vacancy self-diffusion is the rate controlling process for Kr and Xe migration by the tri-vacancy mechanism as was predicted in Reference [45] and [76]. The movement of the U vacancies that is required for the migration of the filled tri-vacancy is much slower than the O vacancy migration that rearranges the filled tri-vacancy. The rate of Kr and Xe migration will always be controlled by the slowest pathway in its migration mechanism, which is U vacancy diffusion.

In Fig. 5.5 as the energy barrier that accounts for the tri-vacancy being filled is increased the migration energy begins to increase also. At about $\Delta E = 0.5$ there begins to be a slight increase in the effective migration energy of the filled tri-vacancy defect. At $\Delta E = 0.75$ eV the effective migration energy is 0.47 eV greater than 4.8 eV equaling 5.27 eV, and at $\Delta E = 1.0$ the effective migration energy is 0.83 eV greater than 4.8 eV equaling 5.63 eV. Past $\Delta E = 1.5$ eV the effective migration energy begins to have a one to one relationship with the change in energy. The effective migration energy for $\Delta E = 1.5$ eV was 6.3 eV, and the effective migration energy for $\Delta E = 2.0$ eV was 6.8 eV. Making the barrier lower for the U move out of the defect complex has no effect on the effective migration energy of the filled tri-vacancy.

The self part of the Van Hove correlation was calculated for a Kr or Xe atom migrating through the UO_2 crystal using the tri-vacancy mechanism. The results of 1000 independent KMC simulations were combined to examine how this function changed as a function of time in the KMC simulation. The early evolution where on average the migrating atom is near its origin is shown in Fig. 5.6. The behavior of the atoms as time progresses late into the simulation is shown in Fig. 5.7.
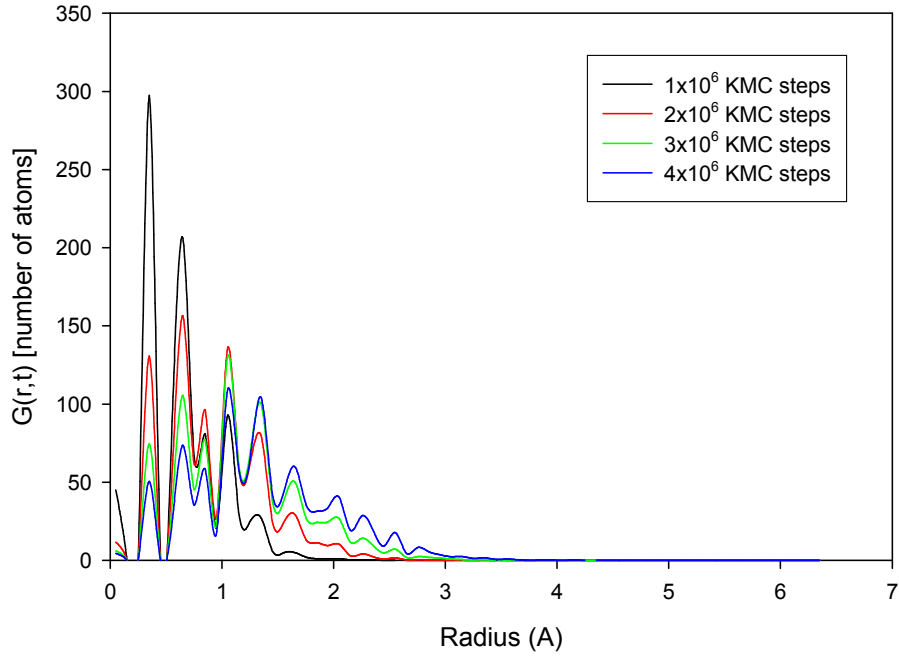
Fig. 5.6. Early time behavior or the self part of the van Hove correlation function for Kr or Xe migrating through a UO$_2$ crystal
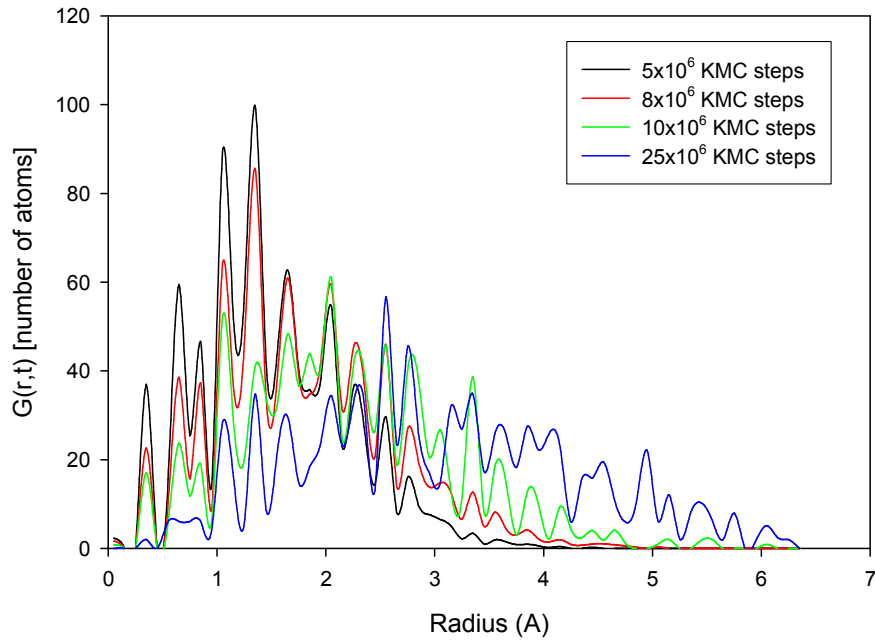
Fig. 5.7. Long time behavior or the self part of the van Hove correlation function for Kr or Xe migrating through a UO$_2$ crystal

116

The interpretation of these plots is slightly different than in the case of O self-diffusion. The peaks present in Fig. 5.6 and Fig. 5.7 do not directly correspond to lattice positions they are an artifact of the discreet positions possible in the KMC simulation. In Fig. 5.6 most of the tracked atoms are still near their origin, but by the time steps shown in Fig. 5.7 the atoms have begun to move around the system. The correlation function has started to take on a roughly Gaussian shape that is unlike the shape seen in the O self-diffusion calculations. The Gaussian shape is due to each tracked atom being independent from each other, which is unlike the O self-diffusion case where the system of atoms is correlated by the atomic structure. The broadening of the roughly Gaussian shape of $G_s(r,t)$ for Xe is the expected behavior of fluids and leads to the relationship seen in Equation 3.11 that relates $G_s(r,t)$ to mean square displacement. If the simulation is continued for long enough the correlation function will become a flat line equal to a set of single atoms that are uncorrelated with their origin.

The diffusion coefficients from KMC simulation are plotted versus several different sets of experimental data in Fig. 5.8. The first set is an experimental fit to the diffusion of single gas atom Xe through poly-crystalline UO_2 from Matzke [57]. The reported migration energy from the empirical fit is 3.9 eV ± 0.4 eV. A second empirical fit with a migration energy of 3.04 from Davies and Long is also plotted in Fig. 5.8 [77]. The magnitude of the diffusion derived from simulation is significantly lower than experimental measurements, but the temperature behavior is very similar. The experimental data is taken from polycrystalline tests which will have enhanced diffusion over single crystal experiments and simulations. It is also instructive to examine the diffusion coefficients from KMC simulation plotted against

the diffusion coefficients used in the various R/B models for Kr / Xe release from failed

TRISO particles discussed in Section 2.1. A more detailed discussion with all the applicable

equations and terms is available in References [1], [14], [15], and [16].   Diffusion

coefficients from the PARFUME / German model, JAERI model and GA model for Xe

release are co-plotted with the simulated KMC diffusion coefficients in Fig. 5.8. These sets

of data are taken as a general range of experimental data and are referred to collectively

throughout this chapter in subsequent figures.
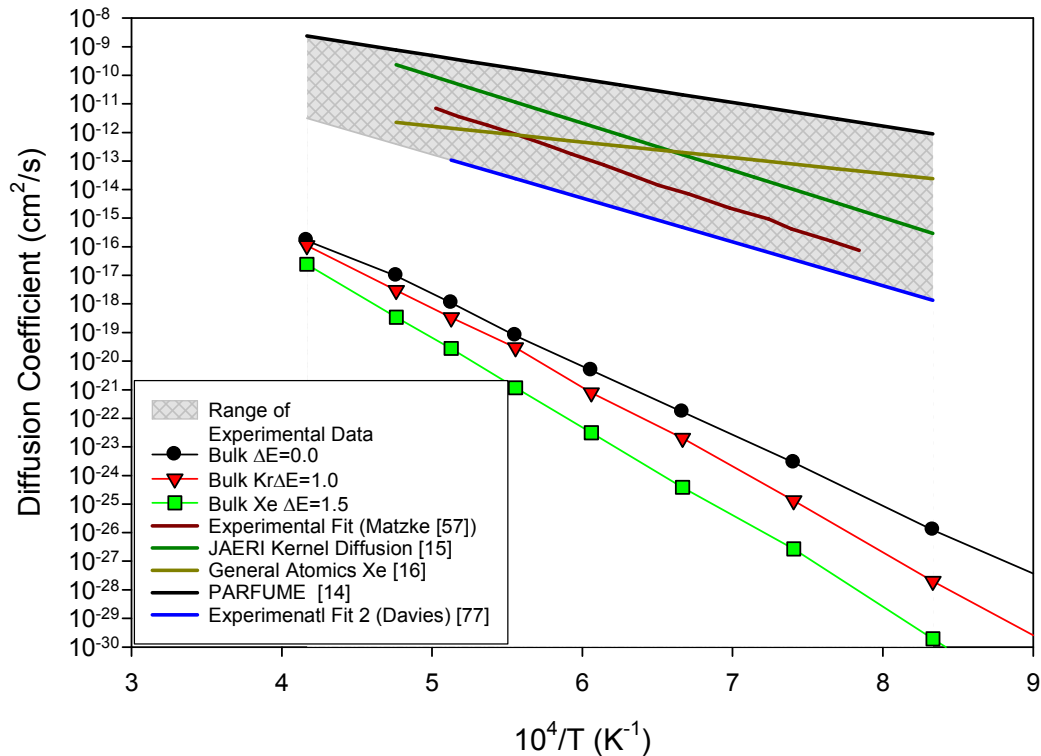
Fig. 5.8. KMC Calculation of the bulk crystal diffusion of Kr and Xe through UO_2 for different diffusion
barriers compared to Diffusion Coefficients from different Release to Birth Ratio Models for failed
TRISO particles

From the Arrhenius plot shown in Fig. 5.8, the KMC simulated diffusion coefficient is

much lower than the Xe diffusion coefficients from experiment and R/B models. There are

many possible sources of the differences in the diffusion coefficient magnitudes that can stem from changes in both major components of Equation (4.22) the migration or diffusion energy (E_D) and the pre-exponential term (D_0). The key difference between the KMC results and the other diffusion coefficients is the KMC results are a simulation of only bulk or intragranular diffusion of Kr or Xe through the UO_2 crystal, while the experimental and empirical diffusion coefficients are reporting the diffusion of Kr and Xe out of polycrystalline UO_2. The presence of grain boundaries in this experimental data enhances the diffusion as was discussed in Section 4.2.2 by lowering the barrier to vacancy diffusion. At the grain boundaries, U atoms in the crystal will diffuse with a lower barrier energy enhancing Kr and Xe diffusion. Additionally, as crystal grain sizes shrink, smaller crystal grains will replace the larger grains leading to a net increase in the total grain boundary surface area that is proportional to the ratio of the original grain radius to the new grain radius. With smaller grains, a larger fraction of atoms will be grain boundary atoms leading to further increases in diffusion coefficient magnitude as seen in Fig. 4.9.

By comparing the results of the KMC simulations of bulk crystalline Kr and Xe diffusion to the diffusion coefficients of the R/B models, it is possible to draw conclusions about the noble fission gas physics taking place during previous experiments. In Fig. 5.8 the R/B models have several different effective migration energies. The PARFUME / German and GA models have lower effective migration energies of 1.6 eV and 1.1 eV respectively. The slope of the JAERI model diffusion coefficient is equivalent to 3.27 eV which is closer to the theoretically expected behavior of U vacancy self-diffusion controlling Kr and Xe diffusion. The polycrystalline nature of the experimentally measured UO_2 helps explain the change in

the observed effective migration energy. The large difference in migration energies suggest that perhaps the time and temperature conditions observed to create the PARFUME and GA models only observed Kr and Xe escaping from grain boundaries. The larger JAERI migration energy suggests the temperature range used in these test could actually observe some of the intragranular diffusion that was occurring in the fuel. However the grain boundary effects possibly present in the PARFUME and GA model still lead to an effective migration energy that is lower than the expected theoretical migration energy from atomistic calculations.

5.1.6 Impact of Grain Boundary on KMC Simulation

The large difference in experimental and KMC simulated diffusion coefficients can be partially attributed to the polycrystalline nature of UO_2 that exists in the reference experiments. The importance of grain boundary diffusion or intergranular diffusion and how it impacts the behavior of poly crystalline material was discussed in Section 4.2.2. Evidence of grain boundary behavior in Xe diffusion experiments has been specifically studied in literature [61]. In order to further explore the different important diffusion mechanisms in UO_2, the KMC algorithm was modified to be able to simulate a grain boundary region running through a perfect crystal. The code changes that were necessary to implement grain boundaries in KMC and the impact the grain boundary had on the results of O and U self-diffusion and the Kr / Xe bulk diffusion mechanism will be discussed.

Several code changes were included to account for the grain boundary region. Most notably the input was changed to include new energy barriers for O and U atoms in the grain boundary region and a parameter was added that stipulated the distance from the grain

boundary that was considered the grain boundary region. Inside the code the grain boundary was implemented as a plane of Schottky defects at the center of the KMC simulation crystal. Vacancies treated the grain boundary as a barrier that could not be crossed. This treatment assumes that the grain boundary acts as an equilibrium source and sinks for vacancies. This limits atom and vacancy motion in one direction, but preserves periodic boundary conditions in the other two dimensions. During the simulation, each vacancy is checked after it makes a move to see if it is in a grain boundary region. If in the grain boundary region the rate constant for that vacancy is updated to reflect its lower energy barrier to motion. Otherwise the KMC simulation proceeds as previously described in Section 5.1.1.

Changes in diffusion behavior for O and U self diffusion due to the grain boundary were studied using the KMC program. The energy barrier in the grain boundary region was set to half the normal vacancy diffusion barrier. A difficulty can arise when studying processes in KMC that occur on widely different time scales. Small changes in energy barrier can have a very large effect on the rate constants and the subsequent rate constant library used to calculate the time step of a particular move in KMC. This is the case for Grain Boundary simulations. The vacancies in the grain boundary region have a much higher probability of being chosen for a move than the vacancies in the bulk crystal region. Initially almost all moves in the simulation will be vacancies in the grain boundary region. Eventually the vacancies present in the simulation will migrate out of the grain boundary region to the bulk region where they will only occasionally return to the grain boundary region.

To counter act this behavior in the KMC simulation, the model described in Section 4.2.2 and typified by Equation (4.29) for the effective grain boundary diffusion coefficient for self-

diffusion was applied to the KMC simulation for O and U self-diffusion. Two separate KMC simulation sets were carried out, one where only the grain boundary diffusion was measured and another where only the bulk self-diffusion was measured. The two sets of data (D_{gb} and D_{bulk}) were combined to find the effective diffusion coefficient (D_{eff}) for self-diffusion in UO_2 of different grain sizes.

The behavior of the O self-diffusion coefficient from the KMC simulation with grain boundaries is shown in Fig. 5.9 for grain sizes ranging from 0.01 micron to 1 micron in diameter. For O self-diffusion, UO_2 grains larger than about 1 micron in diameter result in an effective diffusion coefficient that is nearly equivalent to the bulk diffusion. Only with very small grain sizes can grain boundary O self-diffusion dominate the effective diffusion coefficient. However UO_2 is normally formulated with grain sizes of 10 to 20 μm [50].
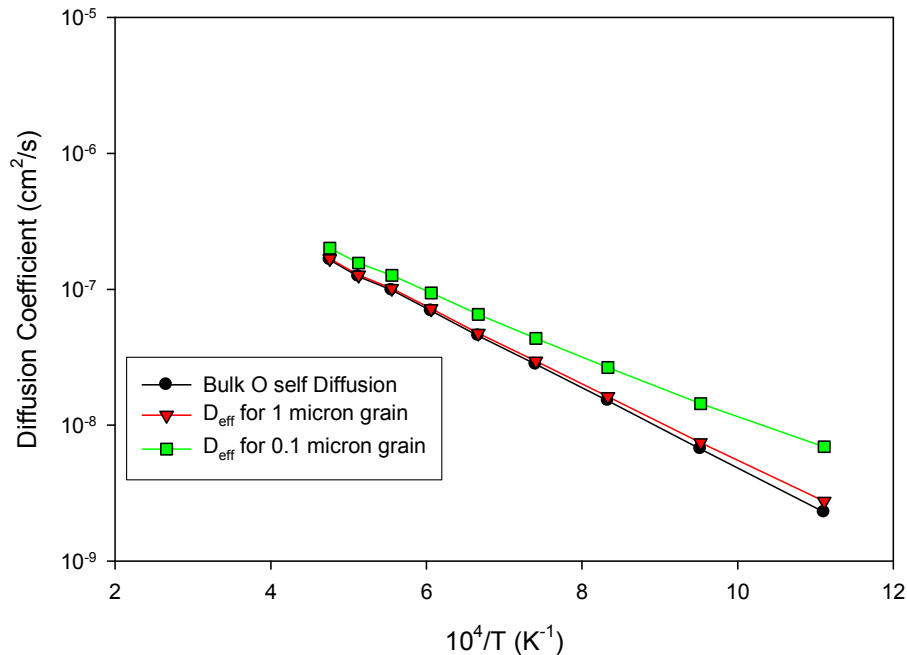
Fig. 5.9. O self-diffusion with Grain Boundary effect in $UO_{2-0.0025}$

As expected the effective diffusion coefficient shifts from the bulk diffusion behavior to the grain boundary diffusion behavior as the grain size shrinks. The fraction of atoms in the grain boundary (g from Equation (4.29)) increases as the grain size shrinks. In the 0.1 micron grain size data the dual behavior of the effective diffusion coefficient is most pronounced, where the high temperature diffusion coefficients follow the bulk diffusion coefficient Arrhenius slope of 0.577 eV and the lower temperature diffusion coefficients follow the slope from the grain boundary diffusion coefficient of 0.2885 eV more closely. The minor impact grain boundaries have on O self–diffusion for nominal formulated UO_2 is expected theoretically due to its relatively small migration energy, which has been verified experimentally [78].
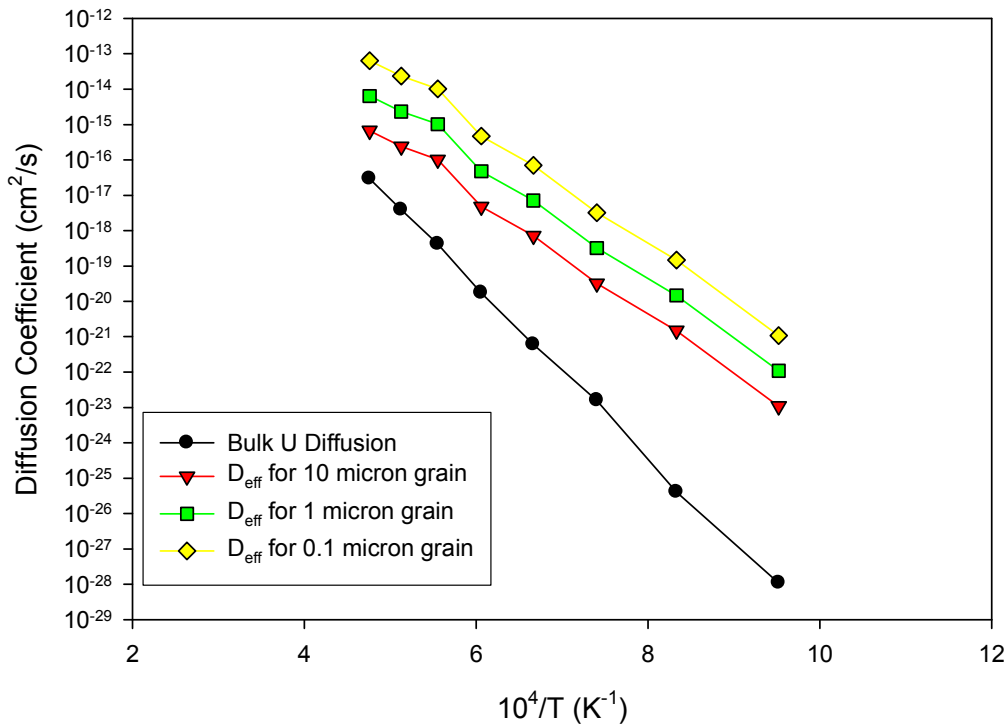
Fig. 5.10. U vacancy self-diffusion in UO_2 with Grain Boundary effect

The Uranium vacancy self-diffusion behavior with the grain boundary effect is shown in Fig. 5.10. The same procedure that was used to calculate the O effective diffusion coefficient for self-diffusion was also applied to the U vacancy self-diffusion case. Again as the grain size shrinks the effective diffusion coefficient moves from the bulk diffusion coefficient to the grain boundary diffusion coefficient. The Arrhenius slope of the effective diffusion coefficient also moves from the 4.8 eV slope of the bulk diffusion coefficient towards the 2.4 eV of the grain boundary diffusion coefficient. Unlike the O self-diffusion case where grains had to be very small for their effective diffusion coefficient to be dominated by the grain boundary, the much larger diffusion barrier in U results in the effective diffusion coefficient being dominated by the grain boundary behavior at most crystal grain diameters.

Just as it is very important for the effective self-diffusion coefficients, grain boundary behavior also greatly impacts Kr and Xe diffusion through UO$_2$. By assuming a constant concentration of Kr and Xe across the bulk and grain boundary, Equation (4.34) which is repeated below, can be applied to calculate the effective diffusion of Kr and Xe for UO$_2$ grains of different sizes.

$$D_{eff}^{imp} = \frac{g}{1+g} D_{gb} + \left(1 - \frac{g}{1+g}\right) D_{bulk}$$ (5.8)

The effective self-diffusion coefficient for trapped Kr migrating through UO$_2$ by the tri-vacancy mechanism is shown in Fig. 5.11, and the D_{eff} for Xe is shown in Fig. 5.12. Again two separate cases were simulated for both Kr and Xe where the grain boundary conditions were run in a KMC simulation and then the bulk diffusion conditions were simulated.
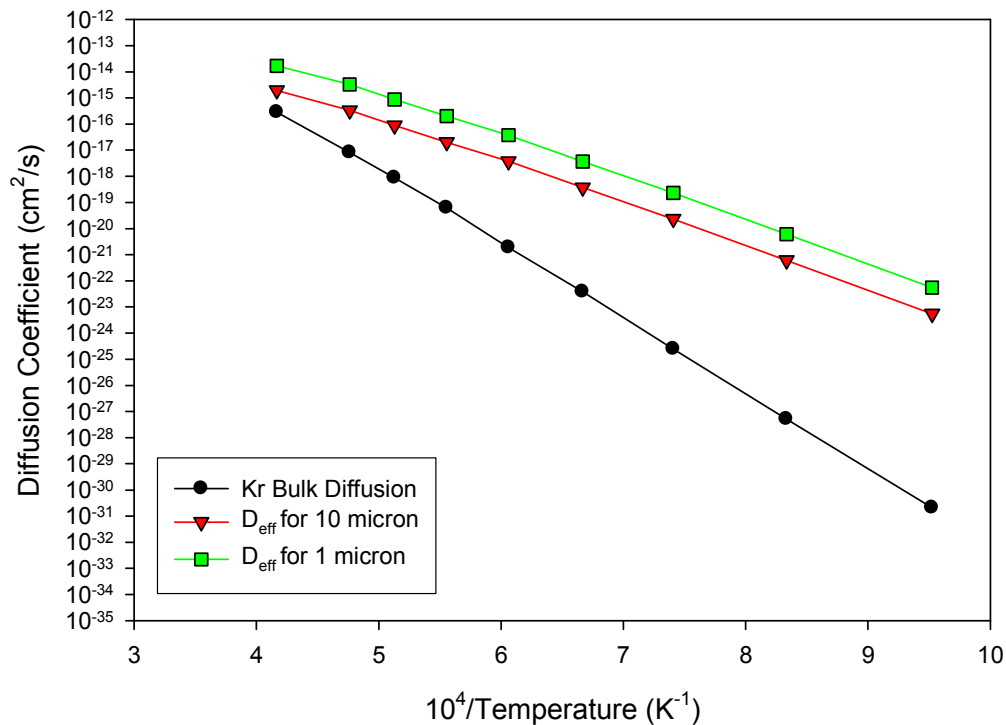
Fig. 5.11. Effect of Grain Boundary on the Diffusion of Kr in UO$_2$ using the tri-vacancy mechanism

Both Fig. 5.11 and Fig. 5.12 are plotted on the same scale to emphasize the steeper Arrhenius slope of the Xe diffusion compared to the Kr diffusion. However both noble gases respond similarly to the application of Equation (5.8) for different grain diameters. The response to grain size is also similar to the case of the effective diffusion coefficient for U self-diffusion. For grain sizes of 1 and 10 microns, the effective diffusion coefficient is more dominated by the Arrhenius slope of the grain boundary diffusion coefficient. The enhancement in the diffusion coefficient from the bulk case to the effective grain boundary diffusion coefficient is similar to the enhancement seen in other work when transitioning between a bulk and grain boundary diffusion coefficient [61].
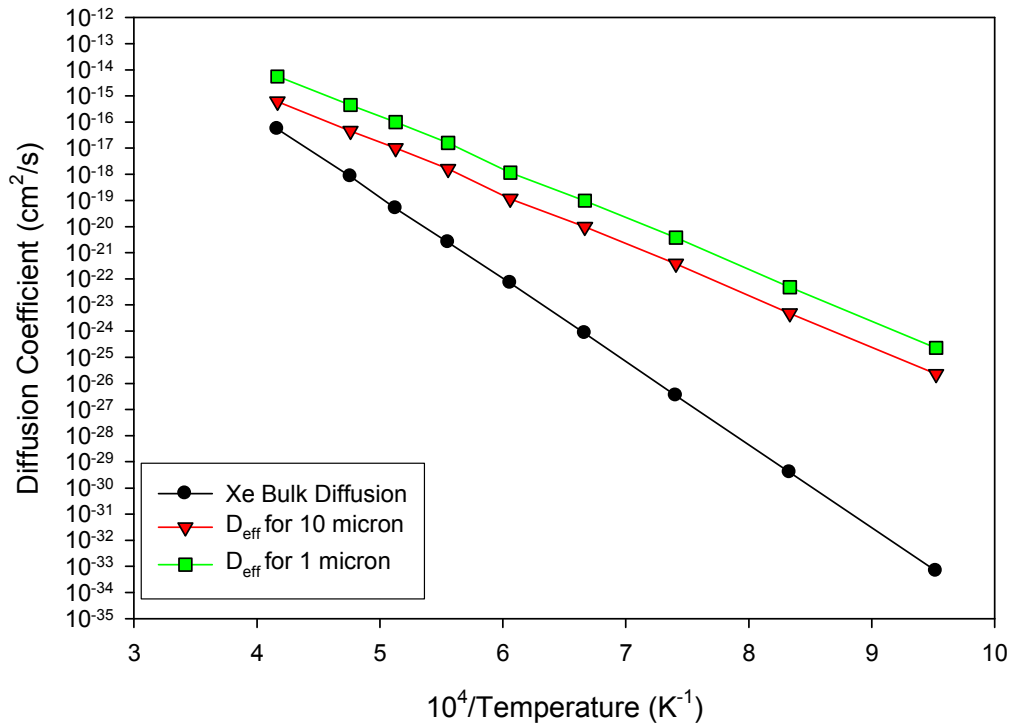
Fig. 5.12 Effect of Grain Boundary on the Diffusion of Xe in UO$_2$ using the tri-vacancy mechanism

The inclusion of the effective grain boundary concept significantly impacts the comparison of KMC diffusion coefficients derived from KMC simulation to diffusion coefficients from R/B models as seen in Fig. 5.13. The effective diffusion coefficient for 10 μm grain diameter Kr and Xe diffusion through UO$_2$ show how the inclusion of grain boundary effects can enhance diffusion by several orders of magnitude. The Arrhenius slope behavior of the effective diffusion coefficients are also more similar to the experimental / empirical diffusion coefficients shown in Fig. 5.13. The change, between the bulk diffusion coefficients from KMC to the grain size effective diffusion coefficients, show how by further refining the model, simulations can begin to approach experimental measurements.

126
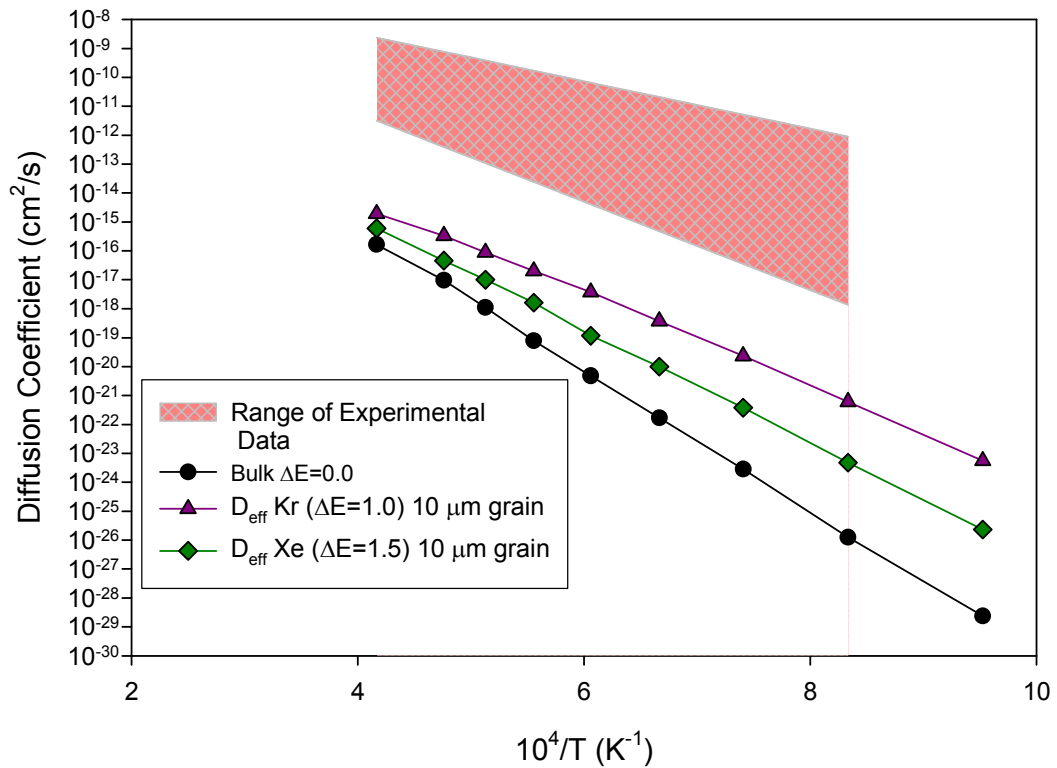
Fig. 5.13. Comparison of Diffusion Coefficients derived from KMC for both bulk diffusion and grain boundary diffusion to experimental diffusion coefficients for R/B models

5.1.7 Impact of Radiation Damage on KMC Simulation

The diffusion of Kr and Xe through UO_2 will also be influenced by the amount of radiation damage that occurs in the UO_2 crystal. In Section 4.2.2 the changes in Arrhenius behavior brought on by radiation damage were previously discussed. Recall Equation (4.21) where the diffusion of some atom 'a' by a vacancy mechanism is proportional to the probability of a neighboring site being a vacancy. This concept also applies to the diffusion of Kr and Xe through UO_2 by the tri-vacancy mechanism where the diffusion coefficient is a function of the concentration of U vacancies in the UO_2 crystal. Because the thermal concentration of vacancies is so low on the U sub-lattice of UO_2 due to its large vacancy formation energy almost all U vacancies will be due to radiation damage. The

127

implementation of additional U vacancies is fairly straight forward in the KMC simulation, and simply requires the addition of more vacancies into a system to increase the vacancy concentration to the desired level based on the irradiation conditions.

The vacancy concentration due to irradiation can be determined by applying radiation damage models that predict the number of Frenkel pairs produced under different reactor conditions coupled with a model for vacancy concentration due to Frenkel pair creation by irradiation and destruction by recombination. For this work, the NRT model [79] was used to predict the number of Frenkel pairs produced by a Primary Knock-on Atom (PKA) and is show in Equation (5.9).

$$N_{NRT} = \frac{0.8E_{PKA}}{E_d} \tag{5.9}$$

Where E_{PKA} is the energy of the PKA's in the system, and E_d is the displacement energy for the atom under investigation, which is approximately 40-50 eV for U [80]. Then NRT model was combined with a model for damage due to neutrons slowing down in a medium by elastic scattering to calculate the Frenkel Pair production rate (R_d) [13] shown in Equation (5.10).

$$R_d = N\sigma_{el}\left(\frac{0.8\Lambda E_n}{4E_d}\right)\Phi \tag{5.10}$$

Where N is the number density of Uranium, σ_{el} is the neutron elastic scattering cross section, Λ is the fraction of energy lost per neutron collision, E_n is the average neutron energy, and Φ is the neutron flux. Using the nominal conditions of the AGR-1 experiment the Frenkel Pair production rate is about 4.3×10^{14} pairs per cm^3 per second. This production rate can then be

coupled with the destruction rate due to recombination to create a model for the U vacancy

concentration as a function of time and irradiation conditions shown in Equation (5.11) [47].

$$\frac{dC_v}{dt} = R_d - K_{iv}C_iC_v \tag{5.11}$$

Where C_v is the vacancy concentration, C_i is the interstitial concentration, and K_{iv} is the

recombination rate that is determined by Equation (5.12).

$$K_{iv} = \frac{z\Omega D_v}{a^2} \tag{5.12}$$

Where z is a combinatorial factor that accounts for the number of vacancy and interstitial

position combinations that can lead to recombination, for nearest neighbors the value is 48,

but in real crystal recombination can take place at greater distances making 500 a better

number to use for the z term. In Equation (5.12), Ω is the atomic volume, D_v is the diffusion

coefficient of the U vacancy, and a is the lattice constant. Solving for the equilibrium

vacancy concentration gives a value of 3.2×10^{20} vacancies per cm^3 at 1500K, which is about

13 of every 1000 lattice sites. The displacement per atom (dpa) rate for U in the AGR-1

experiment is estimated as 1.83×10^{-8} dpa/s, which gives a final dpa at the end of 760 days at

effective full power approximately 1.2 dpa for U atoms in the final TRISO fuel. The terms

used to calculate U Frenkel Pair production by radiation damage are shown in Table 5.2

Table 5.2. Terms used to calculate U Frenkel Pair Production of in UO_2 by Radiation Damage. These values reflect the general conditions of the AGR-1 experiment.

Terms for R_d		Terms for K_{IV}	
N (atm/cm^3)	2.34E+22	z	500
σ_{el} (b)	4.7206	Ω (cm^3)	4.13E-23
Λ	0.01671	D_v (1500K)	6.02E-22
E_n (MeV)	1.0	a (cm)	5.47E-08
E_d (eV)	40		
Φ (n/cm^2/s)	4.65E+13		

The impact of increasing the number of U Frenkel pairs present in the fuel is explored in Fig. 5.14, and Fig. 5.15. The enhancement of the diffusion coefficient due to radiation damage is seen most strongly for the case where no additional energy is required to move the escaping U vacancy away from the filled tri-vacancy complex (i.e. step (c) to (d) in Fig. 4.2). The ΔE=0.0 eV case is shown in Fig. 5.14 for various different Uranium vacancy concentrations ($N_{v,U}$). The different U vacancy concentrations correspond to different levels of radiation damage, where $N_{v,U}$=0.001 is considered as a baseline concentration used for as manufactured defects, $N_{v,U}$=0.0025 is the concentration of U vacancies after about 2 days of irradiation in the AGR-1 experiment, $N_{v,U}$=0.01325 is the equilibrium vacancy concentration calculated from the conditions given in Table 5.2, and $N_{v,U}$=0.025 is a larger vacancy concentration used to demonstrate the effect of increasing radiation damage on the Kr/Xe diffusion coefficient.

In Fig. 5.15 the effective diffusion coefficient for different radiation damage levels is shown for Kr (The ΔE=1.0 eV) and Xe (The ΔE=1.5 eV). These diffusion coefficients show

little enhancement due to the increased U vacancy concentration. This is due to the additional energy barrier required to induce migration out of the U vacancy plus filled tri-vacancy complex. The change in diffusion coefficient between $N_{v,U}=0.001$ and $N_{v,U}=0.025$ is almost indistinguishable in Fig. 5.15 in contrast to Fig. 5.14 where the change is between 1 and 2 orders of magnitude. The small change in Kr and Xe diffusion due to radiation damage is not completely unexpected. In migrating by the tri-vacancy complex the diffusion of Kr and Xe is no longer strictly proportional to the concentration of U vacancies in the fuel. The vacancy complex must rearrange and interact with free U vacancies for migration to proceed [13]. Experimental results have also shown that changing the U vacancy concentration in UO_2 by the use of different valence impurities has not enhanced Xe diffusion [49].
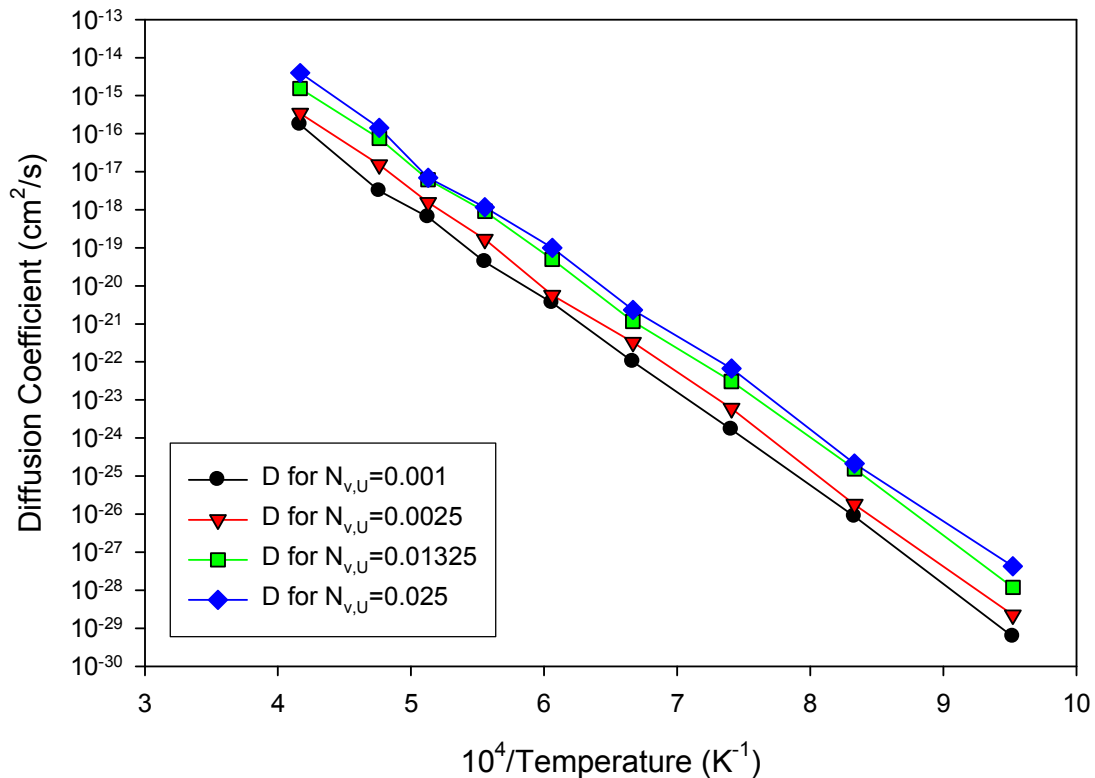
Fig. 5.14. Effect of increasing radiation damage on Kr/Xe migration through UO_2 for no increase in U vacancy saddle energy out of the filled tri-vacancy complex ($\Delta E=0.0$ eV)
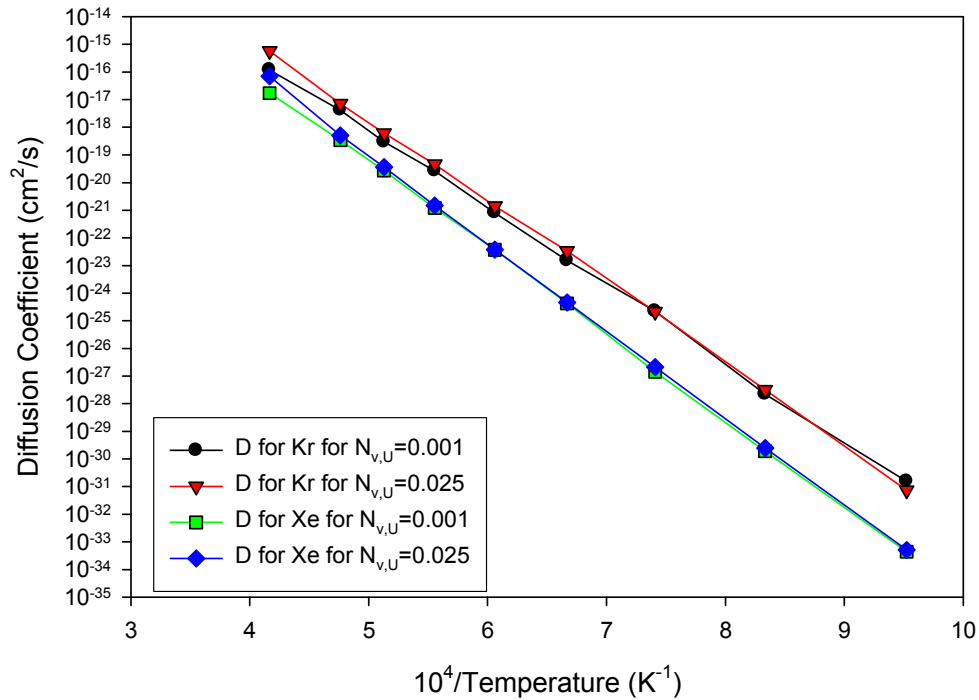
131

Fig. 5.15. Effect of increasing radiation damage on Kr /Xe migration through UO_2 with previously determined additions saddle energy for Kr (ΔE=1.0 eV) and Xe (ΔE=1.5 eV)
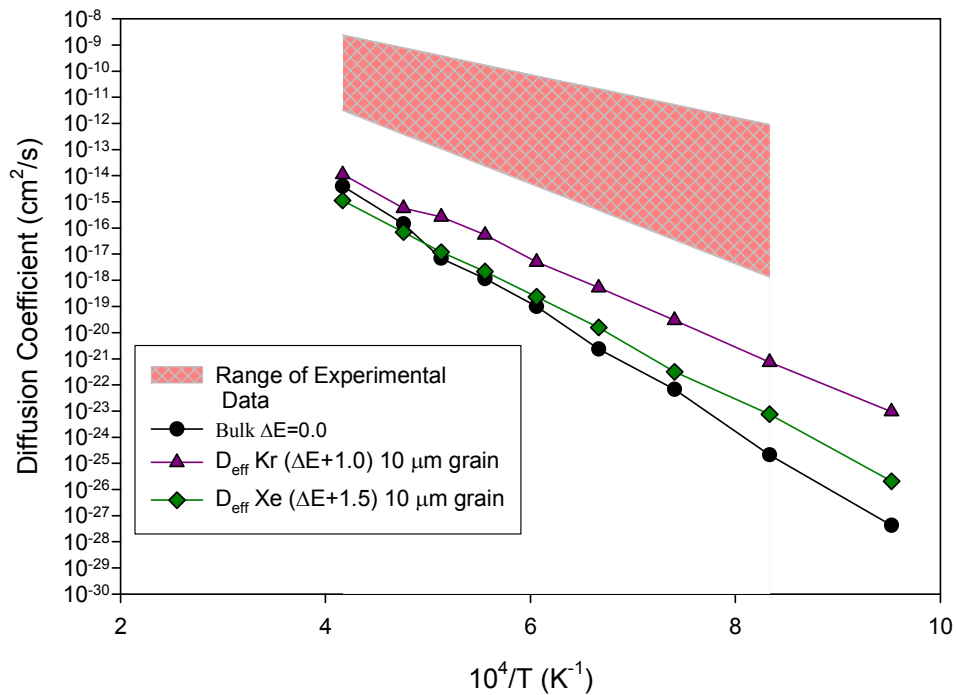

Fig. 5.16. Combined Effect of Radiation Damage and Grain Boundaries on the enhancement of the diffusion coefficient for Kr and Xe with a U vacancy concentration of 0.025

The combined effect of Radiation Damage and Grain Boundaries can be seen in Fig. 5.16. In this figure, the Bulk diffusion coefficient for radiation damage equivalent to a U vacancy concentration of 0.025 is plotted with the grain boundary diffusion coefficients for Kr and Xe with the same U vacancy concentration. As was shown in Fig. 5.15 increasing radiation damage does not proportionally increase the diffusion coefficient for the Kr and Xe, so the effective diffusion coefficients for the 10 μm grain size Kr and Xe case do not change much. However, the case for bulk tri-vacancy migration with no additional energy does see a significant diffusion coefficient enhancement over its corresponding value in Fig. 5.13.

In addition to the experimental Xe diffusion behavior exemplified by the Matzke Experimental fit shown in Fig. 5.16 [57]. Uranium Dioxide nuclear fuel undergoes a recrystallization event at high burn-up (near 6.5% Fissions per Initial Metal Atom (FIMA)). Once the threshold burn-up is reached, the microstructure of the UO_2 fuel transitions from 10-20 μm grains to a grain size of around 1 μm. This phenomenon in UO_2 goes by many names such as high burn-up structure, polygonized high burn-up structure, and rim structure, which refers to the formation of this structure on the outer rim of high burn-up fuel rods. One important impact of this change is the Xe concentration in the fuel reaches a steady state level in the fuel of $0.2 - 0.3$ wt.% [81]. This high burn-up steady state Xe concentration in the UO_2 can be related to an effective diffusion coefficient for Xe in the fuel. Investigation into the consequences of the 0.2-0.3 wt.% Xe concentration in high-burn-up UO_2 using the Booth equivalent sphere model for fission gas release had revealed the Xe Diffusion Coefficient near 1273K is expected to be near 10^{-18} to 10^{-20} cm^2/s [81]. This is several orders of magnitude lower than what is predicted by the low burn-up Matzke Fit [57]. Independent

investigations into the high burn-up structure have also come to similar conclusions regarding the Xe diffusion coefficient [82]. Other studies have observed a drop in migration energy for Xe diffusion as a function of burn-up that correspond well to a change from an energy expected from bulk diffusion to an energy more typical of grain boundary diffusion [83]. By using the diffusion coefficient range from Reference [81] and the migration energy from Reference [83] it is possible to create a predicted range for High burn-up Xe diffusion. This range is plotted with the effective diffusion coefficients for Kr and Xe for 1 μm grain diameter derived from the KMC simulations in Fig. 5.17 along with the experimental fits from Matzke, Davies, and the R/B models. The lower diffusion coefficients predicted for the high burn-up recrystallized UO$_2$ appear to coincide with the 1 μm diameter grain sized KMC simulation results for Kr and Xe. However, the comparison of the KMC simulation to high burn-up fuel is a comparison to two non-equivalent systems. The KMC simulation does not include many of the expected features of high burn-up fuel such as large interconnected pores and fission product precipitates that act as traps for migrating fission gas [13]. The conditions of the KMC simulation are more closely related to the expected conditions for low burn-up fuel.

The two bands of experimental data in Fig. 5.17 deserve additional exploration to elucidate the different conditions assumed for each set of data. The low burn-up experimental data range is bound on the low diffusion end by a low burn-up measurement of single Xe atom diffusion by Davies [77]. The high diffusion end of this data is bound by the PARFUME model for Kr and Xe diffusion out of failed TRISO fuel. The diffusion coefficients for the Xe release from failed TRISO are derived from experiments that observe

the release of short lived Xe isotopes. With short lived isotopes, the isotope does not exist for a sufficient time to account for trapping that may occur with longer lived species [81]. In the case of the Matzke data the fit is derived from a specimen that is largely unperturbed [57]. This implies a low concentration of available traps in the fuel, which will enhance Xe diffusion. Low burn-up conditions also provide a Xe isotope several μm of travel in the fuel before encountering a trap site [61]. Additionally grain boundary diffusion is essential to the diffusion of fission gas in low burn-up measurements [61]. The conditions of the UO_2 fuel in the high burn-up structure are very different. At high burn-up, there are many trap sites present in the UO_2 crystal. The abundance of trap sites will tend to quickly capture Xe atoms [13]. Once in the trap site, the diffusion will proceed much more slowly.

The additions to the KMC model have begun to close the gap between the first Kr and Xe diffusion coefficients that were calculated for bulk crystal diffusion seen in Fig. 5.5 and experimentally measured Xe diffusion coefficients. The grain boundary effect helped to significantly close this gap by several orders of magnitude. The radiation damage effect was small for Kr and Xe, but this result supports experimental observations of Xe diffusion in UO_2 with hetero-valiant impurities. A gap between simulation and low burn-up experiment still exists. A possible bias in the current KMC simulation may stem from the Kr or Xe atoms initially beginning in a Schottky defect. Diffusion in low burn-up experiments may be enhanced by Xe migration that occurs before a trap is reached [61]. However athermal diffusion mechanisms such as Kr and Xe migration before reaching a trap and fission spike driven migration in the fuel cannot account for all of the additional migration experiments suggest is occurring. There may also be additional migration mechanisms in addition to the

filled tri-vacancy mechanism that accelerates in Kr and Xe diffusion in low burn-up UO_2 fuel conditions. An example mechanism could be the trap hoping mechanism mentioned in Section 4.1.6.
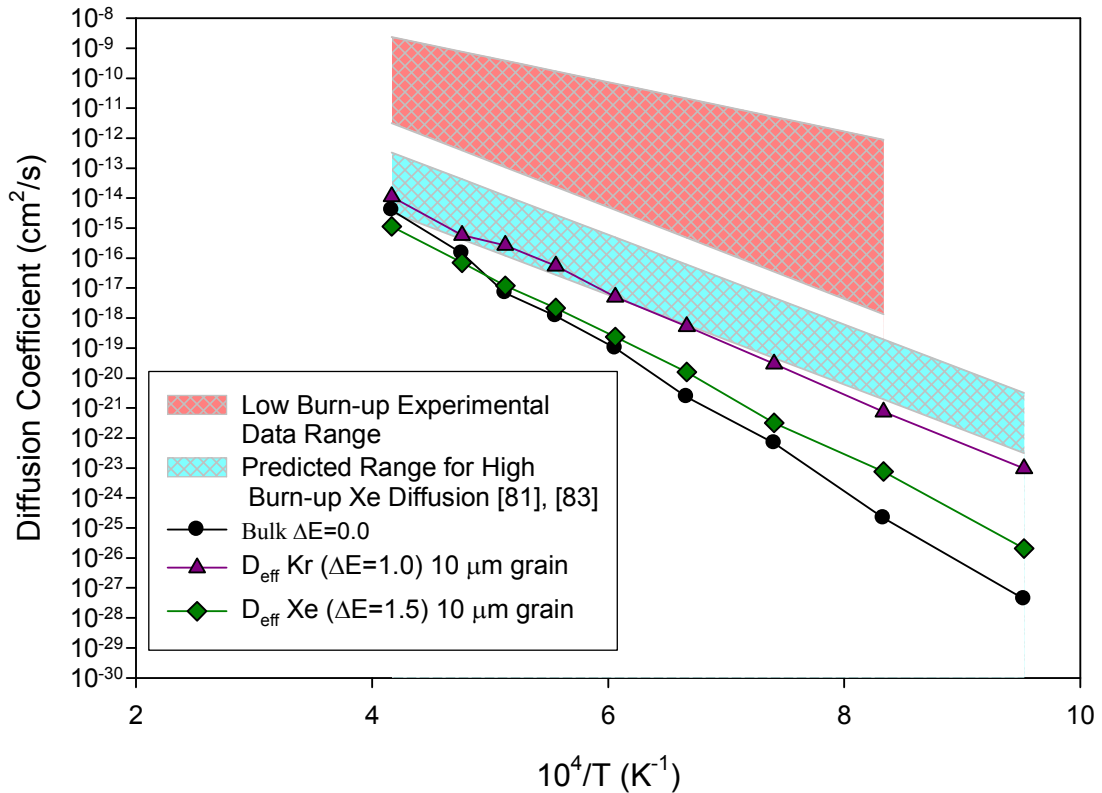
Fig. 5.17. Combined Radiation Damage and Grain boundary Effect Diffusion coefficients derived from KMC simulations for 1 μm grain diameter UO_2 with the predicted high burn-up Xe diffusion coefficient and other experimental fits.

5.1.8 Predicted R/B from Atomistic Simulation

It is always important to bring the simulation back to the link between experiment and simulation that was proposed to connect the gamma-ray spectra that are collected in nuclear fuel tests and the diffusion coefficients derived from atomistic simulation. This concept was illustrated in Fig. 1.2 and can be applied to the diffusion coefficients derived from the KMC simulations to produce R/B values based on the Booth model. Release to Birth ratios based

on the Booth Model for the diffusion coefficients shown in Fig. 5.13 for bulk Kr/Xe diffusion and Fig. 5.17 for 1 μm grain effective diffusion are plotted in Fig. 5.18 for a temperature of 1500 K.
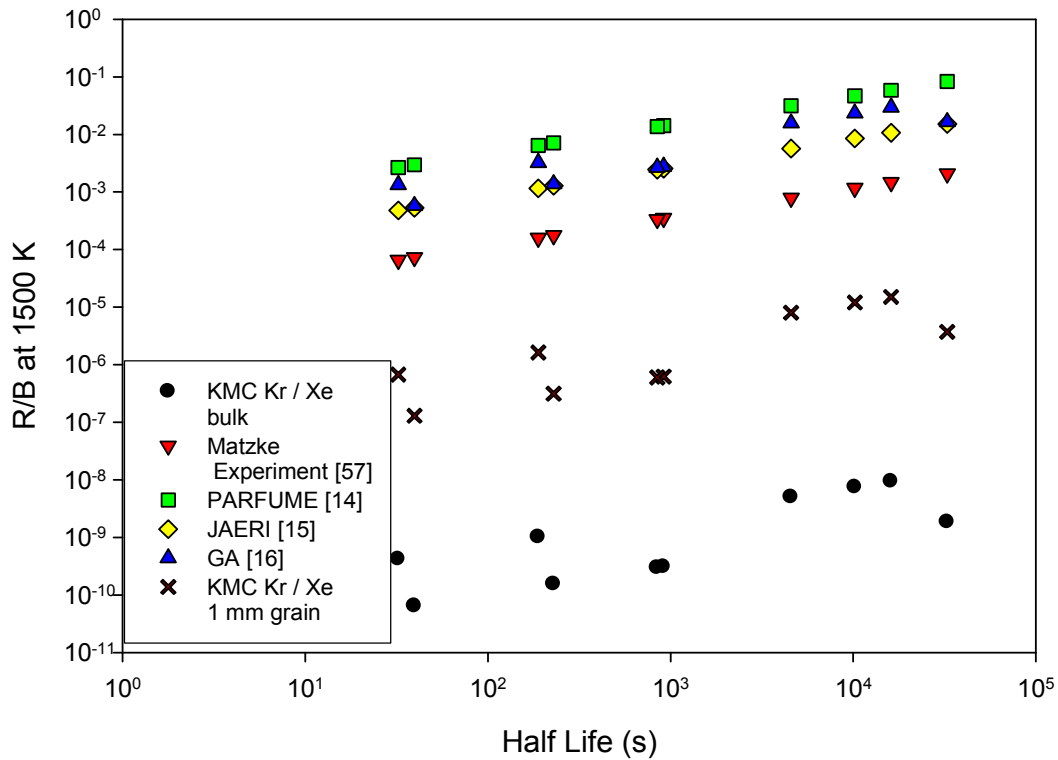
Fig. 5.18. R/B values based on Diffusion Coefficients derived from KMC simulations, polycrystalline experiments and TRISO fuel testing experiments for 1500 K

The R/B values in Fig. 5.18 are calculated with Equation (2.1) where the diffusion coefficients (*D*) are derived from KMC simulations, '*a*' is the radius of the TRISO particle (175 μm for AGR-1), and the decay constants (λ) are for the usual Kr and Xe isotopes of interest. The complete R/B models with the recoil and precursor terms were not used so that the pure diffusive term could be more easily seen between the different models, experimental results and simulations. The KMC results in Fig. 5.18 use the diffusion coefficients for Kr

($\Delta E=1.0$) and Xe ($\Delta E=1.5$) at 1500 K shown in Fig. 5.8 and the effective diffusion coefficient for Kr and Xe for 1.0 μm grains shown in Fig. 5.13. As before with the diffusion coefficients there is a large difference between the atomistic simulation and values from the other data sources, but the inclusion of the grain boundary effect on diffusion closes some of the gap between simulation and measurement

As in Fig. 5.17 with the diffusion coefficients, the R/B models from the KMC simulation are much lower than the low burn-up experimental fit from Matzke and the TRISO R/B relationships. This discrepancy is discussed in the previous section, but there are several characteristics of note present in the R/B model relationships. The migration energy of the diffusion coefficients suggest that many of the models observed diffusion that was not pure bulk diffusion. The German model has a migration energy of 1.63 eV and the GA model has a migration energy of 1.10 eV for their reduced diffusion coefficients. The JAERI model comes closest to having a migration energy that is similar to the Matzke experiment (E_m=3.9 eV) or the KMC simulations (E_m=4.8 eV for bulk diffusion) with a migration energy of 3.27 eV for its reduced diffusion coefficient.

Additional comparisons between the atomistic simulation and the empirical R/B models can be found by formulating indicators (see Equation (2.2)) from the KMC simulation and comparing them to some of the models presented in Fig. 2.2 in a similar fashion. In Fig. 5.19, Indicator values for failed TRISO fuel for the German model [14]and the diffusion only GA model [16] are shown at two different temperatures alongside Indicator values derived from the Kr ($\Delta E=1.0$ eV) and Xe ($\Delta E=1.5$ eV) diffusion coefficients found in the KMC simulations. The behavior of the indicators can be elucidated by examining the effective

equation of the indicator for each model. Equation (2.1) can be approximated as Equation (5.13) for isotopes with half lives less than 10 hours.

$$\left(\frac{R}{B}\right) \approx 3\sqrt{\frac{D'}{\lambda}} \; for \, T_{1/2} < 10 \text{ hours} \tag{5.13}$$

Where D' is the reduced diffusion coefficient, λ is the decay constant, and $T_{1/2}$ is the half life of the isotope of interest. For R/B models with the same reduced diffusion coefficient for both Kr and Xe this implies the Indicator value will be a ratio of half lives between the target Isotope (2) and the reference isotope (1).

$$I = \left(\frac{R}{B}\right)_1 \Bigg/ \left(\frac{R}{B}\right)_2 \approx \frac{3\sqrt{\dfrac{D'}{\lambda_1}}}{3\sqrt{\dfrac{D'}{\lambda_2}}} = \sqrt{\frac{\lambda_2}{\lambda_1}} = \sqrt{\frac{T_{1/2,1}}{T_{1/2,2}}} \tag{5.14}$$

As expected from Equation (5.14) the German model follows a single linear trend on the loglog plot of Indicator versus Half Life. For the GA model, the Indicator values are also roughly linear at higher temperatures in the plot. However, the Xe isotopes have smaller indicator values than would Kr Isotopes of corresponding half lives. This stems from different relationships for the reduced diffusion coefficient that Kr and Xe have in the GA model. The impact of elementally different reduced diffusion coefficient on the indicator behavior is described in Equation (5.15). Notice how there is still no temperature dependence in the Indicator value because the migration energy used in the reduced diffusion coefficient for the GA model is the same for both Kr and Xe.

$$I \approx \frac{3\sqrt{\dfrac{D'_{Xe}}{\lambda_{Xe1}}}}{3\sqrt{\dfrac{D'_{Kr}}{\lambda_{Kr2}}}} = \sqrt{\frac{\lambda_{Kr2}}{\lambda_{Xe1}}} \sqrt{\frac{D'_{0,Xe} \exp\left(-\dfrac{E}{kT}\right)}{D'_{0,Kr} \exp\left(-\dfrac{E}{kT}\right)}} = \sqrt{\frac{T_{1/2,Xe1}}{T_{1/2,Kr2}}} \sqrt{\frac{D'_{0,Xe}}{D'_{0,Kr}}} \tag{5.15}$$

139
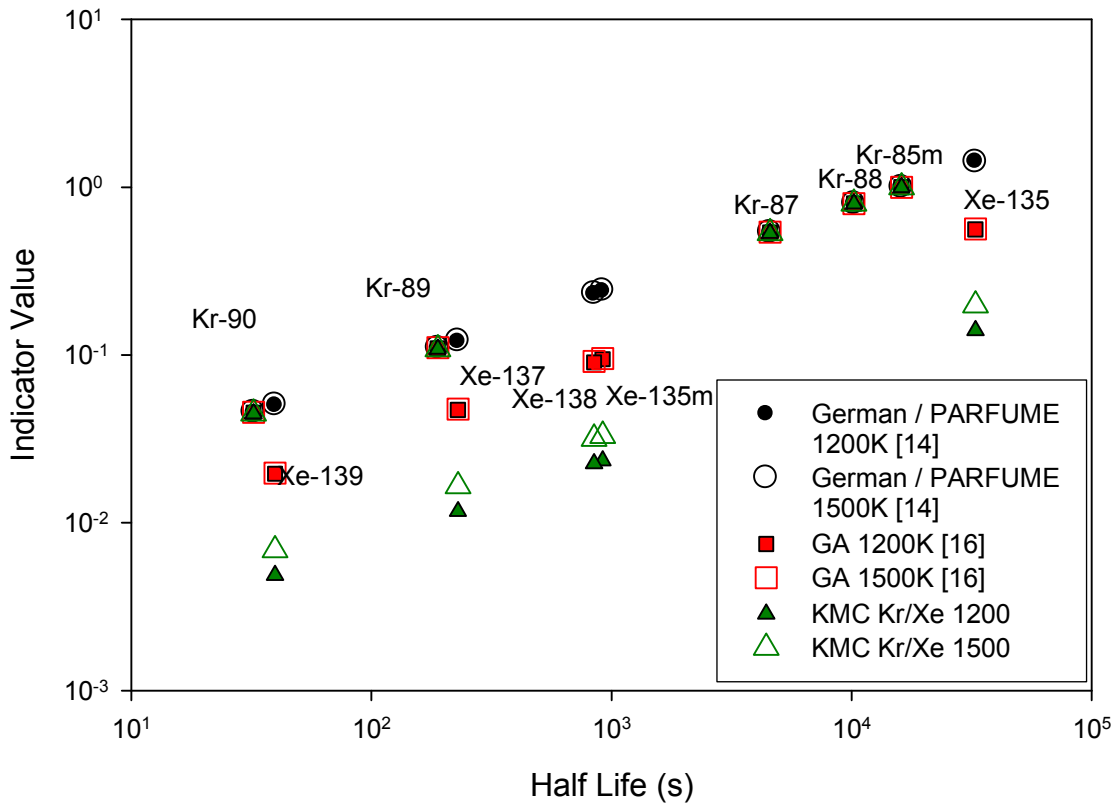
Fig. 5.19. Indicator Values for different failed TRISO particle R/B models at 1200K and 1500K compared to Indicators derived from KMC simulations

The Indicators derived from the KMC simulations also have two separate distinct lines for Kr indicators and Xe indicators. The Kr indicators follow the German model, while the Xe indicators follow two separate linear relationships for the two temperatures. The reasons behind this behavior are slightly different than the GA model. In the GA model there are two relationships for the Kr and Xe reduced diffusion coefficient, but the reduced diffusion coefficients only differ in the pre-exponential terms and have the same migration energy. For the GA model the values shown in Fig. 5.19 are identical for both temperatures. In the diffusion coefficients derived from KMC both the pre-exponential factor and the migration

energy for Kr and Xe differ. This additional term is shown in Equation (5.16) for the KMC results. Here the temperature dependence of the indicators is preserved when comparing different Kr and Xe isotopes.

$$I \approx \frac{3\sqrt{\dfrac{D_{Xe}'}{\lambda_{Xe1}}}}{3\sqrt{\dfrac{D_{Kr}'}{\lambda_{Kr2}}}} = \sqrt{\frac{\lambda_{Kr2}}{\lambda_{Xe1}}}\sqrt{\frac{D_{0,Xe}'\exp\left(-\dfrac{E_{Xe}}{kT}\right)}{D_{0,Kr}'\exp\left(-\dfrac{E_{Kr}}{kT}\right)}} = \sqrt{\frac{T_{\frac{1}{2},Xe1}}{T_{\frac{1}{2},Kr2}}}\sqrt{\frac{D_{0,Xe}'\exp\left(-\dfrac{E_{Xe}}{kT}\right)}{D_{0,Kr}'\exp\left(-\dfrac{E_{Kr}}{kT}\right)}} \qquad (5.16)$$

The result is a variable shift in the Xe indicator values derived from the KMC simulations for different temperatures, not a constant temperature independent shift in Xe indicator values as is seen in the GA model data. This observation shows an additional physical phenomenon that can be elucidated through the use of the Indicator values that was revealed using atomistic simulation.

Chapter 6 Conclusions and Future Work

A multi-scale simulation approach has been developed for studying the bulk diffusion behavior of noble gas fission products in UO_2 and a link between experimental fission gas release experiments and atomistic simulation was explored. Data from on-going TRISO fuel irradiation tests was analyzed using a relative indicator technique that helped emphasized the presence of different physical phenomena in the release of fission gases from TRISO fuel. In this case, the ratios of two Release-to-Birth values (R/B) are established to highlight the presence of recoil, precursor effects, and differences in Kr and Xe diffusion.

To further explore the mechanisms of fission gas release, a Molecular Dynamics model of UO_2 was developed and validated against available experimental data. The accepted probable migration mechanism for Kr and Xe diffusion through UO_2 based on incorporation energy and experimental evidence was proposed. The filled tri-vacancy mechanism has been well established as the suspect mechanism for fission gas migration in UO_2 by both experimental and theoretical means. This mechanism required an understanding of the self-diffusion behavior of O and U in UO_2 that was explored using Molecular Dynamics simulations. The changes in diffusion behavior that result from radiation damage and crystal grain boundaries were also examined using MD where possible. The results of the MD simulation were used in a Kinetic Monte Carlo algorithm developed to simulate the migration of O and U vacancies and Kr or Xe filled tri-vacancies in UO_2. The KMC simulation was able to reproduce the Oxygen self-diffusion and Uranium vacancy self-diffusion experimental behaviors. The stability of Kr or Xe filled tri-vacancies was

established using Molecular Dynamics calculations. Additionally modification to the movement of U atoms due to interactions with Kr or Xe tri-vacancies were modeled in the KMC simulations, and their implications on the diffusion behavior of Kr and Xe in UO_2 were explored. The impact of grain boundaries and radiation damage on the behavior of O and U self-diffusion along with Kr and Xe diffusion was also investigated in KMC. When the resulting diffusion coefficients for Kr and Xe were compared with experimental Xe diffusion coefficients for low burn-up UO_2, the simulated Kr and Xe diffusion coefficients were found to be lower than the experimental values, which might indicate that other migration pathways could be present in the experimental work in addition to the tri-vacancy diffusion mechanism modeled in this work. Nonetheless, the temperature behavior of the simulated and experimental diffusion coefficients was similar.

In addition, the diffusion coefficients from the KMC simulations were recast using the Booth model as R/B ratios and compared to R/B models of fission gas release from TRISO fuel. Trends in the indicator values derived from the results of the KMC simulations were compared to trends present in the R/B models to demonstrate some of the important phenomena revealed by indicator analysis. The microscopic phenomena revealed by the macroscopic Indicator analysis include the importance of half-life to radioisotope release, the effects of separate Kr and Xe diffusion coefficient pre-exponential factors, and the effect of separate migration energies for Kr and Xe,

6.1 *Linking Atomistic Simulations to Gamma Spectrometry*

The multi-scale analysis and simulation technique reported in this work demonstrates the viability of linking two widely different sets of data namely diffusion coefficients from atomistic simulation and gamma-ray spectra collected from on-line nuclear fuel experiments. The important link between the two sets of data is between the Release to Birth Ratios of different isotopes of Kr and Xe and the diffusion coefficient of Kr and Xe developed from atomistic simulation. A variety of physical phenomena that affect diffusion release from failed TRISO can be identified in experimental data using the indicator values discussed in this work. The identified phenomena can then be added to the atomistic simulation. Conversely, by simulating different physics in atomistic simulation it is possible to identify and classify different behaviors in experimental results. Through this coupled analysis a deeper understanding of fission gas release from TRISO fuel may be achieved. The linked study should also lead to better experimental design through improved knowledge of which conditions should be carefully monitored in order to maximize the value of collected experimental data.

6.2 *Future Work*

In this work the migration of Kr and Xe through bulk crystals UO_2 was simulated using a multi-scale atomistic technique. The study of U self-diffusion in the bulk crystal was limited to the Kinetic Monte Carlo simulations. Further study should explore the possibility of using another predictive technique that implements fewer assumptions than KMC to study this process in more detail.

Several saddle point energies were calculated using Molecular Dynamics in the course of this work. A confirmation of these saddle point energies from Ab Initio calculations would be useful in confirming their values. Limited work in Ab Initio has been performed to find the migration energy of U vacancies in UO_2. However, the reported values vary widely (>1 eV) when different Ab Initio parameters are applied [55], and additional confirmation of this energy from Ab Initio or other techniques would be useful for comparison against the 4.8 eV value found in this work. Other saddle point energies of interest for confirmation include the migration of the second U vacancy out of the filled charged tetra-vacancy to conclude the migration mechanism discussed in Section 4.1.6 for cases where Kr and Xe fill the vacancy complex.

An investigation into the effect of grain boundaries impact on Kr and Xe migration was begun. A more detailed analysis of the grain boundary region and its impact on the diffusion of O, U and noble gas fission products should be undertaken in the future. This work examined a single type of grain boundary interface; however, there are many possible high and low angle grain boundaries that could occur in UO_2 that could be investigated to identify their total net impact on O and U self-diffusion and Kr / Xe diffusion.

Future work could also include an investigation of what local effects the Xe or Kr atom impart onto the local conditions of the atoms near the trapped Kr or Xe. For example what additional energy is required to move a U atom into a tetra-vacancy that contains a trapped Kr atom versus a trapped Xe atom. Any changes in the energetics of the system due to trap shape or changes in migration along specific crystal directions could also be investigated.

The current tri-vacancy model for Kr and Xe diffusion through UO_2 assumes a limited influence by the trapped atom on the diffusion process.

The fuel kernel material for current TRISO fuel can be either UO_2 or Uranium Oxycarbide, which is a two phase mixture of UO_2 and UC_2. For UC_2 unlike UO_2 there is very little experimental data. The techniques in this work could be applied to the study of UC_2 in order to produce diffusion coefficients and release to birth ratios for Kr and Xe escaping from the UC_2 phase of failed TRISO particles. The combined release behavior of UO_2 and UC_2 could then be combined to more accurately simulate failed TRISO fuel particles containing kernels consisting of Uranium Oxycarbide.

References

[1]   J.M. Harp, Investigation of Failed TRISO Fuel Assay Using Gamma-Ray Spectrometry, M.S. Thesis, North Carolina State University, 2007

[2]   J. M. Harp, A. I. Hawari, "Relative Release-to-Birth Indicators for Investigating TRISO Fuel Fission Gas Release Models," Proceedings of PHYSOR 2008 Conference, Interlaken Switzerland, 2008.

[3]   A.J. Goodjohn, "Summary of Gas-Cooled Reactor Programs," Energy, v. 16 p. 79-106, (1991)

[4]   M. Ogawa,T. Nishihara, "Present status of energy in Japan and HTTR project," v. 233, i. 1-3, p. 5-10, (2004)

[5]   Y. Xu and K. Zuo. "Overview of the 10 MW high temperature gas cooled reactor—test module project." Nucl. Eng. Des. 218 (2002) 13.

[6]   L Demick, J Kinsey, K Perry, D Petti, "Next Generation Nuclear Plant Project 2009 Status Report," INL Technical Report, INL/EXT-09-17505, OSTI ID: 981867, (2010)

[7]   M. P. LaBar, The Gas Turbine – Modular Helium Reactor: A Promising Option for Near Term Deployment, GA-A23952, General Atomics, 2002

[8]   H. Nickel, H. Nabielek, G. Potta, A. W. Mehner, "Long time experience with the development of HTR fuel elements in Germany," Nuclear Engineering and Design, v. 217, p.141-151 2002

[9]   J.T. Maki, D.A. Petti, D. L. Knudson, G.K. Miller, The challenges associated with high burnup, high temperature and accelerated irradiation for TRISO-coated particle fuel, J. Nuclear Materials. 371, p. 270-280, 2007

[10]   D.M. Scates, J.B. Walter, M.W. Drigert, E.L. Reber, J.M. Harp, "Fission Product Monitoring and Release Data for the Advanced Gas Reactor -1 Experiment," Proc of HTR 2010, Prague, Czech Republic, (2010)

[11]   D. A. Petti, et al, "Technical Program Plan for the Advanced Gas Reactor Fuel Development and Qualification Program", Idaho National Laboratory Report INL/EXT-05-00465, Revision 1, August 2005.

[12]   A. H. Booth, A Method for Calculating Fission Gas Diffusion from UO2 Fuel and its Application to the X-2-F Loop Test. Report CRDC-721, Atomic Energy of Canada Limited. 1957

[13]   D. R. Olander, Fundamental Aspects of Nuclear Reactor Fuel Elements, TID-26711-P1, U.S ERDA Technical Information Center. 1976

[14]   D.A. Petti, P Martin, M. Phelip, R. Ballinger, Development of Improved Models and Designs for Coated-Particle Gas Reactor Fuels, INEEL/EXT-05-02615. 2004

[15]   S. Ueta, J. Sumita, K. Emori, M. Takahashi, K. Sawa, Fuel and Fission Gas Behavior during Riste-to-Power Test of the High Temperature Engineering Test Reactor (HTTR), J. of Nuclear Science and Technology, Vol 40, p. 679-686. 2003

[16]   M. B. Richards, Fission-Gas Release from UCO Microspheres: A Theoretical Model for Fractional Release from Non-hydrolyzed Fuel with Model Parameters Derived from Capsule HFR-B1 Data, General Atomics Report 818:MBR:001:94. 1994

[17]   D. A. Petti, H. Gougar, G.L. Bell, The DOE Advanced Gas Reactor (AGR) Fuel Development and Qualification Program. Conference: 2005 International Congress on Advances in Nuclear Power Plants, INEEL/CON-04-02416, OSTI ID: 911109. 2005

[18]   D.M. Scates, J.K. Hartwell, J.B. Walter, M.W. Drigert, J.M. Harp, "Fission Product Monitoring of TRISO Coated Fuel for the Advanced Gas Reactor-1 Experiment," Proceedings of HTR 2008, Washington D.C. (2008)

[19]   J.M. Harp, A.I. Hawari, Investigating TRISO Fuel Fission Gas Release Models Using Relative Release-to-Birth Indicators, Trans. American Nuclear Society, 96, p 365-367. 2007

[20]   Hawari, A.I., Fleming, R.F., 1994. High accuracy determination of the shape of the efficiency curve of the HPGe detector in the energy range 900 to 1300 keV, Nuclear Instruments and Methods in Physics Research-A, v. 353, p. 106-108.

[21]   J.M. Harp, A.I. Hawari, M.A. Bourham, Simulation of Gamma-Ray Spectrometry of Failed TRISO Fuel, Nuclear Instruments and Methods in Physics Research-A, v. 579, p. 301-304. 2007

[22]   A.G. Croff, ORIGEN: Isotope Generation and Depletion Code System Matrix Exponential Method, Version 2.2. Oak Ridge National Laboratory, ORNL/TM-7175. 1980

[23]   J.K. Hartwell, J.B. Walter, D.M. Scates, M.W. Drigert, Determination Of The AGR-1 Capsule to FPMS Spectrometer Transport Volumes From Leadout Flow Test Data, INL/EXT-07-12494. 2007

[24]   D.M. Scates, private communication, 2009

[25]   J.K. Hartwell, private communication, 2007

[26]   G. Jackson, D. Davies, P. Biddle, :Fission Gas Emission from UO2 During Irradiation at 800-1600oC, AERE Technical Report AERE-R-4714, OSTI ID: 4656344, 1964

[27]   M. Stan, J.C. Ramirez, P. Cristea, S.Y. Hu, C. Deo, B.P. Uberuaga, S. Srivilliputhur, S.P. Rudin, J.M. Wills, Models and simulations of nuclear fuel materials properties, Journal of Alloys and Compounds, Volumes 444-445, 2007

[28]   Vlachos, Adv. Chem. Eng. 30, 1-61 (2005)

[29]   F. Ercolessi, "A molecular dynamics primer," Spring College in Computational Physics, ICTP, Trieste, June 1997, http://www.fisica.uniud.it/~ercolessi/md/md/

[30]   J.M. Haile, *Molecular Dynamics Simulation: Elementary Methods*, John Wiley & Sons, 1997

[31]   D. Frenkel, B. Smit, *Understanding Molecular Simulation*, Academic Press, Elsevier (USA), 2002

[32]   A.F. Voter, "INTRODUCTION TO THE KINETIC MONTE CARLO METHOD", *Radiation Effects in Solids*, K.E. Sickafus et al. (eds.), Springer, 2007

[33]   G.H. Vineyard, "Frequency Factors and Isotope Effects in Solid State Rate Processes," J. Phys. Chem. Solids, v. 3, (1957)

[34]   S. Ovesson, A. Bogicevic, G. Wahnstrom, B.I. Lundqvist, "Neglected adsorbate interactions behind diffusion prefactor anomalies on metals,"

[35]   Fujitsu Limited, Materials Explorer Ultra 4.0, 2006

[36]   K. Refson, "Moldy: a portable molecular dynamics simulation program for serial and parallel computers," Computer Physics Communications, 126(3):309--328, 2000

[37]   W Smith, T.R. Forester, "DL_POLY 2.0. A General Purpose Parallel Molecular Dynamics Package," J. Mol. Graphics, 1996

[38]   N.D. Morelon, D. Ghaleb, J.M. Delaye, L. Van Brutzel, Philosophical Magazine, v. 83, n. 13, 1533-1550, 2003

[39]   J.R. Walker, C.R.A. Catlow, "Structural and Dynamic Properties of UO2 at high temperatures," J. Phys. C: Solid State Phys., vol. 14, p.979-983, (1981)

[40]   M. T. Hutchings, "High-Temperature Studies of UO2 and ThO2 using Neutron Scattering Techniques," J. Chem. Soc. Faraday Trans. II 83, 1083-1103 (1987).

[41]   J. K. Fink, "Thermophysical properties of uranium dioxide," J. Nuclear Materials, vol. 279, p. 1-18, (2000).

[42]   J. K. Fink, International Nuclear Safety Center Documentation, http://www.insc.anl.gov/

[43]   S. Motoyama, Y. Ichikawa, Y. Hiwatari, "Thermal conductivity of uranium dioxide by nonequilibrium molecular dynamics simulation," Physical Review B, v. 60, n. 1, 1999

[44]   J.L. Bates, High-temperature thermal conductivity of round robin' uranium dioxide, Battelle Memorial Institute Pacific Northwest Laboratories Report BNWL-1431, 1970

[45]   R. W. Grimes, "Simulating the Behaviour of Inert Gases in UO2," Fundamental Aspects of Inert Gases in Solids, NATO Report, Ed. S.E. Donnelly, Ed. J.H. Evans, Plenum Press, New York, 1991

[46]   K.A. Jackson, *Kinetic Processes Crystal Growth, Diffusion, and Phase Transitions in Materials*, Wiley-VCH, Weinheim, 2004

[47]   G.S. Was, *Fundamentals of Radiation Materials Science Metals and Alloys*, Springer, 2007

[48]   T.R. England, B.F. Rider, "Fission Product Yields per 100 Fissions for [235]U Thermal Neutron Induced Fission Decay," LA-UR-94-3106

[49]   H. Matzke, "Gas release mechanisms in UO_2 - a critical review," Radiation Effects, v. 53, (1980)

[50]   M. Barrachina, R. Dubourga, M.P. Kissanea, V. Ozrin, "Progress in understanding fission-product behaviour in coated uranium-dioxide fuel particles," J. Nuclear Materials, v. 385, (2009)

[51]   R.A. Jackson, C.R.A. Catlow, "Trapping and Solution of Fission Xe in UO2. Part 1 Single gas atoms and solution from underpressurized bubbles," J. Nuclear Material, v. 127, (1985)

[52]   S. Nicoll, H. Matzke, C.R.A. Catlow, "A computational study of the effect of Xe concentration on the behaviour of single Xe atoms in UO2," J. Nuclear Material, v. 226, (1995)

[53]   R.W. Grimes, C.R.A. Catlow, "Calculations of Solution Energies of Fission Products in Uranium Dioxide," J. Am. Ceram. Soc. v. 72, n. 10, 1856-60, (1989)

[54]   M. Freyss, N. Vergnet, T. Petit, "Ab initio modeling of the behavior of helium and Xenon in actinide dioxide nuclear fuels," J. Nuclear Materials, 352 144-150 (2006)

[55]   Y. Yun, H. Kim, H. Kim, K. Park, "Atomic diffusion mechanism of Xe in UO2," J. Nuclear Materials, 378 40-44, (2008)

[56]   C. R. A. Catlow, "Fission Gas Diffusion in Uranium Dioxide," Proc. R. Soc. London A., v. 364, (1978)

[57]   Hj. Matzke, "Fundamental Aspects of Inert Gas Behaviour in Nuclear Fuels: Oxides, Carbides and Nitrides," Fundamental Aspects of Inert Gases in Solids, NATO Report, Ed. S.E. Donnelly, Ed. J.H. Evans, Plenum Press, New York, (1991)

[58]   J.R. MacEwan, W.H. Stevens, "Xenon Diffusion in UO_2 Some Complicating Factors," J. Nuclear Materials, v. 11, (1964)

[59]   J.A. Turnbull, C.A. Friskney, J.R. Findley, F.H. Johnson, A.J. Walter, "The diffusion coefficients of gaseous and volatile species during the irradiation of uranium dioxide," J. Nuclear Materials, v. 107, (1982)

[60]   R.A. Jackson, C.R.A. Catlow, "Trapping and Solution of Fission Xe in UO_2: Part 1. Single gas atoms and solution from underpressurized bubbles," J. Nuclear Materials, v. 127 (1985)

[61]   D.R. Olander, P. Van Uffelen, "On the role of grain boundary diffusion in fission gas release," J. Nuclear Materials, v. 288, 131, (2001)

[62]   J. Belle, "Oxygen and Uranium Diffusion in Uranium Dioxide (a review)," J. Nuclear Materials, v. 30, p. 3-15, (1969)

[63]   J.F. Marin, P. Contamin, "Uranium and Oxygen Self-Diffusion in UO_2," J. Nuclear Materials, v. 30, p. 16-25, (1969)

[64]   K.C. Kim, D.R. Olander, "Oxygen Diffusion in UO_{2-x}," J. Nuclear Materials, v. 102, p. 192-199, (1981)

[65]   R.A. Jackson, A.D. Murray, J.H. Harding, C.R.A. Catlow. Philos. Mag. A 53 (1986), p. 27

[66]   L. Van Brutzel, A. Chartier, J. P. Crocombette , "Basic mechanisms of Frenkel pair recombinations in UO_2 fluorite structure calculated by molecular dynamics simulations," Phys. Rev. B 78, (2008)

[67]   Hj. Matzke, "Atomic Transport Properties in U02 and Mixed Oxides," J. Chem. Soc. Faraday Trans. 2 (83) (1987) 1121.

[68] A.C.S. Sabioni, W.B. Ferraz, F. Millot, "First study of uranium self-diffusion in UO2 by SIMS," J. Nuclear Materials 257 (1998) 180-184

[69] H. Mehrer, *Diffusion in solids: fundamentals, methods, materials, diffusion-constrolled processes*, Springer, 2007

[70] I. Kaur, Y. Mishin, W. Gust, *Fundamentals of Grain and Interphase Boundary Diffusion*, 3rd ed., John Wiley & Sons, 1995

[71] R. Devanathan, J. Yu, W.J. Weber, "Energetic recoils in UO2 simulated using five different potentials," J. Chem. Phys. 130, 174502

[72] L. Van Brutzel, J.P. Crocombette, "Atomic Scale Modelling of the Primary Damage State of Irradiated UO2 Matrix," Mater. Res. Soc. Symp. Proc., v. 981, 2007

[73] Personal communication, Iyad Al Qasir, 2010

[74] G. Dolling, R. A. Cowley, A. D. B. Woods, "The Crystal Dynamics of Uranium Dioxide," Can. J. Phys. 43(8): 1397–1413 (1965)

[75] D.S. Aidhy, P.C. Millett, T. Desai, D. Wolf, S.R. Phillpot, "Kinetically evolving irradiation-induced point defect clusters in UO2 by molecular dynamics simulation," Physical Review B 80, 104107 (2009)

[76] R.G.J. Ball and R.W. Grimes, J. Chem. Soc. Faraday Trans. 86, p. 1257 (1990)

[77] D. Davies, G. Long, AERE Report 4347, (1963)

[78] D.R. Olander, "Combined Grain-Boundary and Lattice Diffusion in Fine-Grained Ceramics," Advances in Ceramics, v. 17 *Fission-Product Behavior in Ceramic Oxide Fuel*

[79] M.I. Norgett, M.T. Robinson, I.M. Torrens, "A Proposed Method of Calculating Displacement Dose Rates," Nuclear Engineering and Design, v. 33 (1975)

[80] C. Meis, A. Chartier, "Calculation of the threshold displacement energies in UO2 using ionic potentials," J. Nuclear Materials, v. 341, (2005)

[81] S. Bremier, C.T. Walker, "Radiation-Enhanced Diffusion and Fission Gas Release From Recrystallised Grains in High Burn-up UO_2 Nuclear Fuel," Radiation Effects and Defects in Solids, v. 157, 311, (2002)

[82] P. Blair, A. Romano,Ch. Hellwig, R. Chawla, "Calculations on fission gas behaviour in the high burnup structure," J. Nuclear Materials, v. 350 232 (2006)

[83]   J.P. Hiernaut, C. Ronchi, "Fission gas release and volume diffusion enthalpy in UO_2 irradiated at low and high burnup," J. Nuclear Materials, v. 294 39 (2001)

APPENDICES

Appendix A - Investigation of an Experimental Technique to Separate Krypton and Xenon

The combined gamma-ray spectrum from Kr and Xe fission gas released from failed TRISO fuel is quite complex as can be seen in Fig. A.1. Current fuel tests utilize high resolution High Purity Germanium (HPGe) detectors to monitor the isotopic composition of the released gases. However in possible future Very High Temperature Reactors it may not be desirable to use HPGe detectors in an industrial setting. HPGe detectors require cooling to liquid nitrogen temperatures and their performance degrades in the presence of high neutron fields. An alternative to using HPGe detector may be the use of one of the several newly developed medium resolution detectors like Lanthanum Bromide scintillators (LaBr(Ce)) that do not require cryogenic cooling. In order to reduce the complexity of the gamma-ray spectrum measured by the detector a plasma separations device has been tested to see if Kr and Xe can be ionized and selectively directed towards the detector. During the testing of the device some promising results were obtained that indicated the count rate at the detector could be influenced by manipulating the plasma with a magnetic field.
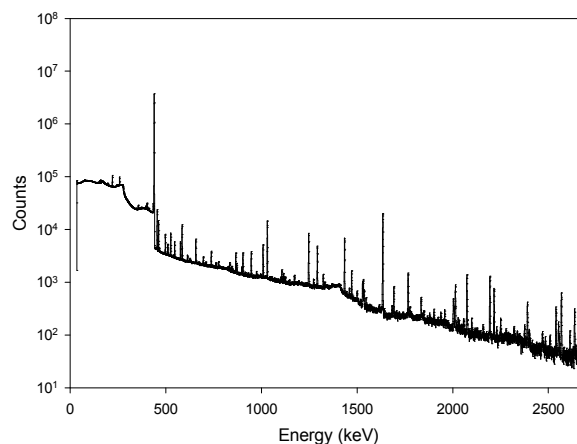
**Fig. A.1.** Experimental Spectrum from AGR-1 Experiment

155

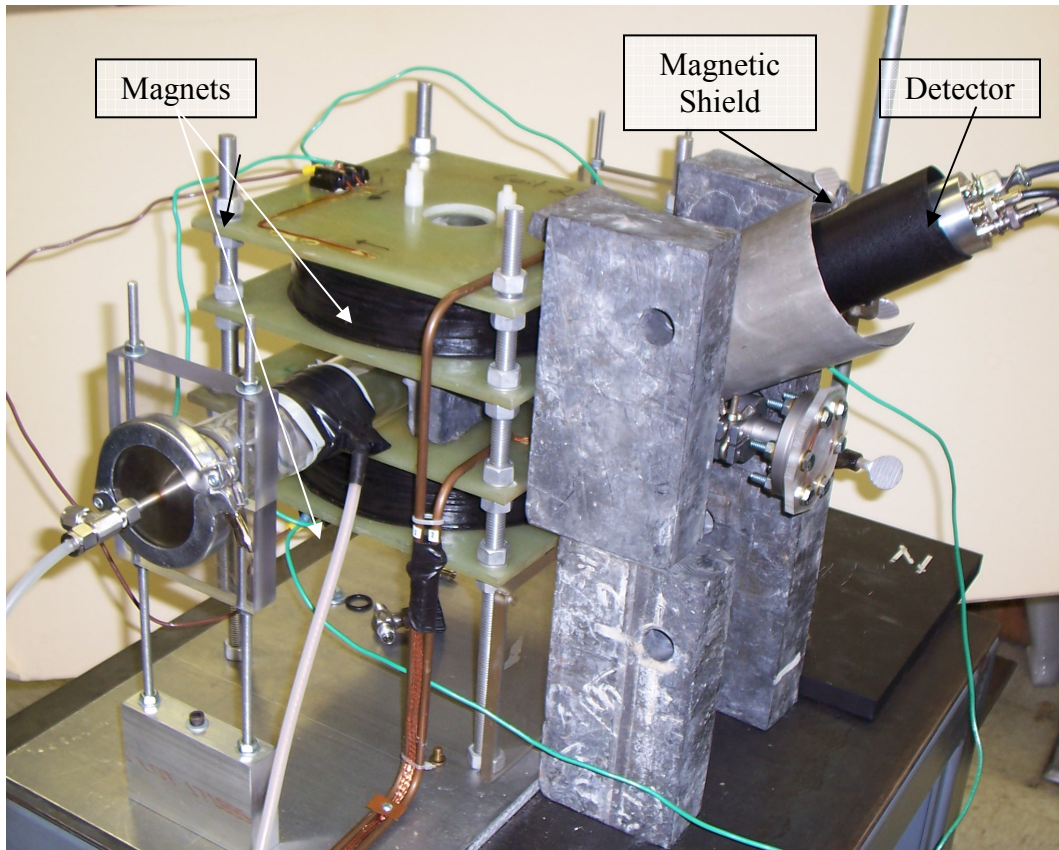## A.1 Description of Plasma Separation Test Cell

The front and top view of the plasma device can be seen in Fig. A.2 and Fig. A.3. Gas enters the glass 'T' section where the electrodes create and inductive plasma. The electrodes were connected to a transformer that amplified the peak-to-peak voltage of an AC power source 1000x, and the signal was 180° out of phase between the two electrodes. The magnets consisted of two identically wound coils placed directly above the centerline of the glass 'T' tube. The current for the magnet was supplied by a 60 V, 20 A, DC power supply. The magnets direct the ionized plasma around the elbow of the glass and towards the detector. A pressure gauge located up stream from the inlet is used to determine when the device has reached a low enough pressure to generate plasma. The detector currently in use is a 1.5 x 1.5 inch LaBr(Ce) scintillator. It is collimated as much as possible by lead bricks and is located inside a magnetic shield that prevents interference from the electromagnets of the device. The magnetic field of the device was distorting the energy calibration of the detector. The detector is mounted at an angle looking down on the area just below the elbow of the glass 'T'. This put the detector out of the direct line of sight to the main plasma channel and allows it to preferentially detect magnetically steered plasma.

Radioactive samples of Kr and Xe are created with neutron activation in the NCSU Pulstar reactor. Natural Kr and Xe are used as the activation sample for these tests. Both Kr and Xe have several stable isotopes that lead to many different activation products. However, only Kr-85m and Xe-125 are created in sufficient activity and have a half life long enough to be useful in these tests. Samples of gas are heat sealed in 7 mL vials and shot into the reactor using the pneumatic rabbit system for irradiation times of usually 10 to 20

156

minutes depending on the needs of the sample and the operating power of the reactor. Since the samples are of finite size, the plasma device is operated as a closed system for radioactive tests meaning the valve to the main vacuum pump is closed during radioactive gas operation. In this configuration the plasma device can operate for several hours given its leak rate of approximately 0.5 torr per hour. Closed system operation is also necessary from a radiological safety standpoint given the ALARA principle. A radioactive sample transfer device was assembled to provide for the easy insertion of the radioactive samples into the system. The transfer device is shown in Fig. A.4. This device connects to the vacuum system and has flexible tubing on that allow for the crushing of the sample vial to release the gas.
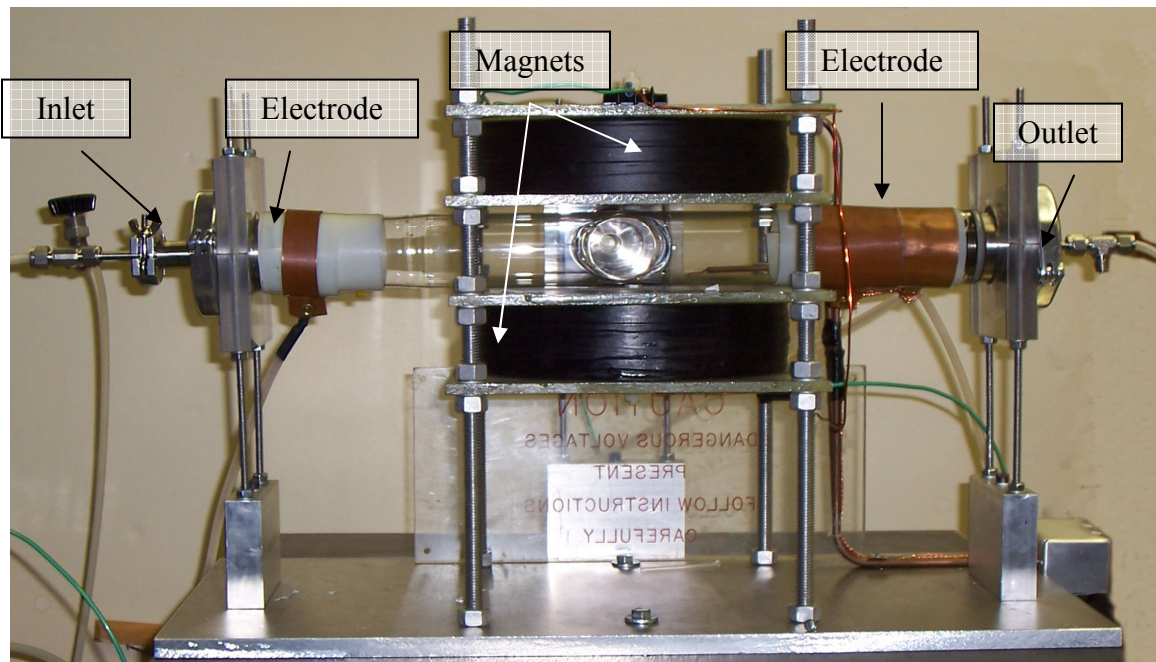
Fig. A.2. Front View of the Plasma Separation Device Prototype

**Fig. A.3.** Plasma Device Prototype with LaBr(Ce) detector and shielding

Fig. A.4 Radioactive Sample Transfer device with Xe-3 sample inside

A.2　　　Operational Characteristics of Plasma Separation Test Cell

During operation of the device, the system is first purged with He and then pumped down to a pressure of about 1.75 torr. Once the sample vial is crushed the radioactive sample fills the system up to a total pressure of about 4 torr. A plasma is then established and counts are collected on the detector system for various different magnetic settings. The counting time for each magnetic setting is dependent on the activity sample. Usually adequate counting statistics (~1%) are collected after 5 or 10 minutes of counting. Measurements have been taken at approximately 30 or 60 Gauss increments up to a maximum magnetic field of about 537 G. The results of this measurement are shown in Fig. A.5. The two coils have a resistance of 3.3 Ohms each. They are wired in parallel to reduce the effective resistance resulting in half the total power supply current flowing through each coil. The LaBr(Ce) detector used in this experiment can easily distinguish between the 4 primary gamma-rays emitted by Kr-85m (151 and 302 keV) and Xe-125 (188 and 243 keV). A sample spectrum that contains both Kr-85m peaks and Xe-125 peaks is shown in Fig. A.6. Peak areas are recorded by the MCA software and then post processed to account for source decay. Experimental uncertainty is assigned based on counting statistics and standard error propagation techniques.

$$B_{mag}=30.303(I_{total})-8.532$$
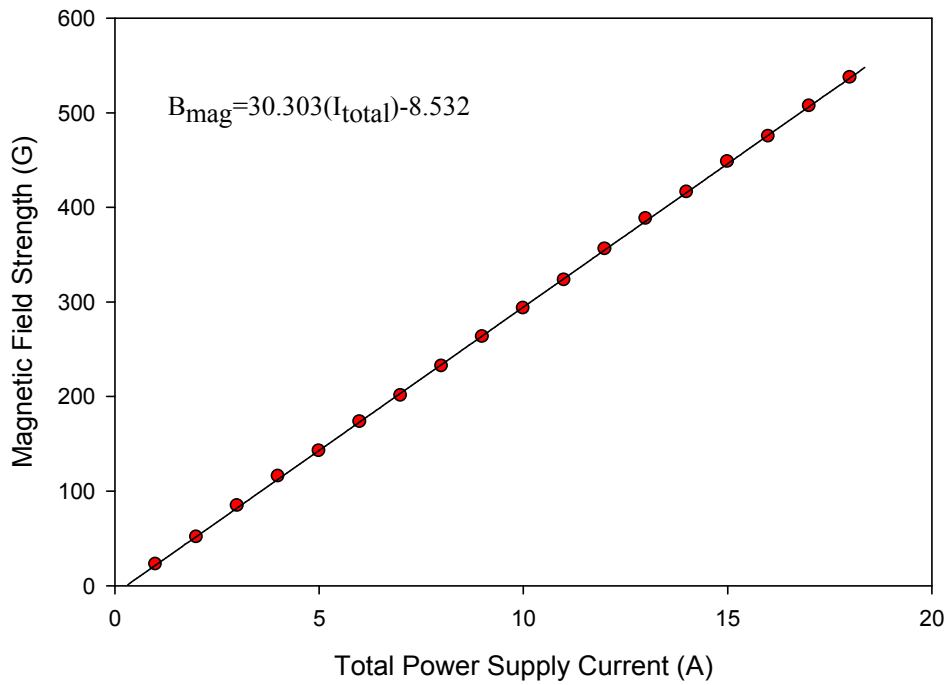
Fig. A.5 Measured relationship between Total Power Supply Current and Magnetic Field Strength for case where coils are wired in parallel and linear fit to this relationship
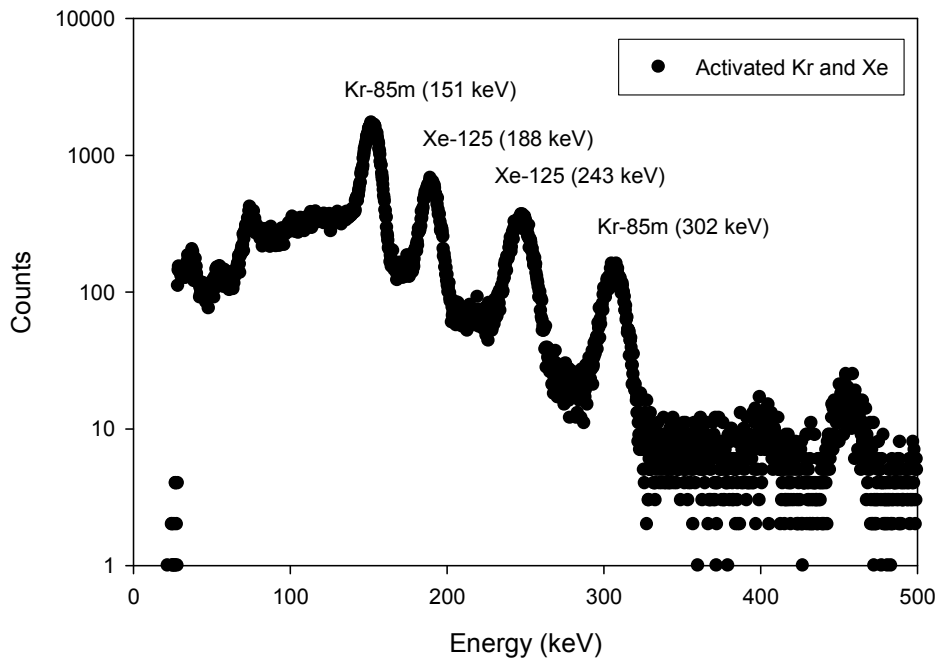
Fig. A.6. A Sample Spectrum of Kr-85m and Xe-125 on the LaBr(Ce) Detector

A.3　　　Results from Plasma Separation Test Cell

The test cell underwent several different modifications each of which lead to a better understanding of the physics occurring inside the device. Initial tests performed late in 2008 illustrated the need to modify the device in several key ways. First a magnetic shield for the detector was added to eliminate the interaction of the electrons in the PM-tube and detector crystal with the magnetic field from the device's Hemholtz coils. Shielding was also added to the device and around the detector to limit the gamma source to nuclei decaying in the center and 3rd leg of the glass T. Additionally the detector was moved from viewing the device straight down the 3rd leg to viewing the 3rd leg at an angle looking down onto the device as is shown in Fig. A.3. Improvements were also made in the preparation of the Kr and Xe gas samples that were irradiated in the reactor. The samples were filled by what will be called the "Glove Method" that lead to more consistent sample preparations and less noble gas waste. In this process the 7mL sample vials used for irradiation are placed inside a nitrile examination glove with most of the air removed. The glove is then filled like a balloon with either Kr or Xe. The samples are then closed while inside noble gas atmosphere of the glove then removed and heat sealed for irradiation. After these improvements were made tests were performed in March 2009 that successfully demonstrated a statistically significant change in the gamma source strength with respect to changing the magnetic field.

Over the course of the experiment several different tests were performed to evaluate the device performance in two key areas. The first was the relationship between magnetic field strength and a change in counts or effective source strength observed by the detector, and the second was the ability of the device to selectively enhance either the Kr or the Xe component

of the signal. Typically, counts were taken for long enough to adequately establish good counting statistics (<1% relative error) in at least the lower energy Kr-85m and Xe-125 peaks at different magnetic field settings. The frequency setting on the power supply was adjusted to shape the plasma in the glass 'T' into a coherent cylinder usually in the range 15-25 kHz. This setting was left unchanged for the duration of each test that consisted of sweeping through the magnetic field intensity range.

Initial tests of the plasma device produced an increase in the count rate of the detector of approximately 6% in both Kr and Xe samples. The initial results of these tests are shown in Fig. A.7. Kr and Xe were separately injected into the device and the change in the relative source strength as a function of magnetic field strength was measured. The initial tests were limited to about 425 G because of the voltage limits of the magnetic power supply. In subsequent tests the coils that made up the magnet were wired in parallel instead of in series, this modification allowed a larger range of magnetic field strengths to be explored as can be seen in Fig. A.8 and Fig. A.9. However the larger range did not lead to a greater enhancement in the relative source strength at the detector. It appeared that the change in effective source strength reached a threshold above about 400 G where any additional enhancement from the magnetic field was offset by competing physical phenomena. The threshold is very clear in the Kr only data shown in Fig. A. 10. The Kr / Xe separation metric for device performance was not demonstrated in these tests. Both Kr and Xe develop the roughly the same enhancement in source strength at the same magnetic fields.
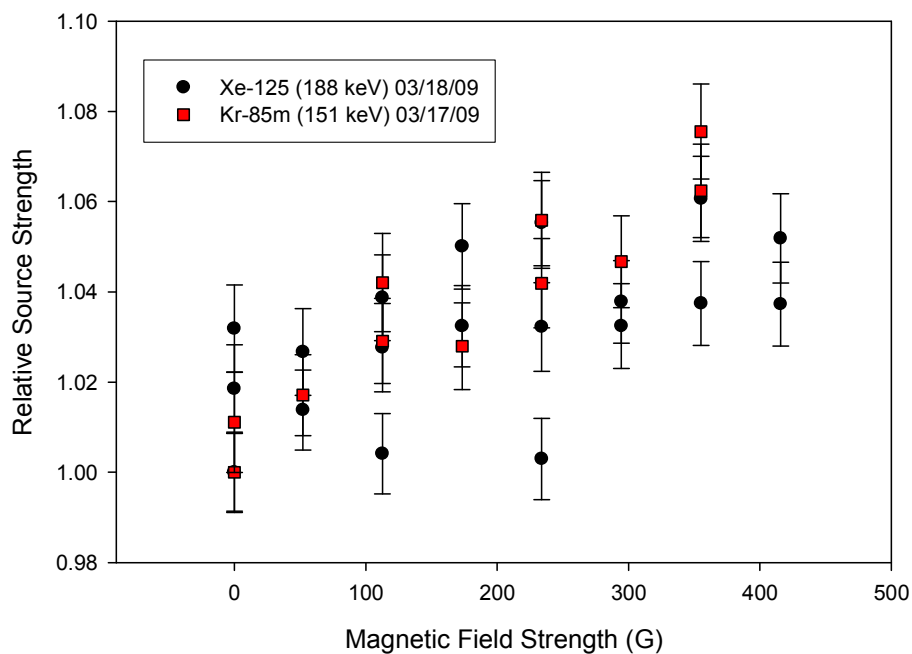
Fig. A.7. Separate Kr and Xe Measurements of signal enhancement versus magnetic field strength
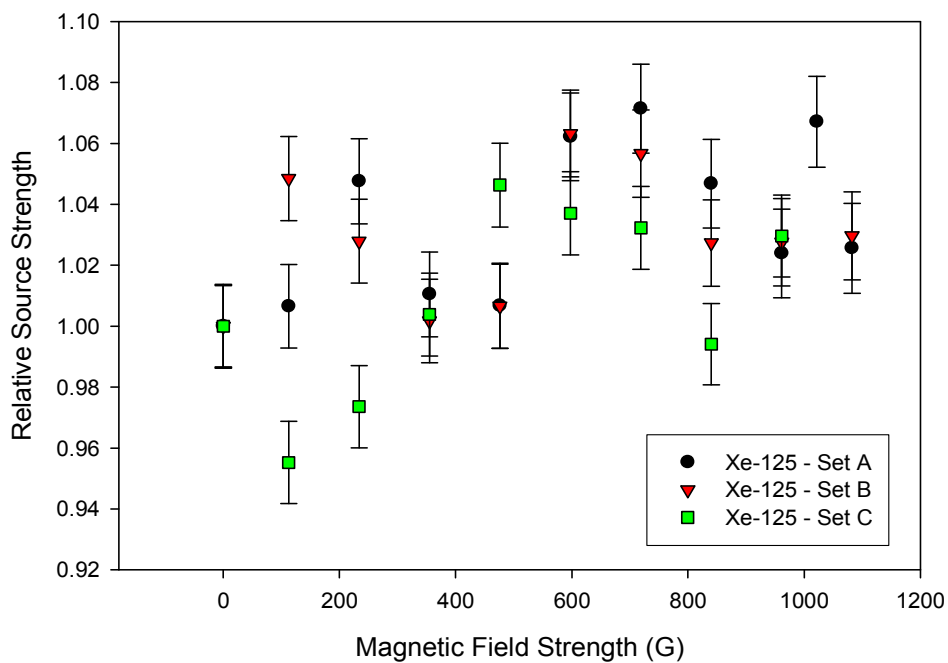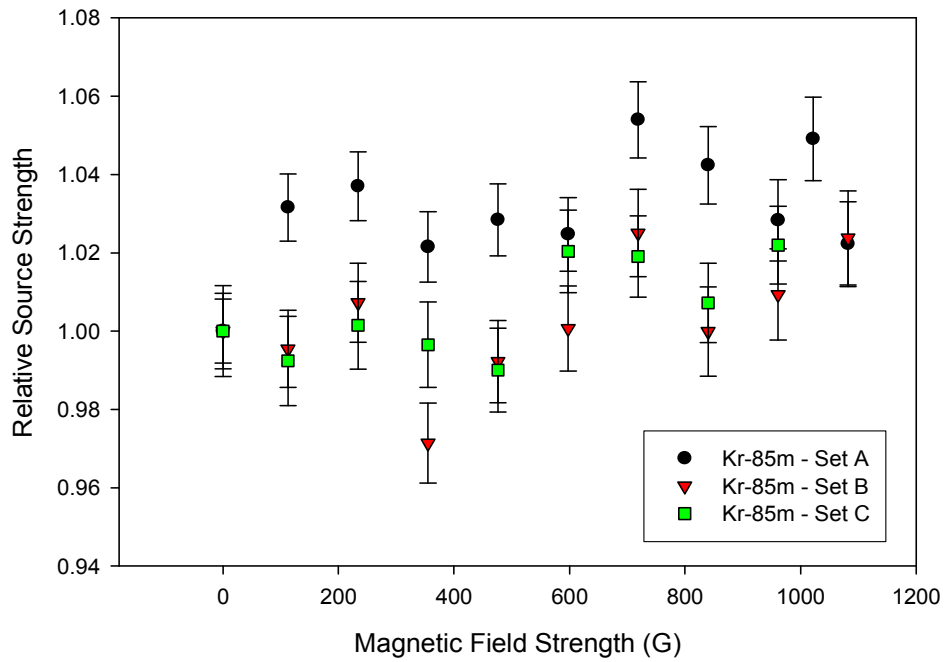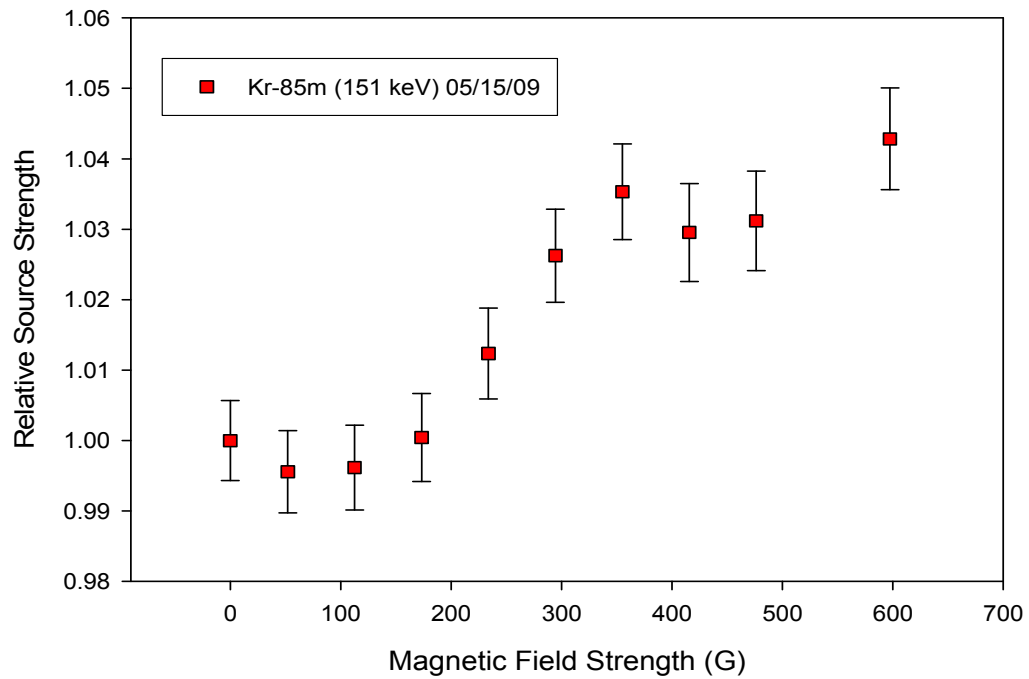

Fig. A.8. Xe Measurements of signal enhancement vs. magnetic field strength over a larger range of magnetic field strength

Fig. A.9 Kr Measurements of signal enhancement vs. magnetic field strength over a larger range of magnetic field strength


Fig. A. 10 Kr only measurement of source strength vs. magnetic field

164

After considering the initial results that only produced a <10% enhancement in effective source strength with no clear separate behavior between Kr and Xe, the basic physics of the system were reevaluated. Operating the plasma system in the 1-4 torr range severely limits the mean free path of Kr and Xe ions in the system. The mean free path was estimated from the Langevin cross section to be 37.8 μm for Kr and 29.7 μm for Xe at 1 torr. Additionally most of the gas in the system was not ionized (neutral atomic density ~10^{16} cm^{-3}, ion density ~10^{10} cm^{-3}) and most of the gas was also not one of the radioactive isotopes of Kr or Xe (radioactive atomic density ~10^7 cm^{-3}).

Two modifications to the device were also made. An induced signal that was found in the cart that held the device was eliminated by grounding the cart directly to the electrical system ground. Signal was also found on the vacuum fittings that were attached to the 3rd leg of the system. This signal scaled proportionally with changes in the magnetic field. It was also found that the fitting on the 3rd leg were acting as an induced ground for the plasma. If one electrode was disconnected plasma would stream from the connected electrode down the 3rd leg, and the intensity of this streaming could be modified by changing the strength of the magnetic field. The intensity of the signal striking the fittings on the 3rd leg could be visually observed and measured on an oscilloscope. Also at very low pressures the plasma could be seen and measured streaming down the 3rd leg even when both electrodes were connected. This behavior was undesirable, and the fittings were replaced with a single blank fitting. With this setup the induced ground effect was reduced but not completely eliminated.

Tests were then performed with these modifications in place. In addition to the standard test configuration, 3 other configurations were tested. The measurement was done with the

current flowing through the Helmholtz coils such that the plasma would be directed towards the 3rd leg (labeled B field +) and with the current in the opposite direction such that the plasma was directed away from the 3rd leg (labeled B field -). The electrical connections from the transformer were also attached to alternatively to either electrode to test for the presence of any DC bias in the transformer (Electrodes Normal or Electrodes Switched). The result was a 2x2 matrix of tests are partially shown in Fig. A.11 and Fig. A.12. Reversing the magnetic field causes the relative source strength to decrease as magnetic field is increased. Switching the electrodes did not have an effect on the effective source strength as can be seen in Fig. A.12.
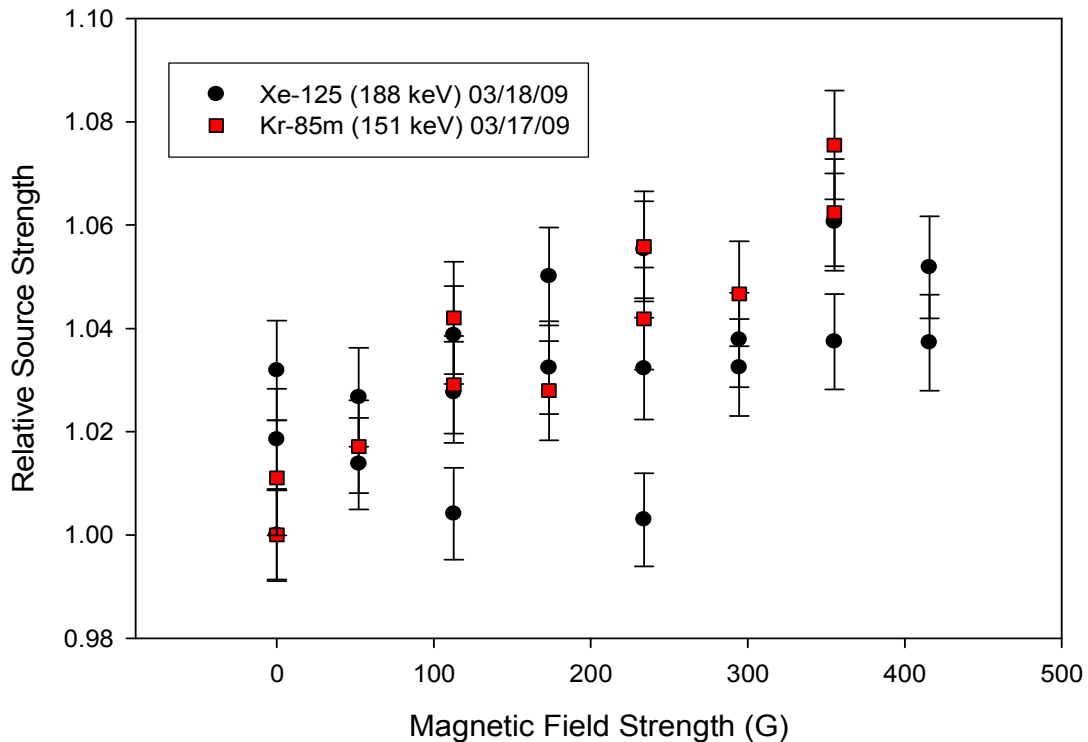
Fig. A.11. Standard Configuration (B+, E normal) showing increased counts with increased magnetic field
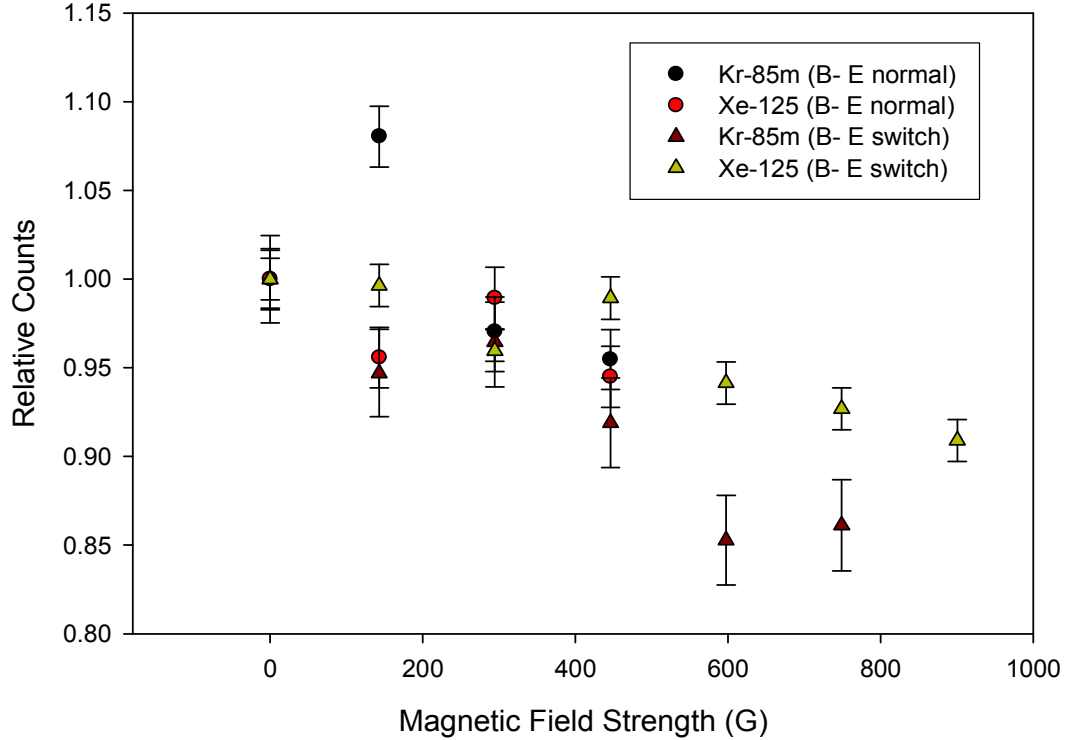
166

Fig. A.12. Reversed magnetic field configuration with the electrodes normal and switched

A.4   Summary of Plasma Cell Results

From these results it can be concluded that some change in the relative source strength of

the samples being tested in the device is occurring with respect to magnetic field strength.

Evidence of separation of the Kr and Xe species was not observed in these tests. However,

the concept does show some promise in enhancing the results of in-core fueled experiments.

There are several conditions that could not be tested with the current equipment, but could

potentially enhance the performance of a similar device. The creation of a consistent flow

for all gas in the device would improve the ability of the magnetic field to separate the Kr

and Xe ions. Lowering the pressure would also be ideal however lowering the pressure must

be balanced against supplying enough radioactive material to the detector to allow for detection.

In order to further explore the concept electro-magnetic elemental separation of radioactive Kr and Xe, an alternative design could be considered. Gas sampled from an effluent would be ionized at a single location and accelerated into a vacuum chamber that could accommodate large differences in the radii of the Kr and Xe isotopes (i.e. 1x1 m). Inside the chamber orthogonal DC electric and magnetic fields would create separation approximately the size of the vacuum chamber. A detector could then be collimated to observe only the impact site of either the Kr or the Xe, or the electric / magnetic field conditions could be modified to concentrate Kr or Xe on the detector. This design would depend on several key factors. The vacuum chamber must be large enough so that the flight paths of the Kr and Xe impact on the chamber wall at significantly different positions (~10 cm) that allow for signal isolation. The pressure of the vacuum chamber must be low enough so that the mean free path of the ions is much greater than the flight path distance in order to prevent recombination. The system will have to process enough gas to collect gamma-ray spectra, and be able to operate reliably for at least several days. These physics driven design features should allow for clearer elemental separation using electro-magnetic techniques.

An alternative design for separating Kr and Xe that could potentially be used involves using staged cryogenic traps to separate the Kr and Xe streams. This design concept would take advantage of the different melting point temperatures of Kr and Xe. The heavier element Xe has a melting point of 161.25 K and Kr has a melting point at 115.93K. By utilizing linked cryogenic traps that were adjusted to two different temperatures, Xe could be

removed from the effluent with the initial trap that was set to a temperature somewhere between the melting temperatures of Kr and Xe. In the second trap the temperature should be set below the melting temperature of Kr but above the melting temperature of Ne (24.5K) to avoid trapping any Ne present in the effluent. For in-pile fuel experiments, Ne is often used to regulate the temperature through mixing He and Ne concentrations in the effluent gas stream. Unfortunately Ne activates to Ne-23 which is and undesirable contaminant in the collected gamma-ray spectrum of Kr and Xe isotopes. Two detectors could then view each trap. Assuming full capture of the Xe in the first trap, the spectrum from the Kr trap would be free of any Xe lines that could cause an interference in calculating the release activities. Additionally, the traps would continually confine the released Kr and Xe enhancing the signal. Currently the release activity is monitored as it moves through the detection volume in a once through configuration. With cryogenic trapping the release activity would continually increase in the traps until an equilibrium activity equal to the release rate at the fuel not the travel time decayed activity that is currently detected. In this design, the enhanced signal strength coupled with the separation of Xe from the Kr stream could potentially improve the accuracy of release activity determination and possibly allow for the use of lower resolution room temperature detectors in the monitoring of in-pile fuel experiments.

Appendix B – Derivation of Average Phonon Frequency for use as KMC Input

Kinetic Monte Carlo calculations require two inputs that convey most of the physics regarding the migration of a certain species. They are the height of the energy barrier (E_B) and the frequency pre-exponential factor term (v_0). The rate constants for a jump are then determined from the following formula in Equation (B.1)

$$v(T) = v_0 \exp\left(-\frac{E_B}{kT}\right) \tag{B.1}$$

Where k is Boltzmann's constant, and T is the temperature of the system. For this work the v_0 term for U atoms in UO_2 was estimated from a phonon frequency distribution of UO_2 derived from Ab Initio calculations of the phonon density of states. The phonon frequency distribution is shown in Fig. B.1. It was calculated with a relaxed structure at 0K. It is possible to include pseudo temperature effects in the Ab Initio calculations; however, the frequency of the heavy U atom will change little through the temperature ranges of interest. The average v_0 for U that was used in the KMC calculations was taken as the spectrum averaged frequency using the following formula in Equation (B.2).

$$\bar{v}_0 = \frac{\sum_{i=1}^{N} w_i v_i}{\sum_{i=1}^{N} w_i} \tag{B.2}$$

The phonon frequency spectrum was split into N equal 'i' bins that each had a corresponding frequency (v_i) and distribution weight (w_i) (i.e. the y axis value for each frequency from Fig. B.1). From these values, it was possible to find the spectrum averaged phonon frequency ($\bar{v}_0$) for both U and O. The U average frequency value that was used as

an input to the KMC calculations was found to be 3.7867 THz. The O average frequency was 10.964 THz.
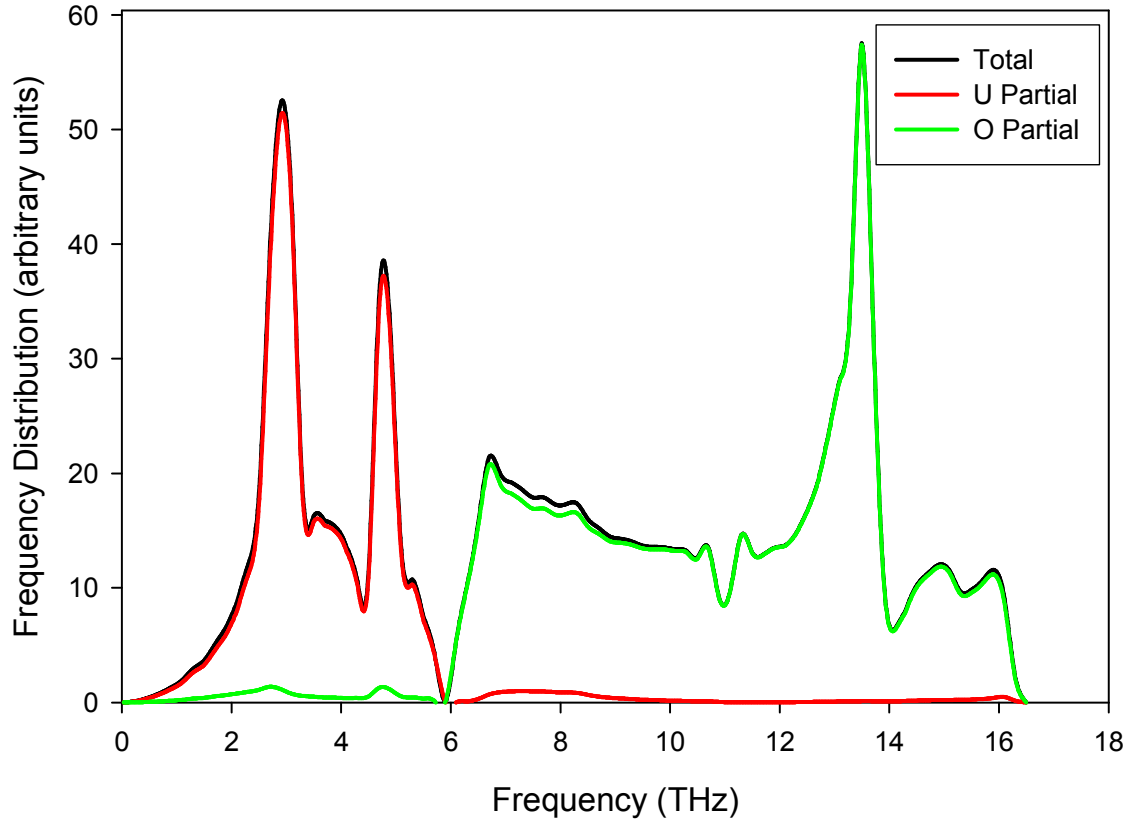
Fig. B.1. Phonon Frequency Distribution of UO_2 from Ab Initio Calculations